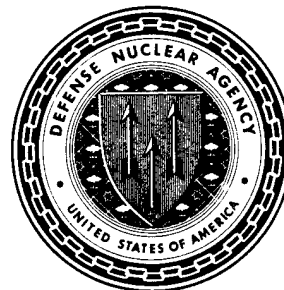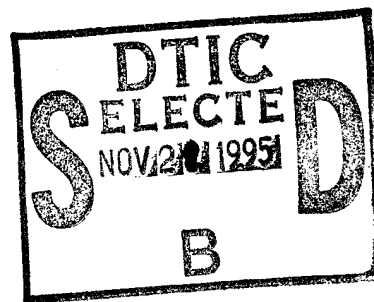Defense Nuclear Agency
Alexandria, VA 22310-3398

DNA-TR-94-190

Numerical Simulation of Damage in Concrete

Yvonne D. Murray
Brett A. Lewis
APTEK, Inc.
1257 Lake Plaza Drive
Colorado Springs, CO 80906-3578

November 1995

Technical Report

CONTRACT No. DNA 001-91-C-0075

DTIC QUALITY INSPECTED 8

19951120 111

DISCLAIMER NOTICE
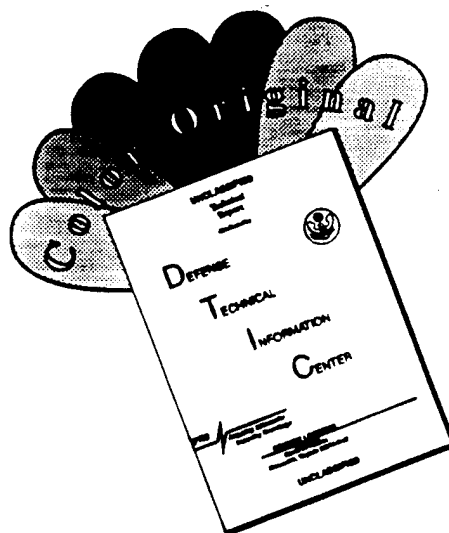
THIS DOCUMENT IS BEST QUALITY AVAILABLE. THE COPY FURNISHED TO DTIC CONTAINED A SIGNIFICANT NUMBER OF COLOR PAGES WHICH DO NOT REPRODUCE LEGIBLY ON BLACK AND WHITE MICROFICHE.

REPORT DOCUMENTATION PAGE

1. AGENCY USE ONLY (Leave blank)	2. REPORT DATE 951101	3. REPORT TYPE AND DATES COVERED Technical 910520 – 940620

4. TITLE AND SUBTITLE

Numerical Simulation of Damage in Concrete

5. FUNDING NUMBERS

C   - DNA 001-91-C-0075
PE - 62715H
PR - RS
TA - RC
WU- DH307770

6. AUTHOR(S)

Yvonne D. Murray and Brett A. Lewis

7. PERFORMING ORGANIZATION NAME(S) AND ADDRESS(ES)

APTEK, Inc.
1257 Lake Plaza Drive
Colorado Springs, CO 80906-3578

8. PERFORMING ORGANIZATION REPORT NUMBER

A-94-2R

9. SPONSORING/MONITORING AGENCY NAME(S) AND ADDRESS(ES)

Defense Nuclear Agency
6801 Telegraph Road
Alexandria, VA 22310-3398
SPSD/Giltrud

10. SPONSORING/MONITORING AGENCY REPORT NUMBER

DNA-TR-94-190

11. SUPPLEMENTARY NOTES

This work was sponsored by the Defense Nuclear Agency under RDT&E RMC Code B4662D RS RC 4300A 25904D.

12a. DISTRIBUTION/AVAILABILITY STATEMENT

Approved for public release; distribution is unlimited.

12b. DISTRIBUTION CODE

13. ABSTRACT *(Maximum 200 words)*

An elasto-plastic damage model for concrete and other geologic materials was implemented into the three-dimensional, nonlinear finite element code DYNA3D. The smooth-cap model contains an isotropic damage formulation for modeling strain-softening and modulus reduction, a three-invariant plasticity surface formulation to simultaneously fit triaxial compression and extension data, and a viscoplastic formulation for modeling strength enhancement at high strain rates. Separate formulations for brittle and ductile damage are implemented. The model captures the essential features of concrete behavior: shear enhanced compaction, dilatency, pre-peak hardening, post-peak softening, modulus reduction, and localized damage accumulation.

Selected benchmark applications demonstrate the fit of the model to standard laboratory test data, bending analysis of reinforced concrete slabs, and comparisons of single element and multi-element laboratory test simulations. The multi-element simulations predict diagonal damage patterns and splitting, which are typical failure modes of unconfined compression test specimens. The multi-element simulations also predict more severe softening than the single-element simulations.

14. SUBJECT TERMS

Concrete	Damage	Dilation	
DYNA3D	Benchmarks	Microcracks	
Smooth-Cap	Strain-Softening	Viscoplasticity	Finite Element

15. NUMBER OF PAGES

140

16. PRICE CODE

17. SECURITY CLASSIFICATION OF REPORT UNCLASSIFIED	18. SECURITY CLASSIFICATION OF THIS PAGE UNCLASSIFIED	19. SECURITY CLASSIFICATION OF ABSTRACT UNCLASSIFIED	20. LIMITATION OF ABSTRACT SAR

CLASSIFIED BY:

N/A since Unclassified.

DECLASSIFY ON:

N/A since Unclassified.

ABSTRACT

The goal of the work under the Conventional Weapons Effects (CWE) program reported here is to predict the dynamic response and damage of buried reinforced concrete structures subjected to airblast and bomb case fragment impact from internal detonations of conventional weapons. Performing such calculations with a first principles code requires implementation of a comprehensive material model for concrete, particularly for modeling strain-softening in the tensile regime and in the low confining pressure compressive regime. We implemented a smooth-cap model with damage into the nonlinear finite element code DYNA3D (Reference 1) to analyze the dynamic response of plain concrete, and other geologic materials. The *capabilities* of the concrete damage model, with and without modeling steel reinforcement, are demonstrated in the present report through a series of structural benchmark calculations. The *validity* of the concrete damage and reinforcement models will be assessed in a future report by comparing the model predictions with full scale Dipole East tests and sub-scale Precision Model tests.

The main body of this report reviews two topics. The first topic is concrete material model development. The original basis of our concrete damage model is a two-invariant, smooth-cap elasto-plastic model (Reference 2). We added numerous features to this model to improve comparisons with standard laboratory test data. These improvements include a damage formulation for modeling strain-softening and modulus reduction in both the tensile and compression regimes, a three-invariant plasticity formulation to model a realistic failure envelope, and a viscoplastic formulation for modeling strength enhancement at high strain rates.

The second topic is selected benchmark applications using the concrete damage model. This report includes fits of the model to standard laboratory test data, bending analysis of reinforced concrete slabs, and comparisons of single and multiple element simulations for unconfined compression tests. The multi-element test simulations predict the softening response and localized damage accumulation of concrete test specimens better than the single element calculations. In particular, multi-element simulations predict more severe softening than single element models. Multi-element simulations also predict diagonal damage patterns and splitting, which are typical failure models of concrete test specimens.

Accession For

NTIS GRA&I	☑
DTIC TAB	☐
Unannounced	☐
Justification	

By____
Distribution/
Availability Codes

| Dist | Avail and/or Special |

A-1

iii

CONVERSION TABLE

Conversion factors for U.S. Customary to metric (SI) units of measurement.

MULTIPLY $\longrightarrow$ TO GET $\longleftarrow$	$\longrightarrow$ BY $\longrightarrow$ $\longleftarrow$ BY $\longleftarrow$	$\longrightarrow$ TO GET $\longleftarrow$ DIVIDE
angstrom	$1.000\ 000 \times$ E-10	meters (m)
atmosphere (normal)	$1.013\ 250 \times$ E+2	kilo pascal (kPa)
bar	$1.000\ 000 \times$ E+2	kilo pascal (kPa)
British thermal unit (thermochemical)	$1.054\ 350 \times$ E+3	joule (J)
degree (angle)	$1.745\ 329 \times$ E-2	radian (rad)
degree Fahrenheit	$T_K = (T_F + 459.67)/1.8$	degree kelvin (K)
erg	$1.000\ 000 \times$ E-7	joule (J)
erg/second	$1.000\ 000 \times$ E-7	watt (W)
foot	$3.048\ 000 \times$ E-1	meter (m)
gallon (U.S. liquid)	$3.785\ 412 \times$ E-3	meter^3 (m^3)
inch	$2.540\ 000 \times$ E-2	meter (m)
joule/kilogram (J/kg)	$1.000\ 000$	Gray (Gy) **
kilotons	4.183	terajoules
ktap	$1.000\ 000 \times$ E+2	newton- second/m^2 (N-s/m^2)
micron (μm)	$1.000\ 000 \times$ E-6	meter (m)
mil	$2.540\ 000 \times$ E-5	meter (m)
mile (international)	$1.609\ 344 \times$ E+3	meter (m)
ounce	$2.834\ 952 \times$ E-2	kilogram (kg)
pound-force (lbf avoirdupois)	$4.448\ 222$	newton (N)
pound-force/foot^2	$4.788\ 026 \times$ E-2	kilo pascal (kPa)
pound-force/inch^2 (psi)	$6.894\ 757$	kilo pascal (kPa)
pound-mass (lbm avoirdupois)	$4.535\ 924 \times$ E-1	kilogram (kg)
pound-mass/foot^3	$1.601\ 846 \times$ E+1	kilogram/meter^3 (kg/m^3)
shake	$1.000\ 000 \times$ E-8	second (s)
slug	$1.459\ 390 \times$ E+1	kilogram (kg)
snail	$5.712\ 000 \times$ E-6	gram (gr)
torr (mm Hg, 0°C)	$1.333\ 220 \times$ E-1	kilo pascal (kPa)

** The Gray (Gy) is the SI unit of absorbed radiation.

TABLE OF CONTENTS

TABLE OF CONTENTS (Continued)

LIST OF ILLUSTRATIONS

LIST OF ILLUSTRATIONS (Continued)

LIST OF ILLUSTRATIONS (Continued)

LIST OF ILLUSTRATIONS (Continued)

LIST OF TABLES

SECTION 1

INTRODUCTION TO THE CONCRETE DAMAGE MODEL

Numerous plasticity models have been developed over the years to describe the constitutive behavior of concrete under various loading conditions. One common type of plasticity model is the elasto-plastic *cap* model originally attributed to Sandler and Rubin in Reference 3. Cap models predict perfectly-plastic response for laboratory test simulations, such as triaxial compression (TXC) or extension (TXE) simulations, as schematically shown by the line with circles in Figure 1.1. Perfectly-plastic response is typical of concrete and other geologic materials at high confining pressures, but is not representative of concrete at low or no confining pressure. At low confining pressure, concrete exhibits strain-softening, which is a decrease in strength during progressive straining after a peak strength value is reached.
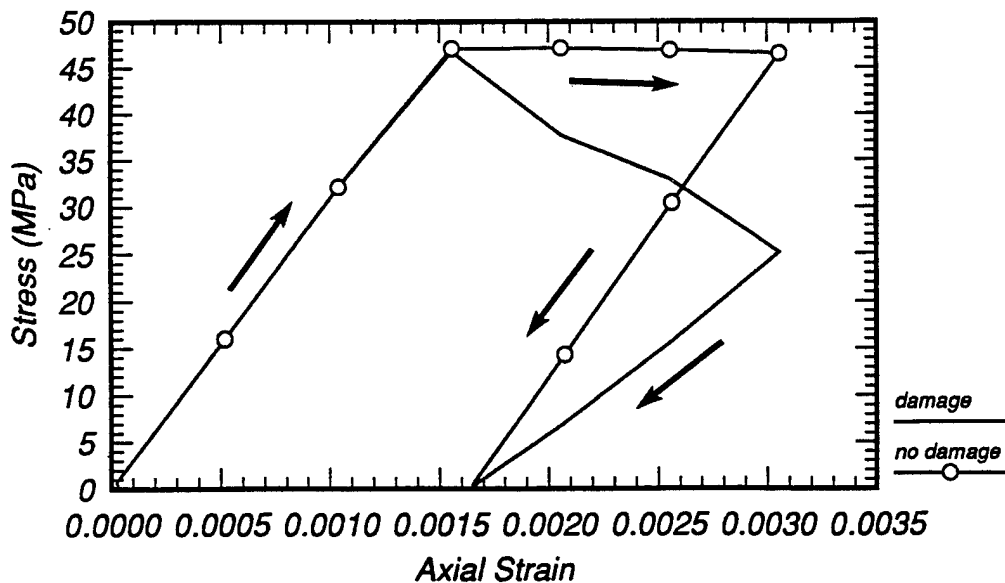
Figure 1.1. Comparison of strain-softening (calculated with damage) and perfectly-plastic (calculated without damage) responses for TXC simulations.

More recently, Simo and Ju in References 4-5 developed a continuum damage formulation with application to cap models, which captures the strain-softening behavior of concrete. APTEK imple-

1

mented their damage formulation into the elasto-plastic cap model in the DYNA3D finite element code. A simulation with strain-softening is indicated by the solid line in Figure 1.1. The cap model with damage captures the essential features of concrete behavior, such as pre-peak hardening, post-peak softening, shear-enhanced compaction, volume expansion under compressive loading (dilation), modulus reduction under cyclic loading/unloading, irreversible deformation, and localized damage accumulation, as discussed throughout the remainder of this report.

The cap model with damage treats plastic flow and damage accumulation as separate processes. Plastic flow is generally assumed to be due to the frictional movement (slip) of microcrack surfaces and is controlled by the presence of shear stresses. Plastic flow results in permanent deformation although the elastic moduli do not degrade with this modelling mechanism. Damage, or the progressive degradation of moduli and strength commonly observed in concrete test specimens, is thought to be due to the growth and coalescence of microcracks. For the remainder of this report, any reference to *damage* will indicate a reduction in moduli caused by the growth and coalescence of microcracks.

The significance of modeling damage accumulation as well as plastic flow is best explained by examining the schematic stress-strain curves shown in Figure 1.2 for three different material model behaviors. The elasto-plastic model in Figure 1.2a is commonly referred to as a plasticity softening model. The stress-strain simulation exhibits permanent deformation following elastic unloading, but no reduction in moduli. Permanent deformation is evident because the simulation unloads to zero stress at non-zero values of strain. Lack of damage (modulus reduction) is evident because the slopes of the initial loading and subsequent loading/unloading curves are equal. Such behavior is often modeled with cap models by shifting or contracting the failure (plasticity) surface to produce the strain-softening response. APTEK, however, does not model strain-softening in this manner. The second model in Figure 1.2b is an example of an elasto-damage model. The stress-strain simulation exhibits a reduction in moduli with increasing strain-softening, but no permanent deformation. The reduction in moduli is indicated by the decrease in the elastic loading/unloading slopes as strain-softening progresses. Such a model is readily implemented by applying Simo and Ju's damage degradation formulation to an elastic model, rather than cap model. In fact, we model concrete response in the brittle (tensile pressure) regime with an elasto-damage simplification of the cap

2
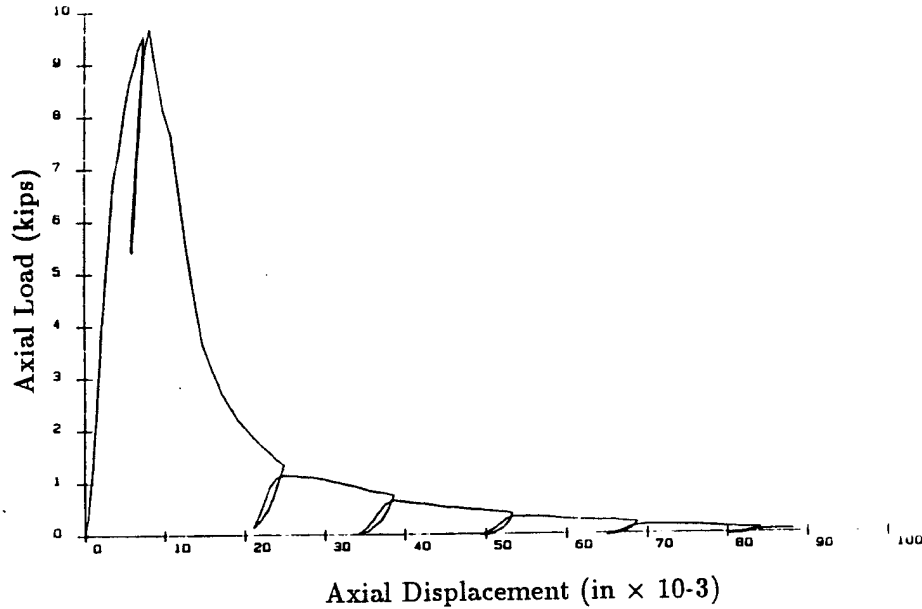
Figure 1.3. Measured cyclic stress-strain response for concrete showing degradation of the elastic modulus with increasing strain-softening.

model. The third model in Figure 1.2c is an example of an elasto-plastic damage model. Both permanent deformation and modulus reduction are modeled. APTEK's cap model with damage described in this report is an elasto-plastic damage model, and is used for modeling concrete response in the ductile (compressive pressure) regime.

Experimental evidence for modulus reduction is available in the literature, *e.g.* the cyclic stress-strain response from uniaxial compressive stress tests performed on concrete by Hurlbut is reproduced in Figure 1.3 from Reference 6. Note that the average slope from the loading/unloading loops decreases with increasing strain. Experimental evidence for modulus reduction from laboratory tests conducted by WES on White Sands Missile Range (WSMR-5) concrete is shown in Figure 1.4. In these tests, concrete cylinders were loaded in uniaxial strain to a pressure of 138 MPa and then unloaded. The damaged cylinder was then loaded in either direct pull or unconfined compression. Both sets of data indicate a substantial reduction in loading modulus and strength following preloading in uniaxial strain. Also shown in Figure 1.4 is the less damaging effect of preloading cylinders in isotropic compression (to a pressure of 138 MPA) prior to direct pull or unconfined compression tests.

We begin our discussion of the cap model with damage with a brief review of Simo and Ju's damage

3
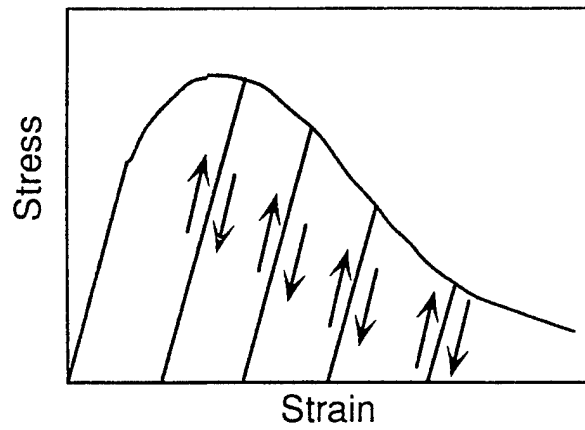
(a) Elasto-plastic or plasticity softening model.
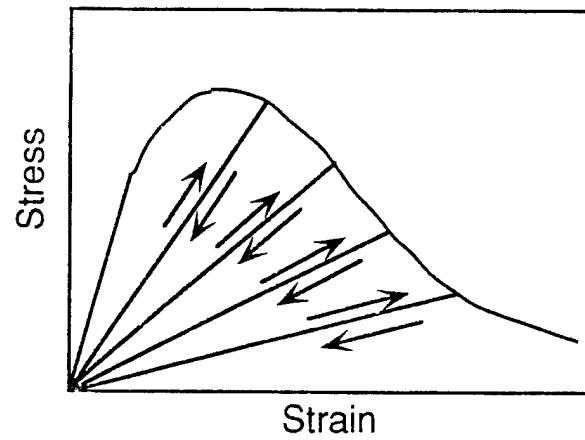
(b) Elasto-damage model.
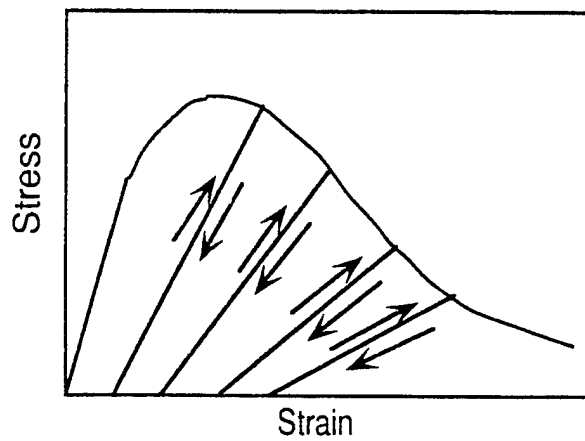
(c) Elasto-plastic damage model.

Figure 1.2. Comparison of material model behaviors.
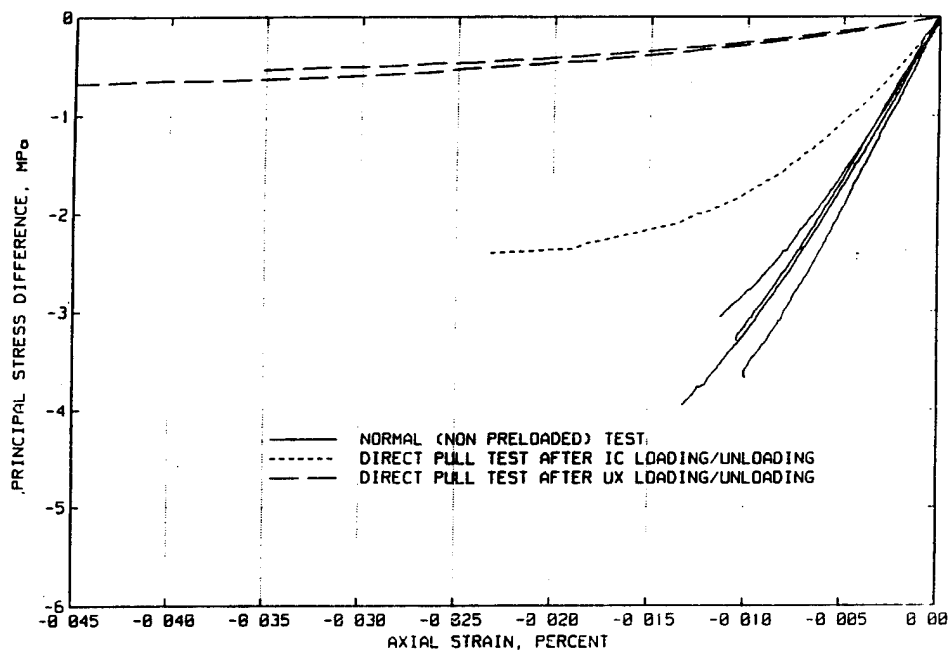
(a) Direct pull test data.
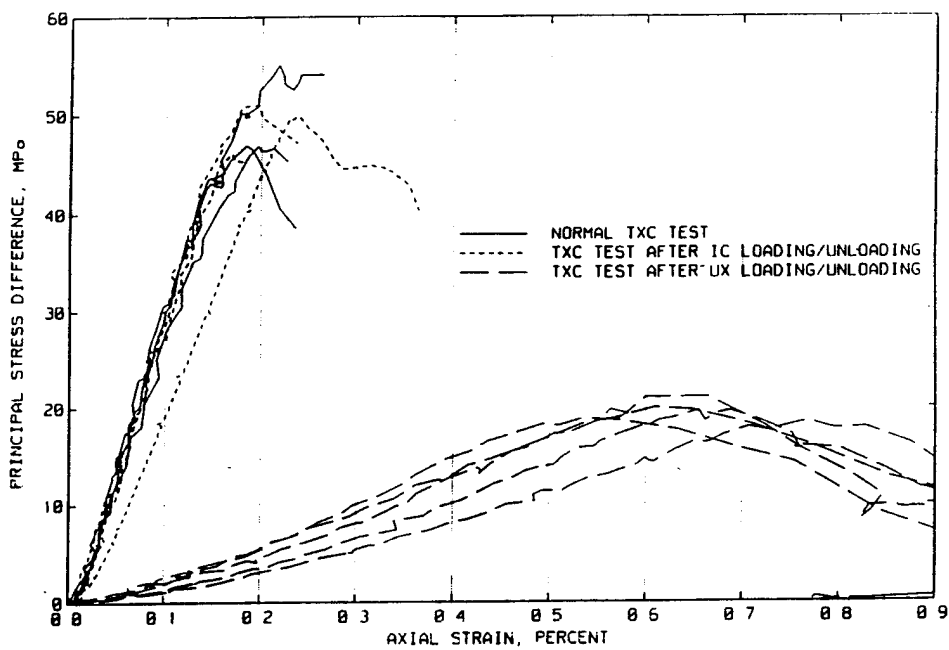
(b) Unconfined compression test data.

Figure 1.4. Reduction in modulus and strength following preloading in uniaxial strain for WSMR-5 concrete.

5

degradation formulation and details of our implementation into DYNA3D. Implementations for modeling ductile and brittle response are discussed separately in Sections 2 and 3. Our implementation for ductile response combines Simo and Ju's damage degradation formulation with the smooth-cap model implemented into DYNA3D by Pelessone in Reference 2, a three stress-invariant formulation developed by Rubin in Reference 7, and a Duvaut-Lions viscoplastic update algorithm developed by Simo *et.al.* in Reference 12. Our implementation for brittle response is a three-invariant elasto-damage simplification of the cap model in which plasticity is neglected. Other features of the implementation include modeling bulk modulus 'healing' to simulate opening and closing of cracks, and modeling dilation damage. These features are discussed in Sections 4 and 5, respectively. The implementation of these formulations into a cohesive model will henceforth be referred to as the APTEK concrete model.

Verification and validation of the concrete model is in progress for CWE applications. These applications include structural benchmark calculations and pre-test predictions for Dipole East structures[1]. The structural benchmark calculations are a series of four rounds of calculations, performed by participating analysts on the CWE program. The objectives of the Round A and B calculations are to compare and assess the participants models for plain concrete. These calculations examine the effect of mesh refinement on the predicted softening response and accumulation of damage for TXC simulations. The objectives of the Round C and D calculations are to compare the participants models for reinforced concrete. These calculations study the dynamics of reinforced slabs sections. Comparisons of all the participants computational results have been compiled by RDA and reported in a four volumes of viewfoils in References 8 through 11. Selected benchmark results are reported in Section 6-8.

---

[1]Predictions for Dipole East structures and Round E benchmarks will be reported in a future technical report.

SECTION 2

MODELING DAMAGE IN THE DUCTILE REGIME

Simo and Ju developed alternative strain- and stress-based damage models. Damage is directly linked to the history of strains (stresses) in the strain-based (stress-based) model. The strain-based and stress-based formulations are based on thermodynamic considerations, although they are not equivalent formulations.

We extended the elasto-plastic cap model to include Simo and Ju's strain-based damage formulation for modeling ductile response. Our terminology for ductile response is any state of stress in which the pressure is compressive. We choose to implement the strain-based formulation rather than the stress-based formulation for two reasons. First, the strain-based formulation is relatively easy to implement, as discussed in subsequent paragraphs, because it does not involve modification of the plasticity return mapping algorithm. Second, we felt a *strain-based* damage model is more likely to predict a "splitting mode", i.e. a cylinder subject to unconfined uniaxial compression develops cracks parallel to the axis of loading, due to the presence of tensile radial and hoop strains.

Although only the strain-based formulation has been implemented to date, future efforts should include review, and possibly implementation, of a stress-based damage model for comparison with the strain-based model. The relative merits and drawbacks of each type of formulation are of particular interest during preloading/unloading into compression (tension) and subsequent loading into tension (compression).

2.1 ISOTROPIC FORMULATION.

Simo and Ju base their strain-based damage model on the *effective stress concept* and the hypothesis of *strain equivalence*. This hypothesis states that "the strain associated with a damaged state under the applied stress is equivalent to the strain associated with its undamaged state under the effective stress." Let σ_{ij} be the stress tensor associated with the damaged state, and $\bar{\sigma}_{ij}$ be the effective stress tensor, or stress tensor associated with the undamaged state. A scalar damage parameter d

7

transforms the effective stress tensor into the stress tensor, as follows:

$$\sigma_{ij} = (1 - d)\bar{\sigma}_{ij} \tag{2.1}$$

The scalar damage parameter d ranges from zero for no damage and approaches unity for maximum damage. Thus $1 - d$ is a reduction factor associated with the amount of damage. One effect of the reduction factor $1 - d$ is to reduce the loading/unloading slope, or moduli, during cyclic loading. For linear elastic response, the bulk and shear moduli, K and G, are degraded isotropically. Another effect is to model the softening response observed in lab test data. A physical interpretation of the reduction factor $1 - d$ is the ratio of undamaged to nominal surface area at a material point. The effective stress $\bar{\sigma}_{ij}$ acts on the undamaged surface area while the total stress σ_{ij} acts on the nominal area.

It is helpful to refer back to the unconfined compression simulations previously shown in Figure 1.1 to visualize the relationship between the stress associated with the damaged (strain-softening) and undamaged (perfectly-plastic) states. The effective stress from Equation 2.1 is stress calculated for perfectly-plastic response in Figure 1.1. Thus the reduction factor $1 - d$ decreases with axial strain, and is equal the ratio of the stress calculated with damage (strain-softening) to the stress calculated without damage (perfectly-plastic).

2.2 EVOLUTION OF THE DAMAGE PARAMETER.

It is assumed that the damage parameter d depends on the history of total strains. In particular, d is a function of the undamaged energy norm, from which Simo and Ju define the *equivalent strain*, $\bar{\tau}$, as follows:

$$d \;=\; G(\bar{\tau}) \tag{2.2}$$

$$\bar{\tau} \;=\; \sqrt{2\Psi^0} \tag{2.3}$$

Here Ψ^0 is the undamaged elastic strain energy. For the linear elastic case, $\Psi^0 = \frac{1}{2} C_{ijkl} \epsilon_{kl} \epsilon_{ij}$, where C_{ijkl} is the undamaged linear elasticity tensor and ϵ_{ij} are the total strain components. One way of expanding Ψ^0 is:

$$\Psi^0 = \frac{1}{2} \left(\sigma_{11}^* \epsilon_{11} + \sigma_{22}^* \epsilon_{22} + \sigma_{33}^* \epsilon_{33} \right) + \sigma_{12}^* \epsilon_{12} + \sigma_{13}^* \epsilon_{13} + \sigma_{23}^* \epsilon_{23} \qquad (2.4)$$

where the stress tensor σ_{ij}^* is calculated from the total strains and undamaged moduli, K and G.

Damage accumulates when $\bar{\tau}$ exceeds a damage threshold, r, i.e. when $\bar{\tau}_{n+1} > r_n$. Here the subscripts n denote the nth time step in the finite element analysis. The initial damage threshold is denoted r_0. The damage threshold at each time step is held equal to the initial damage threshold ($r_n = r_0$) until $\bar{\tau}_{n+1}$ exceeds the initial value r_0. Once the initial damage threshold is exceeded, d_{n+1} is updated from Equation 2.2, $d_{n+1} = G(\bar{\tau}_{n+1})$, and a new damage threshold is updated as follows: $r_{n+1} = \bar{\tau}_{n+1}$. Thus the damage threshold increases as damage accumulates.

One functional form for G suggested by Mazars in Reference 13 is:

$$G(\bar{\tau}) = 1 - \frac{r_0(1 - A)}{\bar{\tau}} - A \exp^{[B(r_0 - \bar{\tau})]} \qquad (2.5)$$

A and B are material constants which are obtained from fits to laboratory test data. This functional form for G has been implemented into the APTEK concrete model. A plot of G versus $\bar{\tau}$ is shown in Figure 2.1 for $r_0 = 14.76$ psi$^{-1/2}$, $A = 0.8$ and $B = 0.015$ psi$^{-1/2}$. Note that $G = 0$ when $\bar{\tau} = r_0$ and G approaches one as $\bar{\tau}$ increases.

2.3 ALTERNATE FORMULATION.

The damage degradation model previously discussed in Section 2.1 models isotropic degradation of the moduli. This means that both the bulk and shear moduli are degraded simultaneously. However, the preload data previously shown in Figure 1.4 suggests that bulk modulus degradation may not be appropriate for modeling the response of concrete at low or moderate confining pressures. The data suggests that damage accumulates with increasing deviatoric strain or stress (uniaxial strain

9
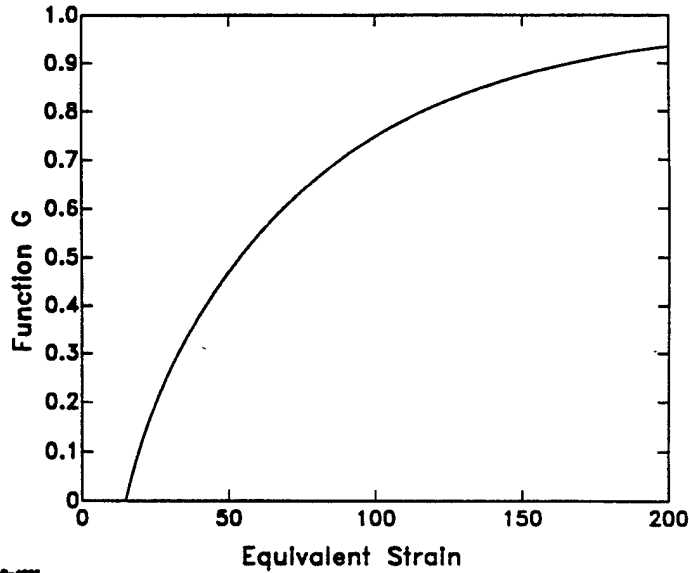
Figure 2.1. Increase in the damage function, G, with equivalent strain, $\bar{\tau}$.

preload) but not with increasing volumetric strain or pressure (isotropic compression preload). The data indicate a substantial reduction in loading modulus (Youngs's modulus) following preloading in uniaxial strain to a pressure of 138 MPa. However, the stress-strain responses from the unconfined compression test, measured with and without preloading in isotropic compression, are in reasonable agreement. The data do *not* indicate a reduction in loading modulus following preloading in isotropic compression to a pressure of 138 MPa.

To account for this behavior, APTEK modified[1] the concrete model to eliminate damage in isotropic compression, base damage on the accumulation of distortional strain energy, and degrad the shear modulus only. Let S_{ij} be the deviatoric stress tensor defined as follows:

$$S_{ij} = \sigma_{ij} - P\delta_{ij} \tag{2.6}$$

were σ_{ij} is the stress tensor, P is the pressure, and δ_{ij} is the Kronecker delta. Let $\bar{S}_{ij}$ be the effective deviatoric stress tensor associated with the undamaged state. The damage parameter d transforms

---

[1]This alternative formulation and the original isotropic formulation are separately maintained.

10

the effective deviatoric stress tensor into the deviatoric stress tensor, as follows:

$$S_{ij} = (1-d)\bar{S}_{ij} \qquad (2.7)$$

It is assumed that the damage parameter d depends on the history of the deviatoric strains. The damage evolution function and the equivalent strain, $\bar{\tau}_d$, are defined as follows:

$$d = G(\bar{\tau}_d) \qquad (2.8)$$

$$\bar{\tau}_d = \sqrt{2\bar{\Psi}^d} \qquad (2.9)$$

Here $\bar{\Psi}^d$ is the undamaged elastic distortional strain energy, defined in terms of the undamaged elastic strain energy, as follows: $\bar{\Psi}^d = \bar{\Psi}^0 - Ke_v^2$ where e_v is the volumetric strain. Damage initiates when $\bar{\tau}_d$ exceeds a user specified threshold, r_0, as follows: $\bar{\tau}_d > r_0$. Once the initial damage threshold is exceeded, d is updated from Equation 2.8 and the new damage threshold is set equal to the old (previously exceeded) value of $\bar{\tau}_d$.

2.4 APPLICATION TO A CAP MODEL.

We applied Simo and Ju's damage degradation formulation to a three-invariant, viscoplastic cap model. We obtained the original two-invariant, rate-independent formulation of the cap model from Pelessone in Reference 2 and implemented it into DYNA3D. This formulation is reviewed in Section 2.4.1. We extended this formulation to include the effect of the third deviatoric stress invariant on geologic material strength. The three-invariant model fits a wider range of laboratory test data than the two-invariant model. The three-invariant formulation was developed by Rubin in Reference 7 and is discussed in Section 2.4.2. Verification of the three-invariant formulation is given in Appendix C. We also added rate-dependence to the model through implementation of viscoplastic and viscodamage formulations. These implementations allow us to model an increase in strength as a function of strain rate. They were formulated by Simo and Ju in Reference 5 and are discussed in Section 2.4.4.

We also extended the cap model to include explicit dependence of the pressure-volumetric strain

11

(a) Smooth-cap.   (b) Non-smooth cap.
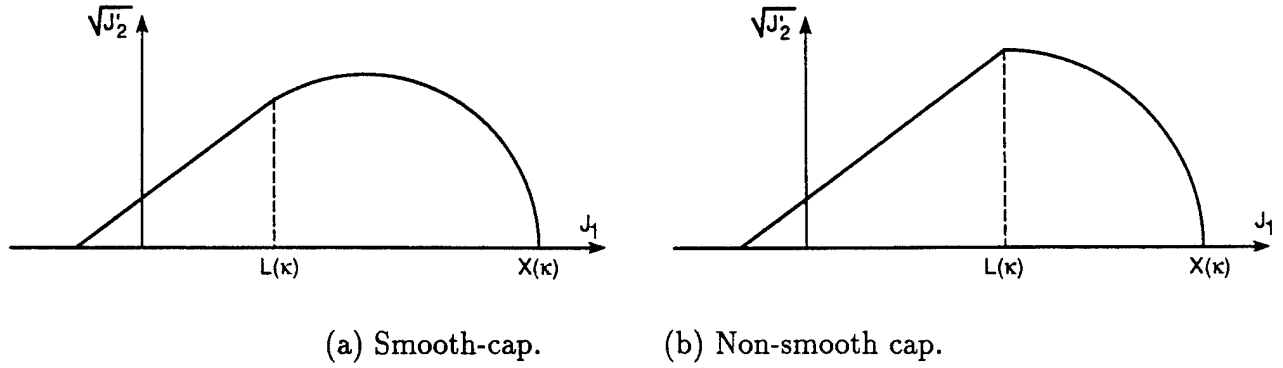
Figure 2.3. Comparison of the smooth-cap yield surface used in the APTEK concrete model with a non-smooth cap yield surface.

relation on the current porosity. The user has the option of requesting the explicit pore-compaction model or the original constant bulk modulus model. The explicit pore compaction model was developed for soils and is discussed in Appendix B. The constant bulk modulus model was used to model concrete in all our benchmark and internal detonation calculations.

2.4.1   Smooth-Cap Formulation.

The cap model proposed by Pelessone is a two-invariant plasticity model with a yield surface defined by a shear failure envelope, a moveable hardening cap, and a tensile cutoff. There is a continuous and smooth (no corners) intersection between the failure envelope and hardening cap, which eliminates the numerical complexity of treating a compressive 'corner' region between the failure surface and cap[2]. Hence we refer to Pelessone's cap model as a smooth-cap model. Figure 2.2 shows a three-dimensional view of a two-invariant cap model in principal stress space. Figure 2.3 shows a two-dimensional view in stress invariant space, along with a non-smooth yield surface for comparison. The nomenclature used in these figures will be explained in subsequent paragraphs.

The two-invariant model is described in terms of two stress invariants, $\bar{J}_1$ and $\bar{J}_2'$, were $\bar{J}_1$ is the first invariant of the stress tensor:

$$\bar{J}_1 = \sigma_{kk} = 3\bar{P} \tag{2.10}$$

---

[2] One goal of the cap model proposed by Pelessone was to improve the algorithmic implementation of the Simo-Ju-Taylor cap model previously implemented in the LLNL version of DYNA3D. In the Simo-Ju-Taylor model, the cap has a horizontal tangent that intersects the sloped failure surface in a non-smooth fashion, i.e. the cap and failure surface have different slopes. Hence special treatment must be given to the corner region formed by two lines normal to the cap and failure surfaces.

σ2

σ1
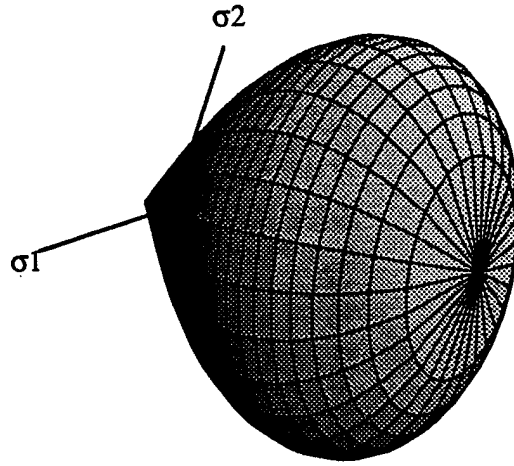
Figure 2.2. Two-invariant cap model in principal stress space.

and $\bar{J}_2'$ is the second invariant of the deviatoric stress tensor:

$$\bar{J}_2' = \frac{1}{2}\bar{S}_{ij}\bar{S}_{ij} \tag{2.11}$$

Here bars are used over the stresses and invariants to indicate *effective* quantities associated with the undamaged state in Equation 2.1.

The yield function of the two-invariant model is described in terms of the shear failure surface and hardening cap functions, F_f and F_c respectively, as follows:

$$f(\bar{J}_1, \bar{J}_2', \kappa) = \bar{J}_2' - F_f^2 F_c \tag{2.12}$$

Multiplying the cap ellipse function by the failure surface function allows the cap to take on the slope of the failure surface function at their intersection, as discussed in subsequent paragraphs. Thus the yield surface is described by a single smoothly varying function, f, as previously shown in Figure 2.3. Stress states inside the failure envelope, $f < 0$, are elastic states. Stress states on the envelope, $f = 0$, indicate that the material is yielding. Stress states outside the envelope, $f > 0$, are not allowed.

13

The shear failure surface is defined in terms of the first stress invariant as:

$$F_f(\bar{J}_1) = \alpha - \lambda e^{-\beta J_1} + \theta \bar{J}_1 \tag{2.13}$$

The material parameters α, λ, β, and θ are evaluated by fitting Equation 2.13 to experimental data ($\sqrt{J_2'}$ versus J_1) from TXC tests, and then adjusting these parameters to account for damage, as discussed in Appendix D.

The isotropic hardening cap $F_c(\bar{J}_1, \kappa)$ is a two-part function that is either unity (thus reducing the yield function to $F_f^2(\bar{J}_1)$ for the shear failure surface) or an elliptically shaped function for the cap with size and position (hardening) parameter κ. The cap surface is defined as:

$$F_c(\bar{J}_1, \kappa) = 1 - \frac{\left[\bar{J}_1 - L(\kappa)\right]\left[\mid \bar{J}_1 - L(\kappa) \mid + \bar{J}_1 - L(\kappa)\right]}{2\left[X(\kappa) - L(\kappa)\right]^2} \tag{2.14}$$

This function is displayed schematically in Figure 2.4. It is unity for $\bar{J}_1$ less than $L(\kappa)$ and elliptical for $L(\kappa) \leq \bar{J}_1 \leq X(\kappa)$. The hardening parameter κ that controls the motion of the cap surface, and $L(\kappa)$ and $X(\kappa)$ define the geometry of the cap. The function $L(\kappa)$ is the current value of $\bar{J}_1$ at the intersection of the cap and failure surfaces. The function $X(\kappa)$ is the current value of $\bar{J}_1$ at the intersection of the cap and the $\bar{J}_1$ axis. It is defined in terms of the cap ellipticity ratio R, where R is the ratio of its major and minor axes (parallel to the $\bar{J}_1$ to $\sqrt{\bar{J}_2'}$ axes), as follows:

$$X(\kappa) = L(\kappa) + RF_f(L(\kappa)) \tag{2.15}$$

where $L(\kappa)$ is defined by:

$$L(\kappa) = \begin{cases} \kappa & \text{if } \kappa > \kappa_0 \\ \kappa_0 & \text{otherwise} \end{cases} \tag{2.16}$$

Here κ_0 is the value of $\bar{J}_1$ at the *initial* intersection of the cap and failure surfaces. Note that Equation 2.16 restrains the cap from retracting past its initial location at k_0. This restraint is arbitrary and the implementation can be readily modified by the user to allow the cap to retract past its initial location, should such a modification be warranted by data. In fact, the user has the option of not allowing the cap to contract at all, which is often the desired option for modeling
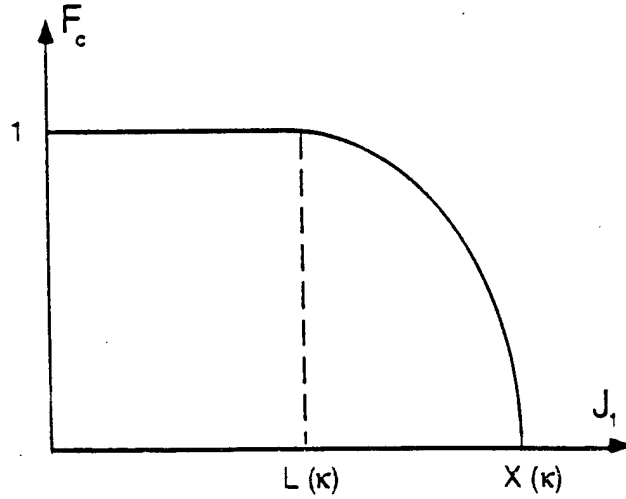
Figure 2.4. Two-part function used for the cap.

rock.

When plastic volume compaction or expansion occurs, the evolution of the cap's motion is defined by the hardening rule:

$$\epsilon_v^p = W \left(1 - e^{-D_1(X-X_0)-D_2(X-X_0)^2} \right) \tag{2.17}$$

where ϵ_v^p is the plastic volumetric strain, W is the maximum plastic volumetric strain, $X_0 = X(\kappa_0)$ is the initial abscissa intercept of the cap surface, and D_1 and D_2 are material parameters. The four parameters of the hardening rule are obtained from the pressure-volumetric strain curve from isotropic compression tests. The cap aspect ratio R is typically evaluated from a fit to the stress path from uniaxial strain data. A detailed description of how to fit the model to concrete data is given in Appendix D for the benchmark series of calculations.

2.4.2 Three Invariant Extension.

We extended the two-invariant smooth-cap model to include the well known dependence of geologic material behavior on the third invariant of the deviatoric stresses, J_3'. This extension uses a formulation published by Prof. Rubin in Reference 7. The three-invariant model describes more complete geologic material behavior from a wider range of laboratory test data than the two-invariant model.

Standard laboratory tests for measuring failure curves of geologic specimens include triaxial compression (TXC) and triaxial extension (TXE) tests. Such tests are conducted on cylindrical specimens and begin with hydrostatic compression, *i.e.* the axial compressive stress, σ_x, is equal to the radial
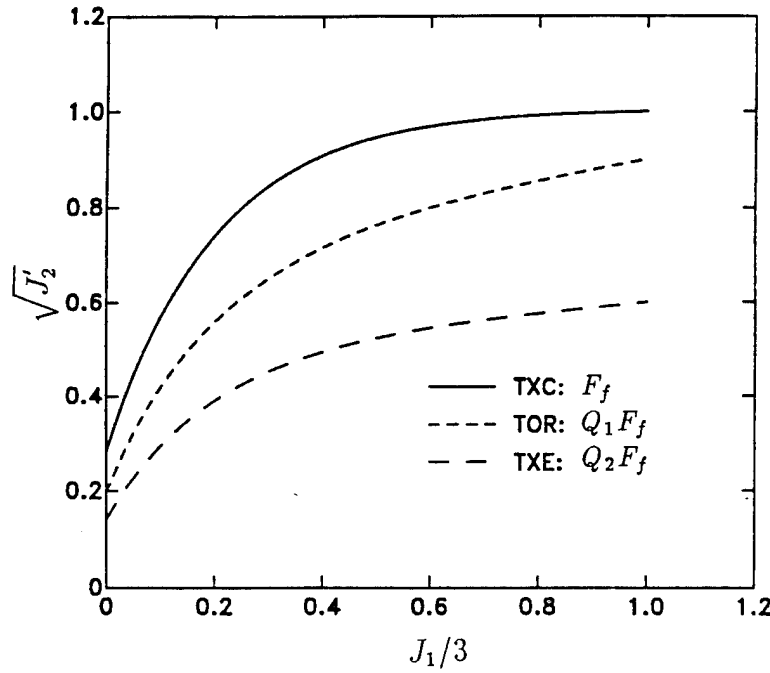
Figure 2.5. Schematic failure curves for triaxial compression (TXC), a deviatoric state of torsion (TOR), and triaxial extension (TXE).

compressive stress, σ_r. For TXC tests, the magnitude of the compressive stress is then quasi-statically *increased* until the specimen fails. For TXE tests, the magnitude of the compressive stress is quasi-statically *decreased* until the specimen fails. Typical failure curves, shown in Figure 2.5, are plotted as a stress difference quantity, $\sqrt{J_2'} = (\sigma_x - \sigma_r)/\sqrt{3}$, versus pressure, $J_1/3$. It is well known that geologic materials fail at lower values of $\sqrt{J_2'}$ for TXE tests than for TXC tests conducted at the same pressure. The failure surface functions F_f, Q_1, and Q_2 shown in this figure are discussed in subsequent paragraphs.

A two-invariant model cannot be simultaneously fit to measured failure curves from both TXC and TXE tests. Two-invariant models are typically fit to TXC data, although the choice of which data (TXC or TXE) to fit depends on the analyst's judgement and the availability of data. The advantage of the three-invariant model proposed by Rubin is that it can be simultaneously fit to measured TXC and TXE failure curves, as well as to a failure curve for a deviatoric state of torsion (TOR).

Figure 2.6 shows a three-dimensional view of a three-invariant cap model in principal stress space. Although a straight-line Mohr-Coulomb failure envelope is shown in Figure 2.6, our model is more general than shown because it allows the user to specify a nonlinear failure curve to describe the pressure dependence of the TXC curve (refer back to Equation 2.13). The difference between the

16
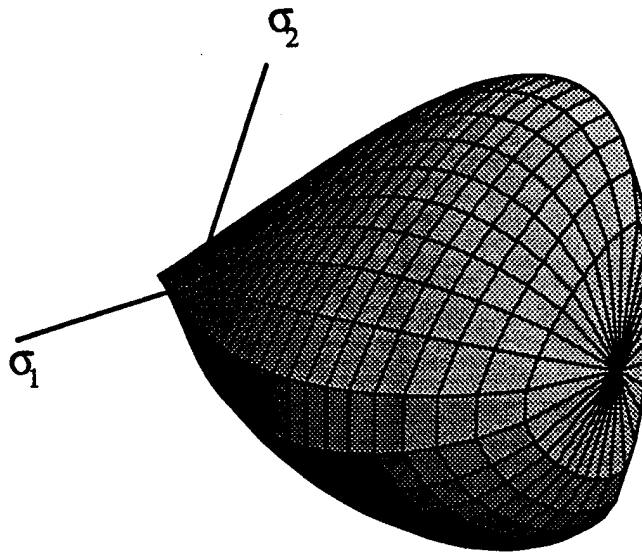
Figure 2.6. Three-invariant cap model in principal stress space.

two-invariant cap model previously shown in Figure 2.2 and the three-invariant cap model shown in Figure 2.6 is the shape of the yield function in the octahedral plane[3]. For the two-invariant model, the yield function forms a circle in the octahedral plane. For the three-invariant model, the yield function forms a hexagon (regular, semi-regular as shown, or irregular) in the octahedral plane.

Figure 2.7 depicts three common failure surfaces in the octahedral plane. The two-invariant model corresponds to the the circular surfaces, e.g. Mises-Schleicher or Drucker-Prager. The three-invariant model corresponds to the Mohr-Coulomb semi-regular hexagon. It is obtained fits to both TXC (point A) and TXE (point C) data. Although a straight-line is fit between the TXC and TXE states, the Rubin three-invariant formulation is general enough that the yield function may form an *irregular* hexagon-like shape in which each of the six sides is quadratic (rather than linear as shown) between the TXC and TXE states. Such a shape is obtained from fits to TXC, TOR, and TXE data.

The two-invariant model was extended to three invariants by modifying the yield function in Equa-

---

[3]The octahedral plane is a plane whose normal is the hydrostatic axis and makes equal angles with each of the principal axes of stress.
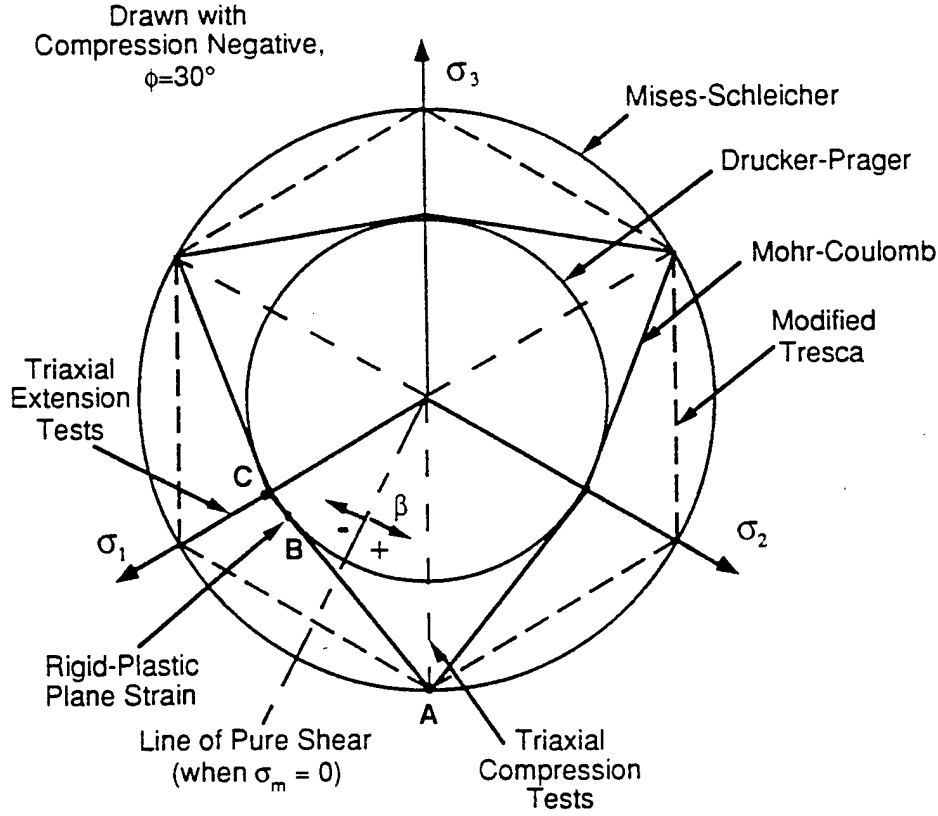
Figure 2.7. Three common failure surfaces in the octahedral plane.

tion 2.12, as follows:

$$f(\bar{J}_1, \bar{J}_2', \beta, \kappa) = \bar{J}_2' - \mathcal{R}^2 F_f^2 F_c \tag{2.18}$$

where $\mathcal{R}(\beta, \bar{J}_1)$ is a scaling function proposed by Rubin in Reference 7. The angle β is confined to the range $-\pi/6 \le \beta \le \pi/6$, and is related to the invariants $\bar{J}_2'$ and J_3' as follows:

$$\sin 3\beta = \hat{J}_3 = \frac{3\sqrt{3}}{2} \frac{\bar{J}_3'}{\bar{J}_2'^{3/2}} \tag{2.19}$$

in which $\bar{J}_3'$ is the determinant of the deviatoric stress tensor:

$$\bar{J}_3' = \frac{1}{3} \bar{S}_{ij} \bar{S}_{jk} \bar{S}_{ki} \tag{2.20}$$

$\hat{J}_3$ is a normalized invariant which remains in the range $-1 \le \hat{J}_3 \le 1$. For the standard laboratory

18

tests just discussed, the values[4] of β and $\hat{J}_3$ are:

$$\beta = \frac{\pi}{6}, \quad \hat{J}_3 = \quad 1 \quad \text{for TXC}$$
$$\beta = 0, \quad \hat{J}_3 = \quad 0 \quad \text{for TOR} \tag{2.21}$$
$$\beta = -\frac{\pi}{6}, \quad \hat{J}_3 = -1 \quad \text{for TXE}$$

The scaling function $\mathcal{R}$ in Equation 2.18 determines the strength of the material for any state of stress relative to the strength for TXC. This is demonstrated by referring back to Figure 2.5. Three functions of pressure are indicated, denoted F_f, Q_1, and Q_2. The function F_f is fit to the failure curve measured from TXC tests. The product functions $Q_1 F_f$ and $Q_2 F_f$ are fit to failure curves measured from TOR and TXE tests. Rubin develops an analytical expression for $\mathcal{R}$ in terms of experimental values for Q_1 and Q_2 as functions of pressure. This expression in given in Equation A.2 of Appendix A. The scaling function $\mathcal{R}$ takes on positive values less than or equal to one, and thus it scales the failure curve F_f for stress states other than TXC.

We choose to implement the following functional form for the scaling functions Q_1 and Q_2:

$$Q_1 = \alpha_1 - \lambda_1 e^{-\beta_1 J_1} + \theta_1 \bar{J}_1 \tag{2.22}$$
$$Q_2 = \alpha_2 - \lambda_2 e^{-\beta_2 J_1} + \theta_2 \bar{J}_1 \tag{2.23}$$

The eight material parameters ($\alpha_1, \lambda_1, \beta_1, \theta_1$, and $\alpha_2, \lambda_2, \beta_2, \theta_2$) are evaluated by fitting the product functions $Q_1 F_f$ and $Q_2 F_f$ to experimental data ($\sqrt{J_2'}$ versus J_1) from TOR and TXE tests, and then adjusting the parameters to account for damage. Minimum values are $Q_1 = 0.57735$ and $Q_2 = 0.5$. These minimum values define a triangle in the octahedral plane. Maximum values are $Q_1 = 1.0$ and $Q_2 = 1.0$. These maximum values define a circle in the octahedral plane. The Rubin three-invariant formulation allows the shape of the yield function in the deviatoric plane to transition with pressure from triangular, to irregular hexagonal, to circular.

The yield function provided by Equation 2.18 (with $F_c = 1$) reduces to the classical criteria of

---

[4]Stresses are assumed positive in compression.

Mohr-Coulomb and maximum-octahedral-shear stress for specific values of Q_1 and Q_2, and specific functional forms for F_f. The reduced forms of $\mathcal{R}$ are given in Appendix A. Verification of the three-invariant model for constant (pressure-independent) values for Q_1 and Q_2 is given in Appendix C. Reduction of the Rubin model to a Willam-Warnke model is also given in Appendix A. The Willam-Warnke model (Reference 15) is a commonly used model in which the shape of the yield surface in the deviatoric plane transitions with pressure: the Willam-Warnke model is a subset of the Rubin model.

2.4.3 Implementation Aspects.

The implementation of the damaged degradation formulation into finite elements models, such as the three-invariant cap model, is particularly simple because it makes use of an additive split of the the stress tensor into elastic-damage and plastic corrector parts. Damage evolution and plastic flow are treated as separate processes. The algorithmic formulation proceeds in two phases: an elastic-damage prediction in which the parameter d is updated, and a plastic return mapping phase in which the effective stresses, $\bar{\sigma}_{ij}$, are updated.

Damage Parameter Update. Let n denote the n_{th} time step in the finite element analysis. The first step in updating the damage parameter from d_n to d_{n+1} is to update the total strain tensor, ϵ_n, from the incremental strain tensor, $\Delta\epsilon$, as follows: $\epsilon_{n+1} = \epsilon_n + \Delta\epsilon$. Then one computes the equivalent strain according Equation 2.3 or Equation 2.9 as follows:

$$\bar{\tau}_{n+1} = \sqrt{2\Psi^0(\epsilon_{n+1})} \qquad \text{(isotropic)} \tag{2.24}$$

The updated damage parameter d_{n+1} and damage threshold r_{n+1} are then given by:

$$d_{n+1} = \begin{cases} d_n & \text{if } \bar{\tau}_{n+1} - r_n \leq 0 \\ G(\bar{\tau}_{n+1}) & \text{otherwise} \end{cases} \tag{2.25}$$

$$r_{n+1} = \max(r_n, \bar{\tau}_{n+1}) \tag{2.26}$$

20

Effective Stress Update. The effective stress components, $\bar{\sigma}_{ij}$ in Equation 2.1, are those stress components obtained from the elasto-plastic cap model without consideration of damage. The recovery of the effective stress components at the beginning of the time step is straight forward, *i.e.* $\bar{\sigma}_n = \sigma_n/(1 - d_n)$. Plastic response is formulated in effective stress space holding d_n constant.

The effective stress update to determine $\bar{\sigma}_{n+1}$ requires several steps. The first step is to check for yielding. This is done by by temporarily updating the effective stress components from the incremental strain rates by assuming that the entire strain increment is elastic. These updated stresses are called the elastic trial stresses, denoted $\bar{\sigma}_{n+1}^{trial}$. The value of the yield function in Equation 2.18 is valuated from the elastic trial stresses. The new stress state is an elastic stress state if $f \leq 0$ and a plastic stress state is $f > 0$.

If the stress state lies inside the failure surface ($f \leq 0$) then the elastic stress update is trivial, *i.e.* $\bar{\sigma}_{n+1} = \bar{\sigma}_{n+1}^{trial}$. If the stress state lies outside the failure surface ($f > 0$), then a return mapping algorithm, or plasticity algorithm, returns the stress state back to the failure surface so that $f = 0$. This is done by enforcement of the so-called plastic *consistency condition*, $\dot{f} = 0$, which may be expressed as:

$$\dot{f} = \frac{\partial f}{\partial \bar{\sigma}_{ij}} \dot{\bar{\sigma}}_{ij} + \frac{\partial f}{\partial \kappa} \dot{\kappa} \tag{2.27}$$

Here the superscript dot indicates differentiation with respect to time.

Enforcement of the consistency condition requires several assumptions. The first of these assumptions is that the total strain rate tensor, $\dot{\epsilon}_{ij}$, can be partitioned into elastic and plastic components:

$$\dot{\epsilon}_{ij} = \dot{\epsilon}_{ij}^{e} + \dot{\epsilon}_{ij}^{p} \tag{2.28}$$

The goal of the plasticity algorithm is to determine the plastic strain rate, $\dot{\epsilon}_{ij}^{p}$, thus identifying the partitioning.

The second assumption is that the plastic strain increment is normal to the yield surface:

$$\dot{\epsilon}_{ij}^{p} = \dot{\lambda} \frac{\partial f}{\partial \bar{\sigma}_{ij}} \tag{2.29}$$

21

where $\dot{\lambda}$ is a proportionality constant known as the consistency parameter. This assumption is known as an *associated* flow rule, or normality condition. Use of a potential function other than the yield function in Equation 2.29 results in a *nonassociated* flow rule. Recent studies reported in Reference 16 suggest that rate-independent models with nonassociated flow lead to spurious (non-unique) dynamic solutions, so only associated flow is implemented in the present model.

The third assumption defines the evolution relation for the moveable cap, known as the hardening rule:

$$\dot{\kappa} = \dot{\lambda}h(\bar{\sigma}_{ij}, \kappa) \tag{2.30}$$

where h is the plastic hardening law. For the smooth-cap model, we readily define h by equating the plastic volumetric strain rate, $\dot{\epsilon}_v^p$, derived from the flow rule in Equation 2.29 to that obtained from a first order Taylor series expansion of the hardening rule in Equation 2.17:

$$h(\bar{\sigma}_{ij}, \kappa) = 3 \left(\frac{\partial f}{\partial \bar{J}_1} \right) \Big/ \left(\frac{\partial \epsilon_v^p}{\partial k} \right) \tag{2.31}$$

One additional assumption is the form of the constitutive relation. For concrete, we assume Hooke's Law for an isotropic material:

$$\dot{\bar{\sigma}}_{ij} = C_{ijkl}(\dot{\epsilon}_{ij} - \dot{\epsilon}_{ij}^p) \tag{2.32}$$

where the elastic constitutive tensor C_{ijkl} from Reference 17 is given by:

$$C_{ijkl} = (K - \frac{2}{3}G)\delta_{ij}\delta_{kl} + G(\delta_{ik}\delta_{jl} + \delta_{il}\delta_{jk}) \tag{2.33}$$

For soil, another form of the constitutive relation is the explicit pore compaction model discussed in Appendix B.

The solution of the consistency condition in Equation 2.27 determines $\dot{\lambda}$, which in turn determines the partitioning of the total strain rate into elastic and plastic components. The $\dot{\lambda}$ solution is obtained from Equation 2.27 through substitution of the yield function in Equation 2.18, the flow rule in Equation 2.29, the hardening rule in Equation 2.31, and the assumed constitutive relation in Equation 2.32.

Details of the solution procedure are given in Reference 18 for the special case of $\mathcal{R}$ independent of $\bar{J}_1$ and a linear elasticity tensor, i.e. Hookes law with constant undamaged moduli K and G. For this special case, the expression for $\dot{\lambda}$ is:

$$\dot{\lambda} = \frac{(\partial_{\sigma_{ij}} f) C_{ijkl} \dot{\varepsilon}}{(\partial_{\sigma_{ij}} f) C_{ijkl} (\partial_{\sigma_{ij}} f) - (\partial_{\kappa} f) h} \tag{2.34}$$

with the compact notation

$$(\partial_{\sigma_{ij}} f) = \frac{\partial f}{\partial \bar{\sigma}_{ij}} \tag{2.35}$$

Details of the solution procedure for more sophisticated constitutive models, such as the explicit pore compaction model discussed in Appendix B, have not been summarized due to a shift in interest on the CWE program from modeling soils to modeling concrete. The effective bulk modulus used in the explicit pore compaction model varies with κ. Such dependence of the modulus on the hardening parameter must be taken into account in the solution procedure, but details are beyond the scope of this report.

2.4.4 Rate-Dependent Extensions.

Some existing experimental data shows that the peak stress attained during direct pull and unconfined compression tests is sensitive to the rate of loading or the strain rate. An example of such data from Reference 19 is reproduced in Figure 2.8. To accommodate such strain-rate sensitivity, APTEK implemented a rate-dependent model which requires one additional parameter, denoted by η. This parameter is called the fluidity coefficient, and the rate-dependent model is called a *viscoplastic* model. The original constitutive formulation is attributed to Duvaut and Lions in Reference 14.

Simo and Ju in Reference 4 suggest that the amount of microcracking (damage) exhibited by some materials at a particular strain level is retarded at higher strain rates, thus decreasing the nonlinearity of the stress-strain curve at higher strain rates. To model such behavior, they suggest implementation of a rate-sensitive *viscodamage* model which requires one additional damage fluidity coefficient, denoted by η_d. The viscoplastic and viscodamage extensions are discussed in the following paragraphs.
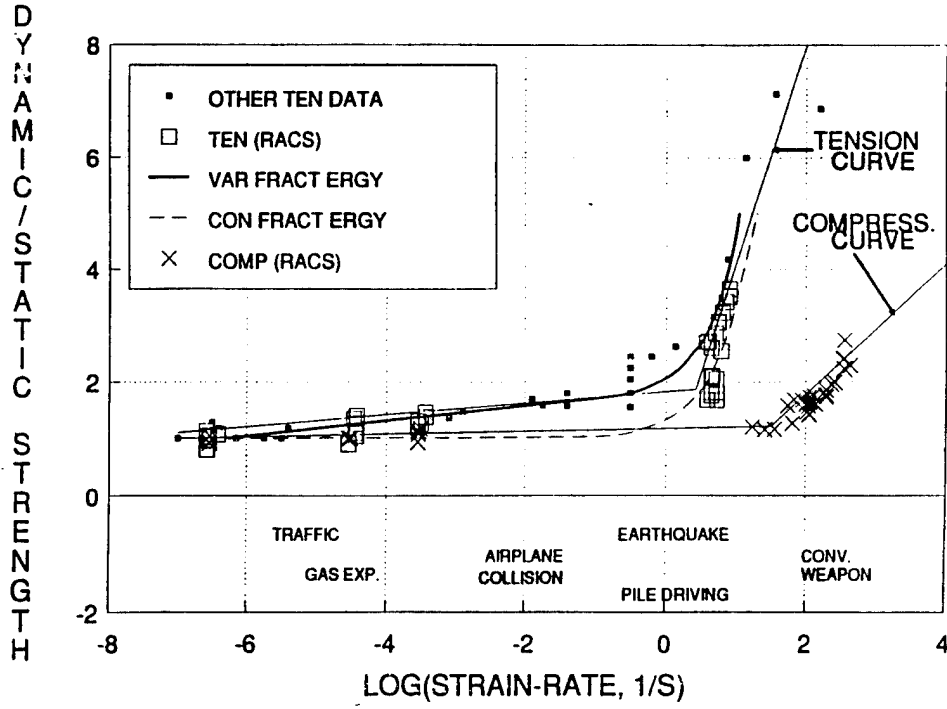
Figure 2.8. Measured rate-dependence of the peak stress attained in direct pull and unconfined compression tests.

Viscoplastic Extension. Simo *et.al.* in Reference 12 postulate a three-dimensional generalization of the Duvaut-Lions viscoplastic strain rate formulation as follows:

$$\dot{\epsilon}^{vp} = \frac{1}{\eta}C^{-1} : (\bar{\sigma} - \tilde{\sigma}) \tag{2.36}$$

where $\dot{\epsilon}^{vp}$ is the viscoplastic strain rate tensor, C is the elasticity tensor, and $\bar{\sigma}$ and $\tilde{\sigma}$ are the viscid and inviscid stress tensors, respectively. For simplicity, we will use bold symbols in this section to indicate tensors, *i.e.* $\sigma = \sigma_{ij}$, and the symbol ':' to indicate tensor contraction.

Simo *et.al.* extended the Duvaut-Lions formulation to multi-surface cap models by developing a closed-form, first order accurate update solution which accommodates an arbitrary number of internal state variables, such as the hardening variable κ. The update solution requires the corresponding solution of the inviscid elasto-plastic problem, which we denote as $\tilde{\sigma}_{n+1}$ and $\tilde{\kappa}_{n+1}$. The viscoplastic update solution also requires that the elastic trial stress, $\bar{\sigma}_{n+1}^{trial}$, be saved.

The update algorithm for the stress tensor is obtained by direct application of an implicit backward

Euler algorithm to the viscoplastic strain rate in Equation 2.36:

$$\bar{\sigma}_{n+1} - \tilde{\sigma}_{n+1} = \frac{\eta}{\Delta t} C : \Delta \epsilon^{vp} \tag{2.37}$$

$$= \frac{\eta}{\Delta t}(\bar{\sigma}_{n+1}^{trial} - \bar{\sigma}_{n+1}) \tag{2.38}$$

where use has been made of the stress updates:

$$\bar{\sigma}_{n+1}^{trial} = \bar{\sigma}_n + C : \Delta \epsilon \tag{2.39}$$

$$\bar{\sigma}_{n+1} = \bar{\sigma}_n + C : \Delta \epsilon^e \tag{2.40}$$

with

$$\Delta \epsilon^{vp} = \Delta \epsilon - \Delta \epsilon^e \tag{2.41}$$

Δt is the time step. Rearranging Equation 2.38 gives the update algorithm for the stress tensor:

$$\bar{\sigma}_{n+1} = \frac{\bar{\sigma}_{n+1}^{trial} + \Delta t/\eta \; \tilde{\sigma}_{n+1}}{1 + \Delta t/\eta} \tag{2.42}$$

Simo *et.al.* also derives a general update algorithm for the internal variables. Our interpretation of that algorithm for the hardening variable κ is:

$$\kappa_{n+1} = \frac{\kappa_n + \Delta t/\eta \; \tilde{\kappa}_{n+1}}{1 + \Delta t/\eta} \tag{2.43}$$

Note that the inviscid and elastic solutions can be obtained with these update algorithms. The inviscid solution ($\bar{\sigma}_{n+1} = \tilde{\sigma}_{n+1}$) is obtained from Equation 2.42 as $\eta \to 0$. This situation corresponds to the rate-independent solution. The elastic solution ($\bar{\sigma}_{n+1} = \sigma_{n+1}^{trial}$) is obtained as $\eta \to \infty$. This situation corresponds to the absence of plastic flow. At each timestep, the viscoplastic solution is bounded between the *current* rate-independent elasto-plastic solution and the elastic trial solution.

Numerous single element simulations were preformed for unconfined compression to determine the numerical relationship between strength enhancement, strain rate, and fluidity parameter. By strength enhancement we mean the ratio of the peak stress attained with viscoplasticity ($\eta > 0$)

relative to the peak stress attained without viscoplasticity ($\eta = 0$). We will refer to this ratio as the strength enhancement factor, SEF. Our simulations indicate that the calculated strength enhancement factor is nonlinearly related to the product of the strain rate times the fluidity parameter, $\dot{\epsilon}\eta$, as shown by the diamond symbols in Figure 2.9 for our WSMR-5 concrete model. The nonlinear relationship is material dependent and time-step independent. Note that Figure 2.9 provides a *calculated SEF* factor, whereas Figure 2.8 provides a *measured SEF* factor.

If a calculation is to be run at a constant strain rate, then the user can readily select a fluidity parameter value match the measured strength enhancement factor at that particular strain rate. However, the current strain rate in most calculations varies on an element-by-element and time-step by time-step basis. For such a case, we propose a method of internally calculating the fluidity parameter based on a user supplied function for the measured strength enhancement factor.

Suppose the measured strength enhancement vs. strain rate is formulated as follows:

$$SEF(\dot{\epsilon}) = \begin{cases} 1.29 - .059 * \log(\dot{\epsilon}) & \text{for } \dot{\epsilon} > 1.0e^{-5} \\ 0 & \text{otherwise} \end{cases} \tag{2.44}$$

where $\dot{\epsilon}$ is the effective strain rate:

$$\dot{\epsilon} = \sqrt{\frac{2}{3}\dot{\epsilon}'_{ij}\dot{\epsilon}'_{ij}} \tag{2.45}$$

and ϵ'_{ij} is the deviatoric strain:

$$\epsilon'_{ij} = \epsilon_{ij} - \frac{\epsilon_{kk}}{3}\delta_{ij} \tag{2.46}$$

This function is plotted in Figure 2.10 and can be obtained from a fit to rate-dependent data, such as the data previously shown in Figure 2.8. Equation 2.44 is the benchmark specification for WSMR-5 concrete.

Internally calculating the fluidity parameter is a two-step process. The first step is to calculate the specified SEF from Equation 2.44 (or Figure 2.10) given $\dot{\epsilon}$ in the element of interest. The second step is to back-calculate η from the specfied SEF and $\dot{\epsilon}$. This is done by fitting a functional form to the calculated SEF versus $\dot{\epsilon}\eta$ values previously shown in Figure 2.9. Then the product $\dot{\epsilon}\eta$ is back-calculated from this functional form, or equivalently, estimated from the graphical representation
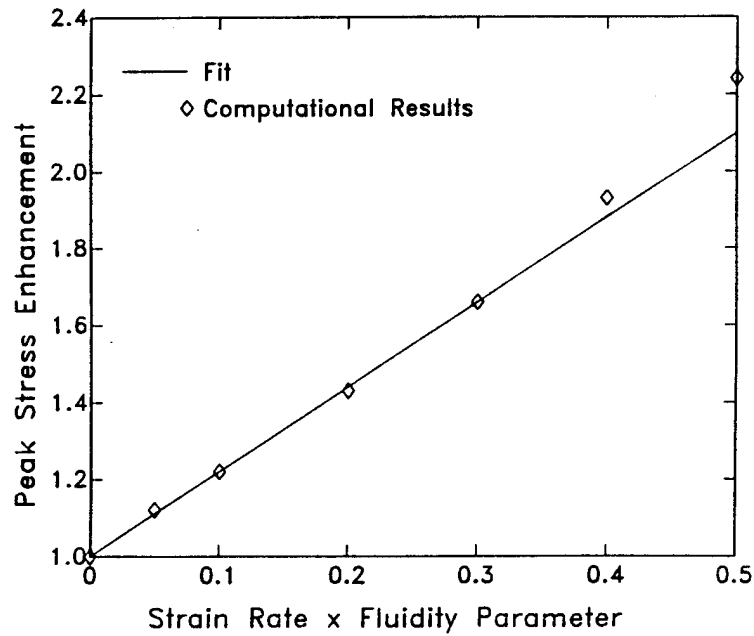
Figure 2.9. Calculated rate-dependent strength enhancement factor established from unconfined compression simulations for WSMR-5 concrete.
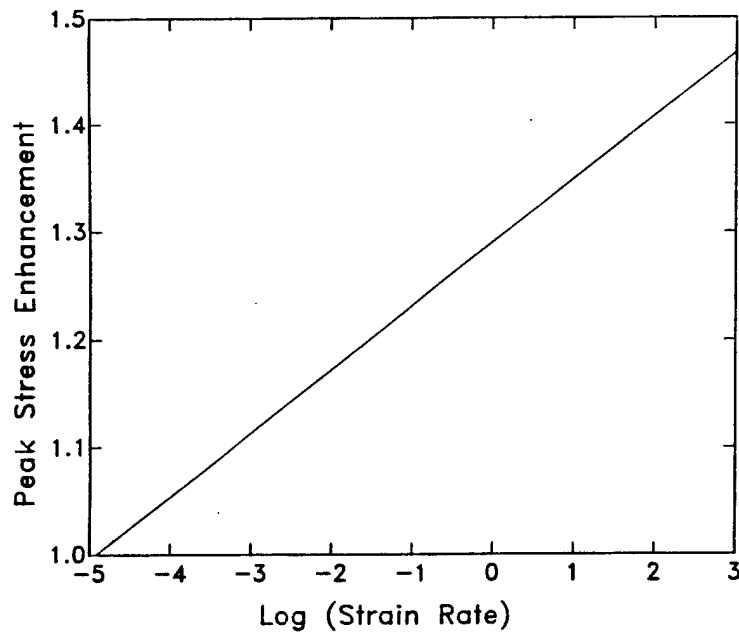
Figure 2.10. Benchmark specification for strength enhancement vs. strain rate estimated from measured data.

27

in Figure 2.9. The fluidity parameter η is readily derived from the product $\dot{\varepsilon}\eta$ because the strain rate $\dot{\varepsilon}$ is known.

Viscodamage Extension. Simo and Ju also developed a closed-form update algorithm in Reference 5 for *linear* viscous damage. Suppose $\bar{\tau}_{n+1} > r_n$ so that damage accumulation is predicted. The update algorithms for the damage parameter and damage threshold are:

$$d_{n+1} = d_n + \Delta r \frac{dG(\bar{\tau}_n)}{d\bar{\tau}} \tag{2.47}$$

$$r_{n+1} = r_n + \Delta r \tag{2.48}$$

where $\Delta r = \Delta\mu(\bar{\tau}_{n+1} - r_n)$. The parameter $\Delta\mu$ is derived from the damage fluidity coefficient, η_d, as follows:

$$\Delta\mu = \frac{\Delta t/\eta_d}{1 + \Delta t/\eta_d} \tag{2.49}$$

Both the instantaneous elasticity and inviscid damage solutions are obtained as limiting cases of the rate-dependent formulation. The instantaneous elasticity solution ($r_{n+1} = r_n$ and $d_{n+1} = d_n = 0$) is obtained as $\eta_d \to \infty$. The inviscid solution ($r_{n+1} = \bar{\tau}_{n+1}$ and $d_{n+1} = d_n + \Delta\bar{\tau}\frac{dG(\bar{\tau}_n)}{d\bar{\tau}}$) is obtained from Equation 2.48 as $\eta_d \to 0$. Hence the expansion of the damage surface ($r_n \leq r_{n+1} \leq \bar{\tau}_{n+1}$) is properly bounded between the instantaneous elasticity and the inviscid damage limit.

2.4.5 Single Element Elasto-Plastic Damage Calculation.

Results of a uniaxial compressive stress calculation under cyclic loading, which includes damage and plasticity, are given in Figure 2.11. The calculated stress-strain response captures the essential features of the measured response previously shown in Figure 1.3. No attempt was made to fit our model to this data because not enough information was available.

One feature of the damage model demonstrated in Figure 2.11 is strain-softening, which is a decrease in strength during progressive straining after a peak strength value is reached. Another feature is stiffness degradation. The average slopes of the loading/unloading curves decrease with increased straining, which indicates progressive degradation of the elastic moduli. The damage parameter d
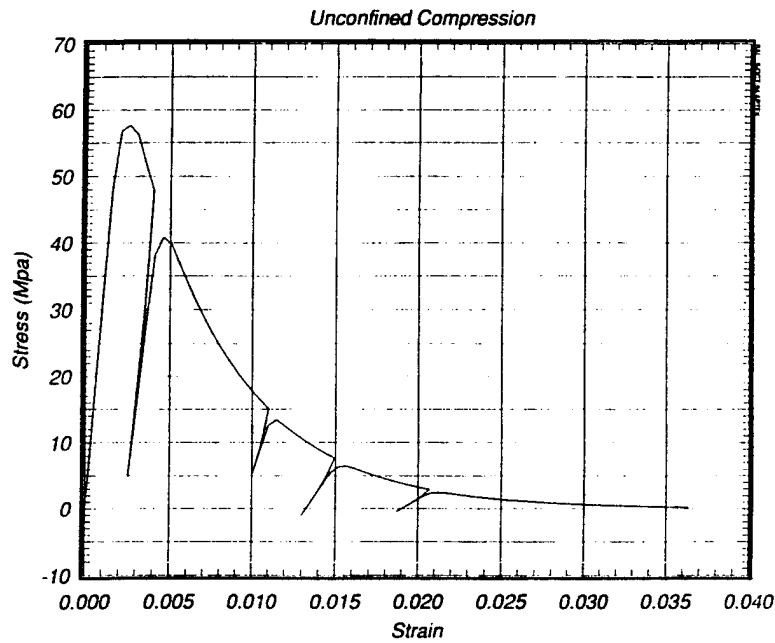
Figure 2.11. Uniaxial compressive stress calculation showing softening and degradation of the elastic moduli with increased straining.

remains constant during unloading and reloading because unloading reduces the equivalent strain below the damage threshold. Also note that permanent plastic strains occur upon unloading.

This example calculation is intended to demonstrate pertinent features of the damage model but the model parameters were not obtained from a fit to laboratory test data. Fits of the model to WSMR-5 concrete data are given in Section 7 for benchmark calculations.

29

SECTION 3

MODELING DAMAGE IN THE BRITTLE REGIME

Of great importance to the CWE program is the behavior of concrete in the low confining pressure and tensile (brittle) regimes. We define the brittle regime as any state of stress in which the pressure is tensile. Pelesonne's original cap model included implementation of a tensile pressure cutoff model. This model set the stress equal to zero (over one time step) once the pressure cutoff value was exceeded. We used this model for the Round A and B benchmarks, and for analysis of a Dipole East structure (DEINT-3). However, our DEINT-3 calculation did not correlate well with the test data because the one-step reduction in tensile strength was too severe. We obtained better correlations in subsequent structural response calculations (Large Test Structure 1 and the Precision Wall Test) by controling the rate of softening in the brittle regime.

To improve the model in this regime, and to meet the benchmark specifications, we eliminated the tensile cutoff portion of the model and implemented an elasto-damage model for brittle response (plasticity is neglected). Our damage model in the brittle regime ($P < 0$) was specifically formulated to meet all of RDA's peak stress specifications for the Round D and E benchmark series of calculations. These specifications are given in Table 3.1 and indicate that the maximum principal stress cannot exceed a peak stress of 3.2 MPa. WSMR-5 test data in the brittle regime was limited to the axial stress-strain response for direct pull, measured with and without the effects of preloading in uniaxial strain and isotropic compression. This data was previously shown in Figure 1.4. Hence the peak stress specifications listed in Table 3.1, other than direct pull, were subjectively selected by RDA to provide a complete (three-invariant) failure surface.

Table 3.1. RDA's benchmark specifications in the brittle regime.

Simulation	Peak Stress (MPa)
Direct Pull	3.2
Pure Shear	3.2
Equal Biaxial Tension	3.2
Equal Triaxial Tension	3.2

3.1 STRESS-BASED FORMULATION.

Simo and Ju formulate an *anisotropic* model for brittle response in Reference 4 which requires second- and fourth-order *tensor* damage variables[1]. However, we chose to loosely base our brittle damage model on their *isotropic* formulation in Equation 2.1, due to its efficiency and simplicity through use of a *scalar* damage variable. In addition, we choose to neglect plastic response in the brittle regime, due to the limited availability of *stress-strain* data. In particular, no data was provided on lateral strains or post-peak axial softening response. Neglecting plasticity makes the model more run-time efficient, which is an advantage when performing complex analyses, such the the Dipole East series of calculations. At the same time, we can readily fit the elastic-damage model to the limited set of WSMR-5 data and meet all of RDA's peak stress specifications.

To model the elastic-damage response in the brittle regime, the user specifies the peak stress, which in this case is $\sigma_{max} = 3.2$ MPa, and two parameters (A_b and B_b) which regulate the post-peak softening response according to Equation 2.5. Damage initiates when an energy norm, $\bar{\tau}_b$, exceeds an initial threshold, r_0.

Unlike the pressure independent threshold supplied by the user for the ductile model, the threshold for the brittle model is pressure dependent. This is necessary to meet the benchmark specifications. The initial damage threshold is calculated from the user-supplied peak stress specification and undamaged elastic moduli, as follows:

$$r_0 = \sqrt{\frac{\mathcal{R}^2 Y_T^2}{3G} + \frac{\bar{P}^2}{K}} \tag{3.1}$$

where $\mathcal{R}$ is the value of the Rubin function for the three-invariant formulation, which is $\mathcal{R} = 0.5$ for the benchmark specifications in the brittle regime, and Y_T is a function of pressure which describes the failure (peak stress) surface, as follows:

$$Y_T = 3(\bar{P} + \bar{\sigma}_{max}) \quad \text{for} \quad -\bar{\sigma}_{max} \le \bar{P} < 0 \tag{3.2}$$

---

[1]Their elastic-damage moduli tensor is non-symmetric for the anisotropic model, and thus damage is directional in nature. The elastic-damage moduli tensor is symmetric for the isotropic model.

The pressure dependent threshold in Equation 3.1 is a departure from the work of Simo and Ju. A simpler approach would be to specify a pressure-independent threshold, *i.e.* a constant value for r_0, as discussed in Section 3.2. Although the WSMR-5 direct pull test data could readily be modeled with a pressure-independent threshold, we could not meet the benchmark specifications.

The current value of the energy norm is calculated from the effective stress invariants, $\bar{J}_2'$ and $\bar{P}$, and the undamaged elastic moduli, as follows:

$$\bar{\tau}_b = \sqrt{\frac{\bar{J}_2'}{G} + \frac{\bar{P}^2}{K}} \qquad (3.3)$$

Once the initial damage threshold is exceeded, *i.e.* $\bar{\tau}_b > r_0$, then the updated value of the scaler damage parameter is calculated from Equation 2.5 (with $A = A_b$, $B = B_b$, and $\bar{\tau} = \bar{\tau}_b$), the elastic-damage stresses are updated from Equation 2.1, and the new threshold for damage is increased to the current value of $\bar{\tau}_b$. The algorithmic update is given by Equations 2.25 and 2.26 in which $\bar{\tau}_{n+1}$ is replaced by $\bar{\tau}_{b\ n+1}$. Note that the effective stresses in Equation 2.1 are simply the linear elastic stresses.

Our brittle damage criterion ($\bar{\tau}_b > r_0$) is a *stress-based* criterion, in which damage is linked to the history of the undamaged stress invariants. We could just as easily have implemented a *strain-based* criterion in which damage accumulates according to an energy norm of the strain tensor. Because we are not modeling plasticity in the brittle regime, the strain-based approach is identical to the stress-based approach for the direct pull test simulations given in Figure 3.1. However, the two approaches are *not* identical for cases in which samples are preloaded into the ductile ($P > 0$) regime, causing plastic response to occur before loading in the brittle ($P < 0$) regime. A pressure-independent strain-based model was used in the Round C benchmarks and is briefly discussed in the next section. Preload effects, and the applicability of strain-based versus stress-based models, will be examined in a future effort.

3.2 STRAIN-BASED FORMULATION.

The brittle damage formulation previously discussed in Section 3.1 is a stress-based, isotropic formulation. An alternate, but not necessarily equivalent approach, is to use a strain-based formulation. Our alternate approach is based on a simplification of Simo and Ju's *anisotropic* formulation, in which we degrad K but not G. This alternate formulation was used in the Round C benchmark calculations prior to RDA's specification of a maximum principal stress criterion.

To model damage in the brittle regime, the user specifies an initial damage threshold, r_0, and two parameters ($A = A_b$ and $B = B_b$) which regulate the post-peak softening response according to Equation 2.5. The brittle damage threshold is pressure-independent, and damage initiates when an energy norm, $\bar{\tau}_b$, exceeds the initial threshold, r_0. The energy norm is based on the tensile volumetric strain, ϵ_v^+, as follows: $\bar{\tau}_b = \sqrt{K\epsilon_v^{+2}}$. Hence damage initiates and accumulates when the volumetric strain is tensile, rather than when the pressure is tensile.

This formulation predicts damage accumulation with dilation for TXC simulations with low or no confining pressure. In such a case, our implementation compares the damage accumulated by brittle and ductile models and selects the maximum damage parameter as the operative parameter.

3.3 RATE-DEPENDENT EXTENSIONS.

One method of modeling rate dependence of the strength is the viscodamage extension previously described in Section 2.4.4. Another method of modeling rate dependence of the strength is to scale the initial damage threshold previously given in Equation 3.1 as a function of strain rate. This is a simple two-step process. First, the strength enhancement factor is calculated from Equation 2.44 given the effective strain rate in the particular element of interest. Second, the initial damage threshold, r_0 is scaled by the strength enhancement factor. The viscoplastic extension is not applicable to the brittle regime because we neglected plasticity.

Single element simulations, with and without rate-dependence of the strength, are given in Figure 3.1 for the direct pull benchmark specification. Rate-dependence was modeled by scaling the initial damage threshold. We used initial undamaged moduli of $K = 15520$ Mpa and $G = 13890$ Mpa for
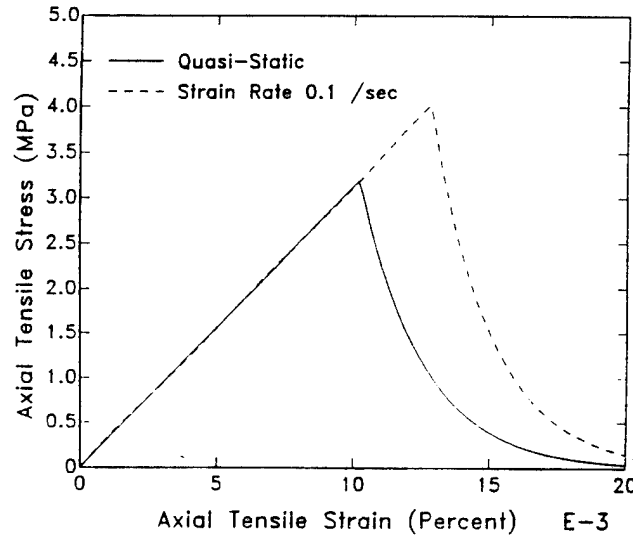
Figure 3.1. Direct pull test simulations.

these simulations, which are linear to the peak stress. We choose softening parameters of $A = 1.0$ and $B = 300$ MPa$^{1/2}$ to provide rapid degradations in strength. One approach in selecting the softening parameters is to relate the area under the calculated stress-displacement curve to the measured fracture energy of concrete, G'_f, which is often times available in the literature.

3.4 MODELING PRE-PEAK DEGRADATION.

In addition to modeling post-peak degradation, the user has the option of modeling pre-peak degradation, or hardening, which is evident in the WSMR-5 direct pull test data previously shown in Figure 1.4a. Pre-peak hardening can be modeled by appropriate selection of the maximum stress parameter, σ_{max}, and the softening parameters, A_b and B_b. A comparison of three direct pull simulations is shown in Figure 3.2. The solid line simulations use a peak stress of $\sigma_{max} = 3.2$ MPa. The dashed line simulation uses the same moduli as the solid line simulation, but a lower maximum stress of $\sigma_{max} = 2.8$ MPa and less severe softening parameters. Note that all simulations exhibit a peak stress of 3.2 MPa, although pre-peak hardening and more gradual post-peak softening are observed in the dashed line simulation.

Although pre-peak hardening can be modeled with the present implementation of the brittle damage model, as just demonstrated, numerous iterations may be required to fit the model to data. This is because the user specifies a threshold of $\sigma_{max} = 2.8$ MPa while trying to simulate a peak stress of 3.2 MPa. In addition, the model lacks flexibility because there is a trade-off between

34
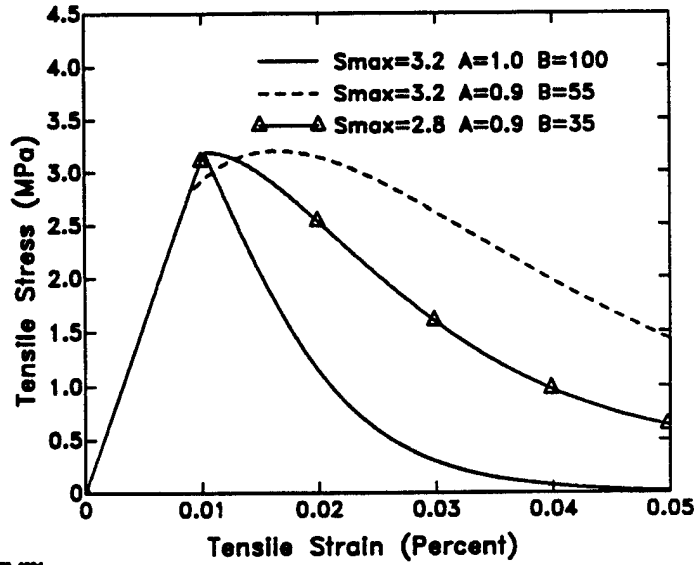
Figure 3.2. Effect of parameter selection on hardening and softening response.

modeling pre-peak damage and the severity of the post-peak softening response. To overcome these drawbacks, the modification described in the next paragraph is proposed, and recommended for future implementation.

In our proposed modification, the user specifies two additional parameters, F and d_0. The parameter F is the pre-peak damage threshold, specified as a fraction of the maximum stress σ_{max}, where $0 < F \leq 1$. The parameter d_0 is the amount of pre-peak damage, specified as a fraction of the total damage. For example, $F = 0.6$ and $d_0 = 0.15$ indicate that damage initiates at a stress of $0.6\sigma_{max}$ and the moduli are degraded 15% prior to attaining a peak stress of σ_{max}.

Modeling pre-peak damage using such an approach requires implementation of a pre-peak damage function, as well as modification of the damage function previously given in Equation 2.5 for modeling post-peak response. The pre-peak damage function is:

$$d = \frac{\bar{\tau}_b - F r_0}{(1 - F) r_0} d_0 \quad \text{for} \quad F r_0 \leq \bar{\tau}_b < r_0 \tag{3.4}$$

Note that d in Equation 3.4 varies linearly with $\bar{\tau}_b$, i.e. $d = 0$ at $\bar{\tau}_b = F r_0$ and $d = d_0$ at $\bar{\tau}_b = r_0$.

Post-peak degradation is readily modeled as follows:

$$d = d_0 + (1 - d_0)(1 - \frac{(1 - A_b)r_0}{\bar{\tau_b}} - A_b \exp^{B_b(r_0 - \bar{\tau_b})})$$ (3.5)

36

SECTION 4

MODELING CRACK OPENING AND CLOSING

We also implemented a feature to allow recovery ('healing') of the bulk modulus during cyclic loading between the brittle and ductile regimes. This feature is intended to simulate opening (bulk modulus degradation) and closing (bulk modulus recovery) of cracks. Our assumption is that any existing microcracks will close under compressive pressure (volumetric strain), but will initiate, grow, and coalesce under tensile pressure (volumetric strain).

Bulk modulus recovery is modeled with both the stress-based and strain-based brittle formulations previously discussed in Sections 3.1 and 3.2. For the stress-based (strain-based) model, we set the brittle damage parameter equal to zero ('healing') any time the pressure (volumetric strain) becomes compressive. We set the brittle damage parameter back to it previous value, and allow further brittle damage accumulation, any time the pressure (volumetric strain) becomes tensile.

A Round D benchmark calculation predicting 'healing' during dynamic bending of a reinforced concrete slab is given in Section 8. A simpler example calculation showing cyclic loading between the brittle and ductile regimes is presented in Figure 4.1. Loading into the brittle regime and subsequent degradation are simulated, with isotropic damage accumulation of $d = 0.3$. Moduli K and G are degraded 30% from their initial undamaged values. Now continue this simulation with loading into the ductile regime. The shear modulus G will retain its degraded value, but the bulk modulus K will recovery its initial undamaged value. Hence the damage is no longer isotropic. Although additional degradation of G may occur in the ductile regime, no degradation of K is allowed. If we continue this simulation with loading back into the brittle regime, isotropic damage accumulation will be recovered. For this example, the values of K and G will be 30% less than their initial undamaged values.
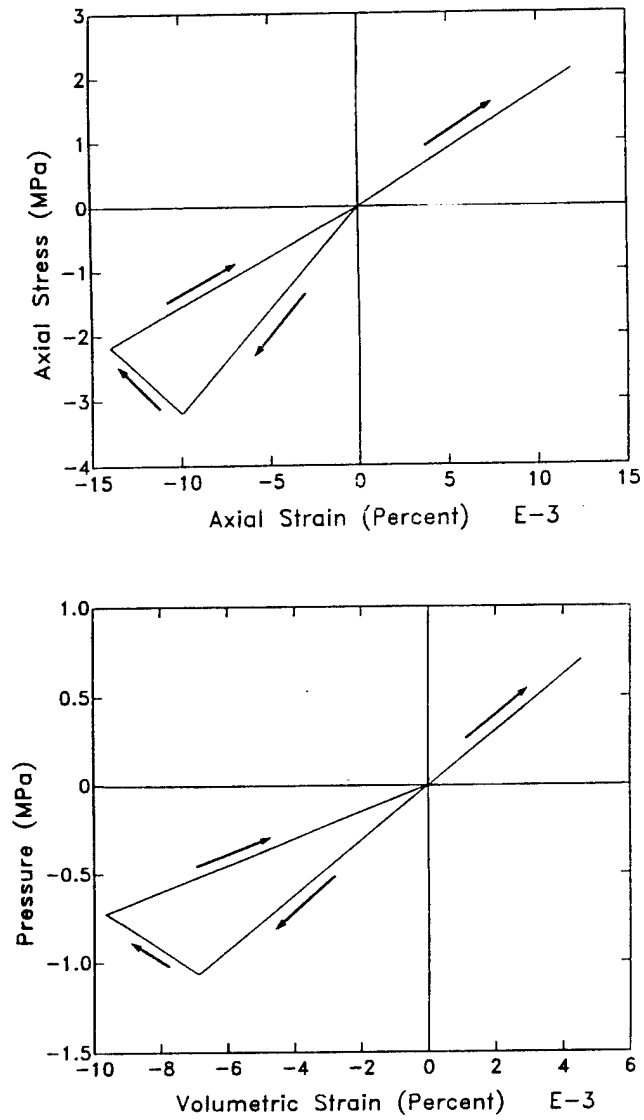
Figure 4.1. Demonstration of bulk modulus 'healing' during cyclic loading between the brittle and ductile regimes.

SECTION 5

MODELING DILATION DAMAGE

Volume expansion under compressive loading is commonly measured in concrete specimens during TXC tests with little or no confining pressure. Such tests also exhibit more severe softening than TXC tests conducted at higher confining pressure. Hence it is possible that the presence of volumetric tensile strain (or possibly lateral tensile strain) contributes to the more severe softening observed in TXC tests conducted at low confining pressure. We also believe that dilation behavior is critical in Mode II (shear) failure.

We implemented a dilation damage formulation to model an increase in the severity of damage when volume expansion occurs. This model is used in conjunction with the stress-based brittle model previously described in Section 3.1. This model is not used with the strain-based brittle model, because the strain-based model already accounts for dilation damage.

Dilation damage initiates when the pressure is compressive ($P > 0$), the volumetric strain is tensile, and the volumetric strain exceeds a dilation damage threshold. The damage threshold is $r_0 = \sqrt{K \epsilon_{v\ max}^2}$ where $\epsilon_{v\ max} = \sigma_{max}/K$ is the maximum volumetric strain allowed during isotropic tension simulations. Two softening parameters are user specified ($A = A_d$ and $B = B_d$ in Equation 2.5) to model the strain-softening response. The effective strain, $\bar{\tau} = \bar{\tau}_d$ in Equation 2.5, is $\bar{\tau}_d = \sqrt{K \epsilon_v^2}$ where ϵ_v is the current value of the volumetric strain. Dilation damage can be neglected by appropriate selection of the softening parameters ($A_d = 1$ and $B_d = 0$).

The softening responses of two unconfined compression simulations are compared in Figure 5.1 with and without dilation damage. Note that more degradation is modeled with dilation damage than without dilation damage.
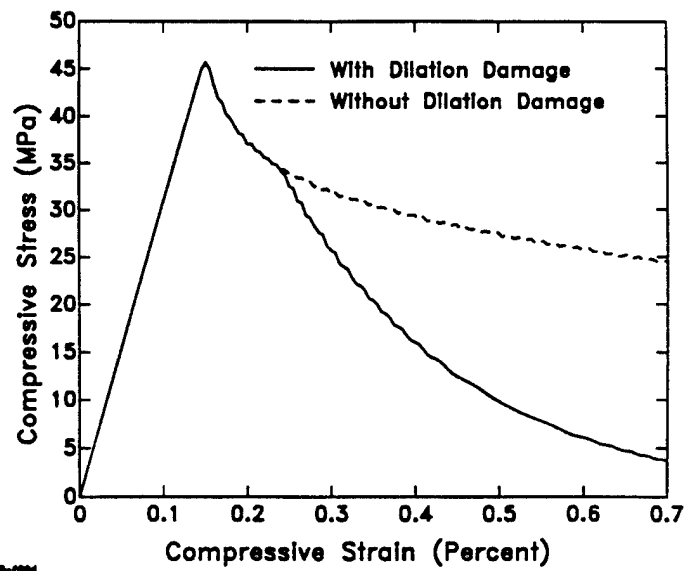
Figure 5.1. Comparison of unconfined compression simulations with and without modeling dilation damage.

SECTION 6

ROUND A BENCHMARKS: LABORATORY TEST SIMULATIONS

The Round A calculations consists of two groups of calculations, called Groups 1 and 2. The Group 1 calculations are single element fits to axial stress-strain data from TXC and TXE tests of plain concrete, for confining pressures between 0 and 100 MPa. These calculations demonstrate our fitting procedure for the isotropic damage model. The Group 2 calculations are multi-element, laboratory test simulations of an unconfined TXC test. These studies use the fit obtained from the Group 1 studies and demonstrate that rate-independent multi-element simulations predict more severe softening than single element models. Multi-element simulations also predict diagonal damage patterns and splitting, which are typical failure modes of concrete test specimens. These modes are not predicted with single element models. Although it is efficient to fit concrete data with single element models, such fits should be considered preliminary. The goodness of these preliminary fits should be evaluated using multi-element lab test simulations.

6.1 SINGLE ELEMENT FITS TO PIECEWISE-LINEAR DATA REPRESENTATIONS.

RDA provided the benchmark calculators with piecewise-linear representations of concrete laboratory test data, rather than with the actual data curves. RDA's representations of the data will be referred to as 'data' through-out the remainder of this section.

The single element in the Group 1 benchmark calculations is modeled 10 cm high by 5 cm square. The element was loaded first in hydrostatic compression. Then the element was further compressed in the axial direction using prescribed axial velocities, while the confining pressure load was held constant. The calculations were run at a slow strain rate of 0.001/s to avoid dynamic effects.

Single element fits of the model to TXC data are given in Figures 6.1-6.6 and to TXE data in Figure 6.7. The fitting procedure is described in detail in Appendix D. Four main features of the

41

1−TXC−0
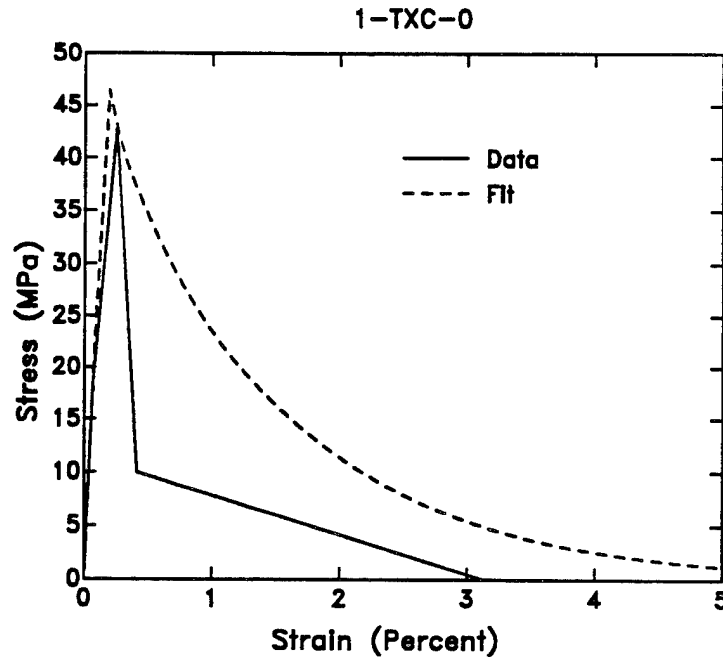
Figure 6.1. Fit of model to TXC data without confining pressure.

fit are discussed here:

- The initial elastic response following hydrostatic compression;

- The 'hardening' behavior, which we define as the nonlinear response prior to the peak stress;

- The peak stress and the strain at which the peak stress occurs;

- The 'softening' behavior, which is a decrease in stress beyond the peak stress with an increase in strain.

The data in these figures is plotted as axial stress versus axial strain. The data for the confined TXC tests is trilinear prior to the peak stress. The first linear segment (not apparent at low confining pressure) corresponds to the intial hydrostatic compression of the specimen. The second linear segment is the initial elastic response, while the third segment provides the hardening response to peak stress. The softening behavior following the peak stress is bilinear until a constant residual stress is attained. The reader should keep in mind that 'real data' does not behave in a piece-wise linear manner.

42

Figure 6.2. Fit of model to TXC data for 5 MPa confining pressure.
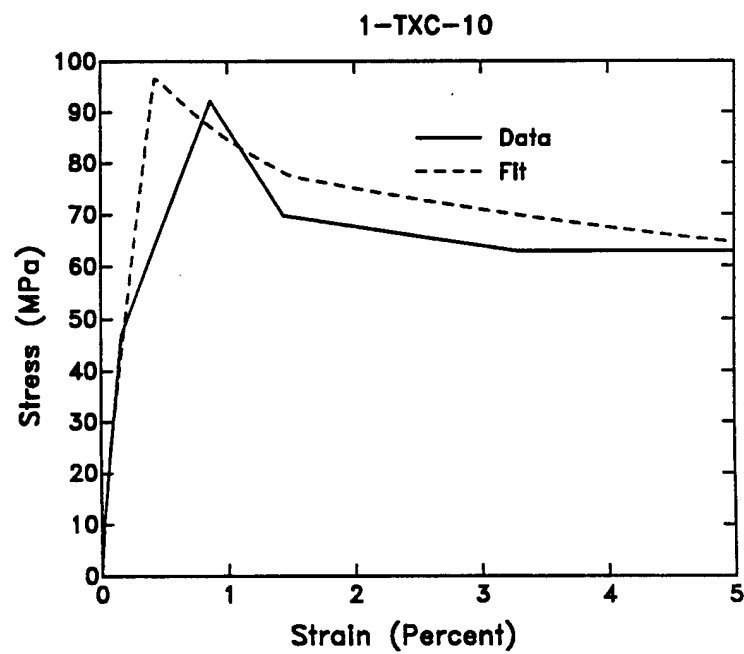
Figure 6.3. Fit of model to TXC data for 10 MPa confining pressure.
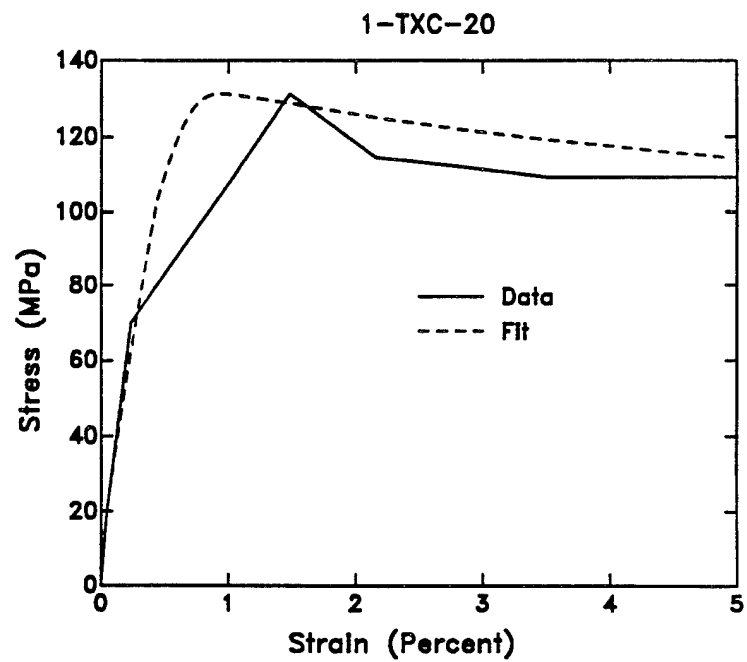
Figure 6.4. Fit of model to TXC data for 20 MPa confining pressure.
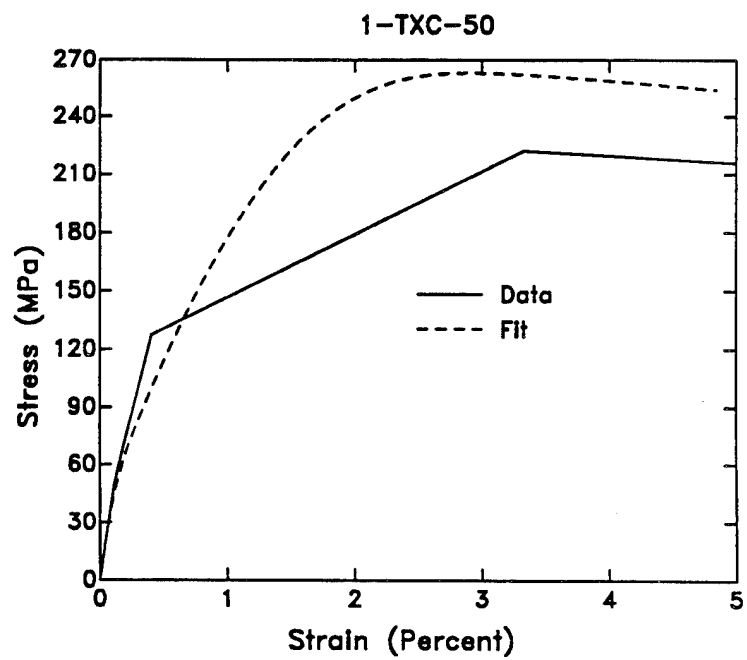
Figure 6.5. Fit of model to TXC data for 50 MPa confining pressure.
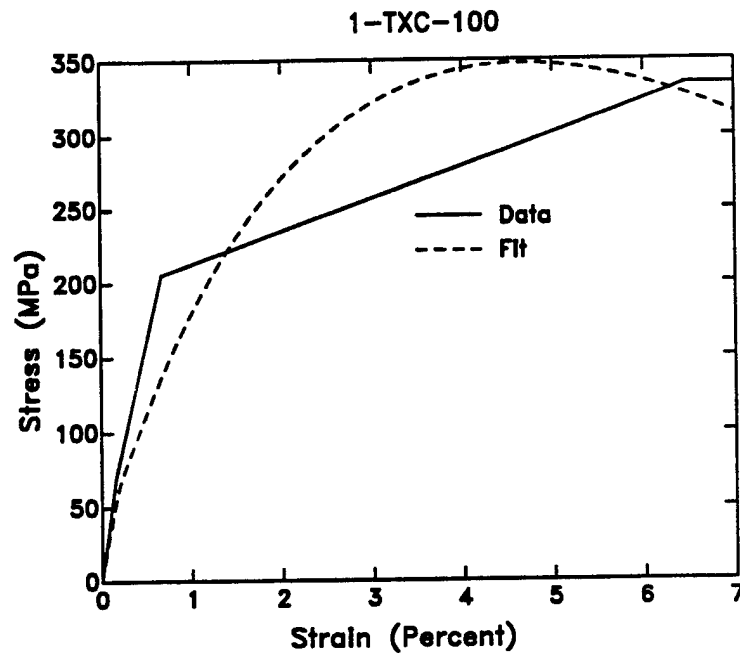
Figure 6.6. Fit of model to TXC data for 100 MPa confining pressure.
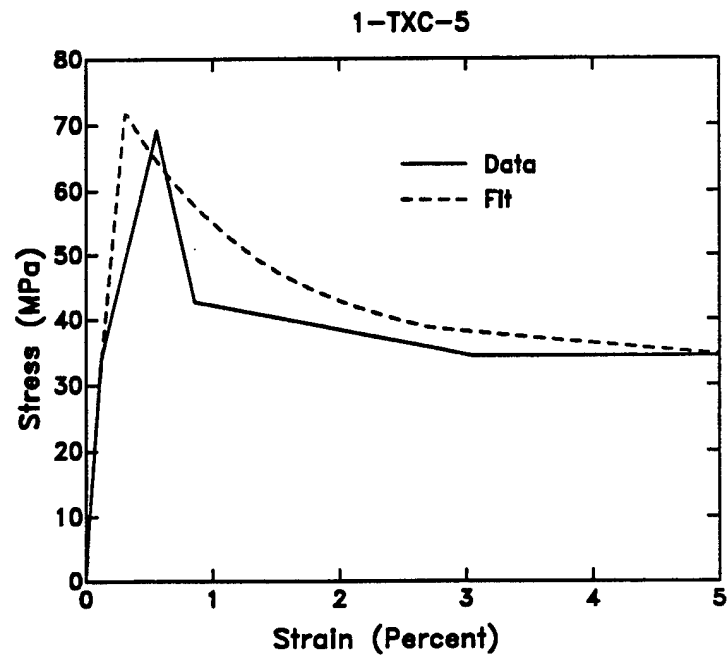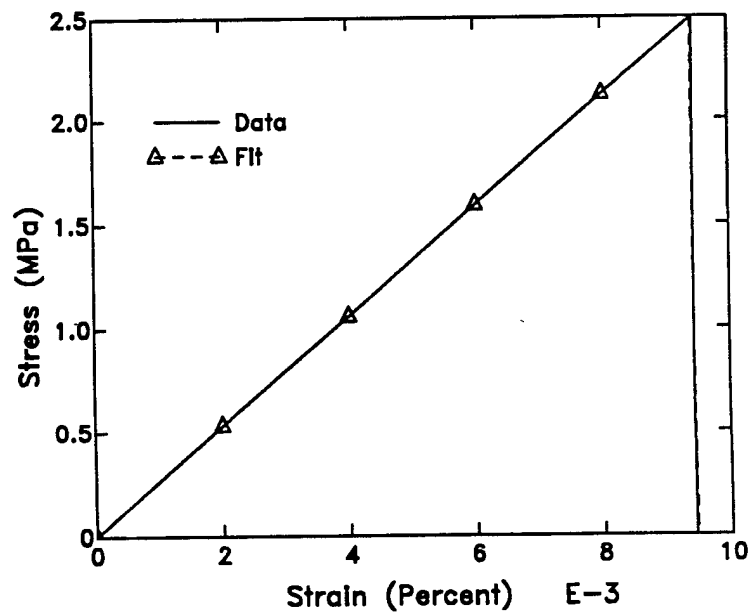

Figure 6.7. Fit of model to TXE data without confining pressure.

RDA provided all calculators with the initial elastic moduli, so the measured and calculated responses are in good agreement during the initial hydrostatic compression and elastic regimes, although differences between the measured and calculated responses are apparent at higher confining pressures. These differences are due to the calculation of plasticity, which initiates at 70 MPa for hydrostatic compression, or slight damage accumulation.

The peak stress of the calculated response is in reasonable agreement with the data for most fits. However, the calculated strain at which the peak stress occurs is less than that of the data, for all fits. The hardening behavior is not adequately modeled. This is probably due to constraints imposed by the dictation of elastic moduli and initiation of plastic response as implied by the piecewise-linear representations of data. Good fits to the hardening behavior of WSMR-5 concrete were obtained in the Round B benchmark calculations.

In fitting the model to the softening behavior of the data, one must keep in mind that the observed softening in TXC laboratory specimens is always accompanied by localization of damage. Test specimens typically split or fail on a diagonal, and the distribution of strain is not uniform throughout the specimen. We were provided with the *average* axial stress-strain response of the specimen, which is different than the stress-strain response in the localized damaged regions and in the undamaged regions. These features of concrete behavior are thoroughly discussed for the Group 2 laboratory test simulations in Section 6.2.

In assigning the benchmark calculations, RDA suggested that the predicted softening in the Group 2 unconfined lab test simulations will be steeper than the Group 1 single element fits. This suggestion was the basis of our Group 1 fit for unconfined compression test, as shown in Figure 6.1. The softening behavior of the single element fit is not nearly as steep as that of the data. However, for confining pressures between 5 and 50 MPa in Figures 6.2-6.5, the softening behavior of the fit is similar to that of the data. For a confining pressure of 100 MPa, the fit softens while the data remains perfectly plastic beyond about 6.3% strain.

One way to check our fit of the damage model to the TXC data is to preform three-dimensional lab test simulations using the model parameters obtained from the single element fit. In this way the average axial stress-strain response from the multi-element lab test simulations can be correlated

46

with the data. One such correlation is made for the unconfined compression test and discussed in Section 6.3.

We also fit the model to data from a TXE test without confinement, as shown in Figure 6.7. The TXE data provided by RDA is a tensile strength of 2.5 MPa with no residual strength after failure. At the time these calculations were performed, a tensile cutoff model was implemented in the concrete damage model. With the tensile cutoff pressure is reached, the damage is instantaneous and complete *i.e.* the damage parameter is set equal to $d = 0.99$.

6.2 MULTI-ELEMENT SIMULATIONS OF TXC TESTS.

The Group 2 calculations are multi-element simulations of an unconfined TXC test. They demonstrate the effect of mesh refinement on the axial stress-strain response, particularly the softening response, and on the localization of damage. These studies use the fit obtained from the Group 1 calculations to model concrete behavior. First, we compare the average axial stress versus strain prediction with the measured data. Next, contours of damage are presented and indicate how damage localizes into diagonal patterns. Finally, local stress versus strain predictions are examined inside and outside the damage zones.

The specimens are modeled 10 cm in the axial z-direction, and 5x5 square cm in the xy plane. The calculation matrix shown in Table 6.1 provides the mesh refinement, the y-face and lateral edge constraints, and whether or not the specimen is 'pinched' to 4.8 cm in the x-direction at midheight. The edge constraints of all pinched specimens are free, which is called 'lubricated' in Table 6.1, while the edge constraints of all unpinched specimens are fixed. For both the pinched and unpinched specimens, the y-faces are either free or in plane strain. In all cases, only one element is modeled in the y-direction. We will refer to this direction as the 'through-the-thickness' direction.

Three mesh refinements are also used in the Group 2 studies, which we will refer to as *coarse* for a 1x1x2 mesh, *medium* for a 1x1x32 mesh, and *fine* for a 16x1x32 mesh. The sample is loaded by a compressive axial velocity which ramps up to 0.0015 m/ms at 0.4 ms and remains constant until the calculation ends at 1.5 ms. The final axial strain is 1.95%. Thus the average strain rate is approximately 13/s, which is much higher than the Group 1 strain rate. These calculations

47

Table 6.1. Matrix of Group 2 laboratory test simulations for Round A.

Case	Zoning xxyxz	Constraint on y-Faces	Lateral Constraint on Ends	Pinching
2-CUL	1x1x2	free	lubricated	yes
2-CUF	1x1x2	free	fixed	no
2-CPL	1x1x2	plane strain	lubricated	yes
2-CPF	1x1x2	plane strain	fixed	no
2-MUL	1x1x32	free	lubricated	yes
2-MUF	1x1x32	free	fixed	no
2-MPL	1x1x32	plane strain	lubricated	yes
2-MPF	1x1x32	plane strain	fixed	no
2-FUL	16x1x32	free	lubricated	yes
2-FUF	16x1x32	free	fixed	no
2-FPL	16x1x32	plane strain	lubricated	yes
2-FPF	16x1x32	plane strain	fixed	no

demonstrate the effect on mesh refinement on the average axial response and on the localization of damage.

Average Axial Stress-Strain Response. The average axial stress-strain response from the coarse, medium, and fine mesh simulations are shown in Figures 6.8-6.10, respectively. Each figure separately shows results for specimens with and without pinching. For the fine mesh calculations, the average stress is calculated by averaging the axial stress for all 16 elements along the loaded edge of the specimen. The average strain is calculated by dividing the axial displacement along the loaded edge by the 10 cm length of the specimen.

Plane strain and unconfined (free) responses are given in each plot and indicate that, in all cases, the peak stress is higher in plane strain than without confinement. This is because the peak stress increases with confinement in TXC tests, so the model provides for increasing strength with confining pressure. The plane strain condition provides some confinement, $i.e$ the through-the-thickness stress is not zero, so the peak stress is enhanced.

The calculated responses of the pinched and unpinched specimens are similar for the medium and
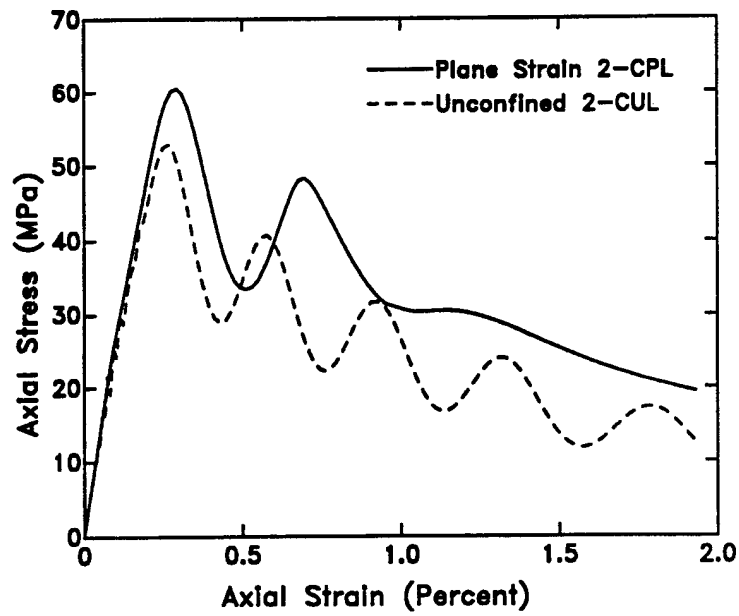
a) Pinched specimens without lateral end constraints.
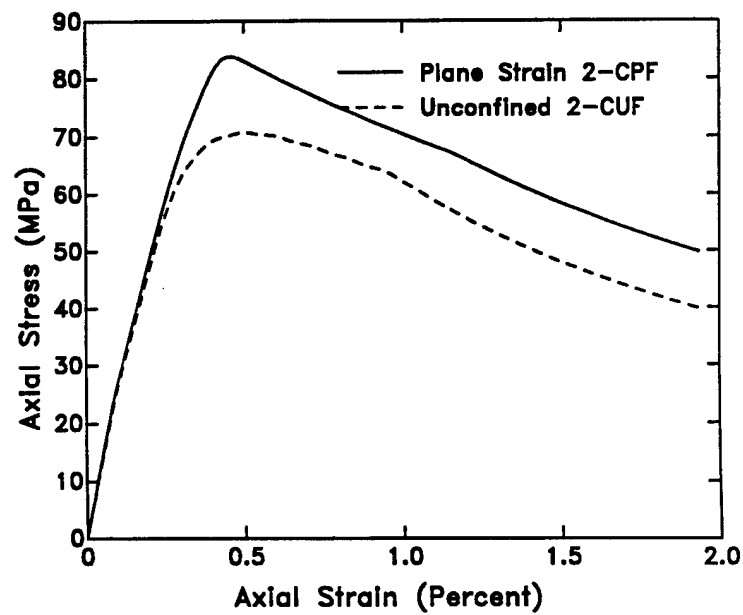
b) Unpinched specimens with lateral end constraints.

Figure 6.8. Coarse mesh computational results.
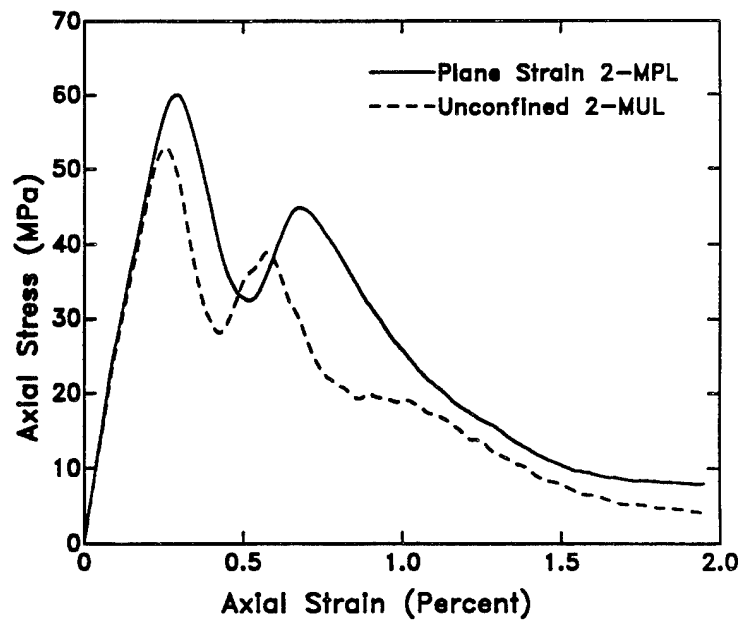
49

a) Pinched specimens without lateral end constraints.

b) Unpinched specimens with lateral end constraints.
Figure 6.9. Medium mesh computational results.
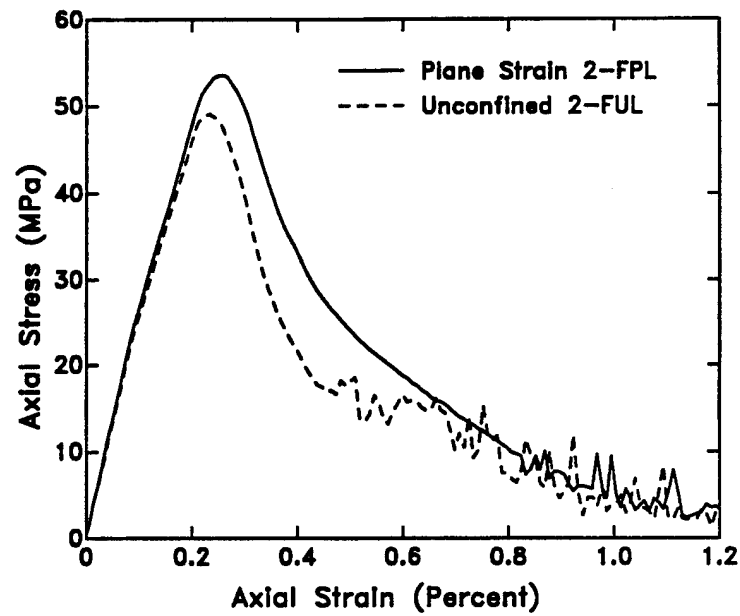
a) Pinched specimens without lateral end constraints.
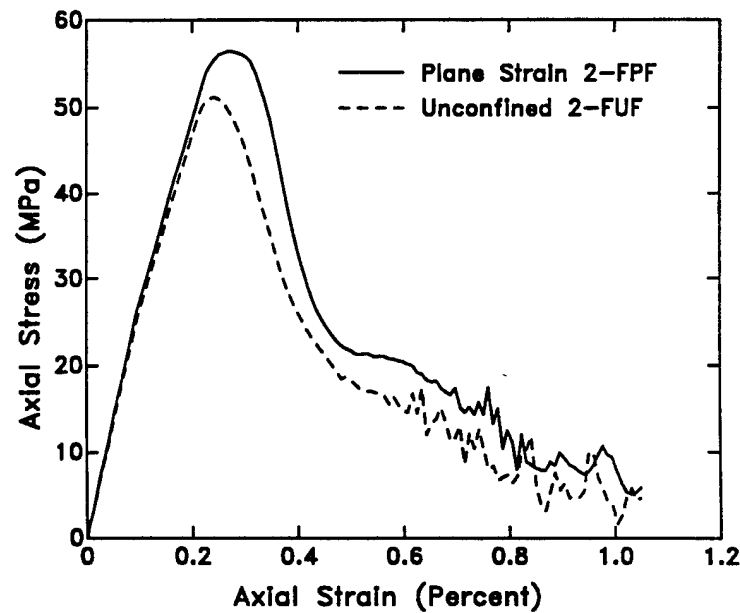
b) Unpinched specimens with lateral end constraints.
Figure 6.10. Fine mesh computational results.

51

fine mesh studies, but not for the coarse mesh studies. For example, the fine mesh results for the pinched specimens in Figure 6.10a are similar to those of the unpinched specimens in Figure 6.10b. However, the coarse mesh results for the pinched specimens in Figure 6.8a are different than those of the unpinched specimens in Figure 6.8b. Two differences are noted: the magnitude of the peak stress and the oscillatory behavior. Both of these differences are due to the lateral edge constraint placed on the unpinched specimens, but not on the pinched specimens.

The magnitude of the peak stress in the coarse mesh studies is discussed first. All nodes except the mid-height nodes are constrained from lateral motion in the unpinched specimens with coarse mesh refinement (2 elements). This lateral edge constraint provides confinement, which increases the peak stress in the unpinched specimens. The peak stress is greater with lateral confinement (unpinched) than without confinement (pinched). The effect of the lateral edge constraint is less significant for the medium and fine mesh refinements, because only two of the 33 nodes along each edge of the mesh are laterally constrained.

Oscillations are also apparent in the pinched specimen, coarse mesh calculations, but not in the unpinched specimen calculations. The oscillations in the coarse mesh, pinched specimen calculations can be eliminated by either reducing the strain rate, or by applying lateral edge constraints. The axial stress oscillations are accompanied by synchronized lateral oscillations in both stress and displacement. Without lateral end constraints, oscillatory lateral stresses develop because the lateral displacements oscillate about their quasi-static values at the Group-2 strain rate. Any overshoot in lateral stress is accompanied by an overshoot in axial stress, similar to the effect of confining pressure on the peak axial stress.

One point to note about the the computed responses is that the steepness of the softening response increases dramatically with mesh refinement. With coarse mesh refinement, the average axial stress is more than half of the peak stress at an axial strain of 1%, in all cases. With fine mesh refinement, the average axial stress is less than 10% of the peak stress at 1% strain, in all cases.
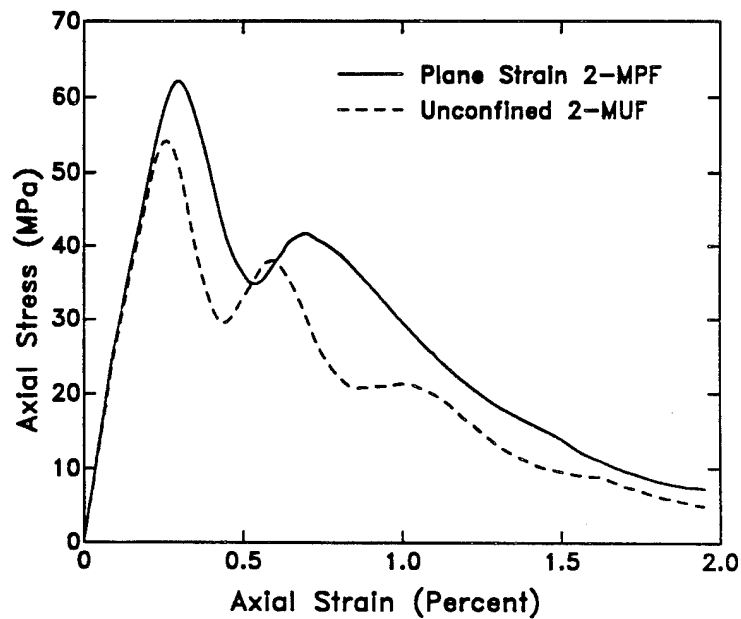
To determine how well we fit the damage model parameters to the data, the average stress-strain prediction from the the unconfined pinched specimen calculation (2-FUL) is compared with the test data and single element fit in Figure 6.11. The softening response of the lab test simulation is
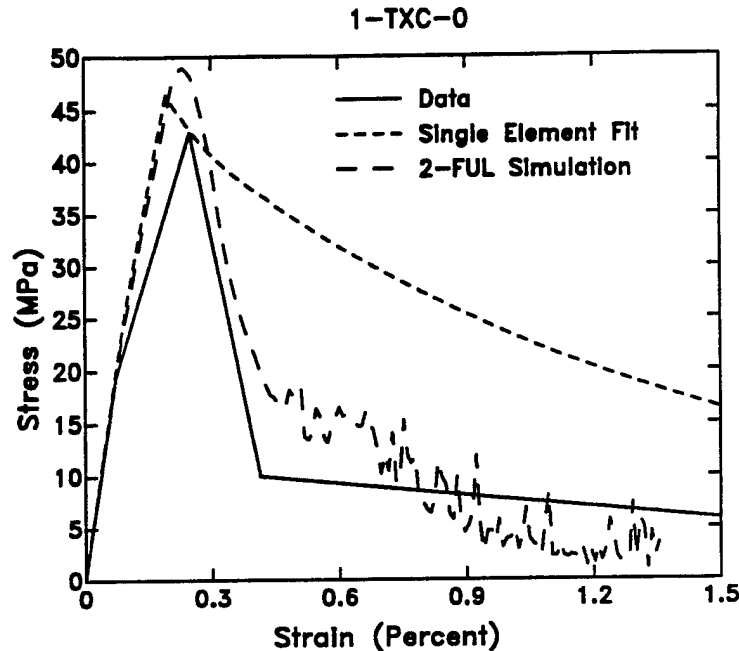
Figure 6.11. Comparison of the fine mesh, unconfined lab test simulation and the single element fit with test data.

much steeper than the single element fit, and in better agreement with the data. *This comparison indicates that a single element cannot be used to fit the softening response measured from a lab test simulation, at least for a rate-independent model.* This is because the post-peak strain distribution is highly non-uniform throughout the specimen, due to localized damage accumulation, and this damage accumulation cannot be captured with a single element model. Damage localization is demonstrated and the effect of further mesh refinement is discussed in subsequent paragraphs.

Another difference between the lab test simulation and single element fit is the peak stress prediction. The higher peak stress calculated with the lab test simulation is probably due to dynamic overshoot due to the high strain rate. The lab test simulation was run at a dynamic strain rate of 13/s whereas the single element fit was run at a much slower strain rate of 0.001/s.

Contours of Damage. Contours of the damage parameter d are plotted in Figures 6.12-6.15 for the fine mesh calculations. The time of each plot is after substantial post-peak softening has occurred. A value of $d = 0.99$ indicates that maximum damage has occurred and the moduli have been reduced to 1% of their original elastic values. A value of $d = 0$ indicates that no damage has occurred.

53

FUL 2
time = 0.59988E+00
contours of eff. plastic strain
min= 0.118E+00 in element 512
max= 0.990E+00 in element 409

contour values
A= 2.30E-01
B= 3.60E-01
C= 4.89E-01
D= 6.19E-01
E= 7.48E-01
F= 8.78E-01
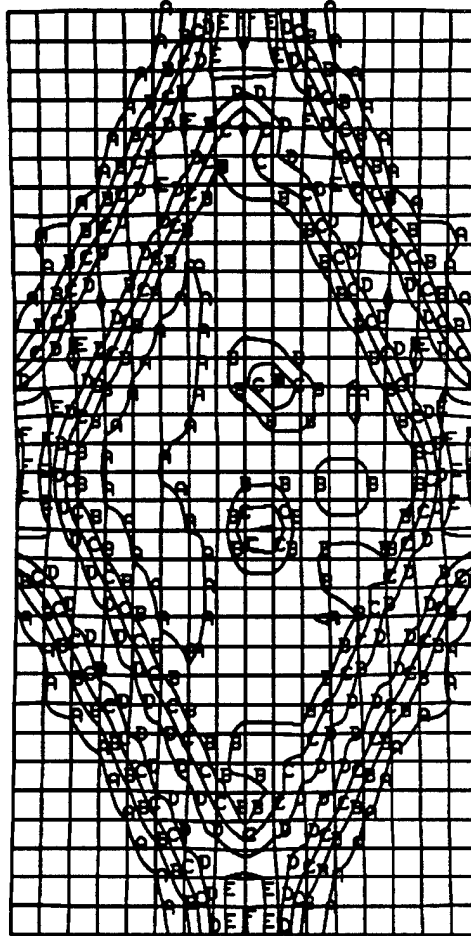
disp. scale factor = 0.100E+01 (default)

Figure 6.12. Contours of damage for an unconfined specimen pinched at midheight (2-FUL).

FPL 2
 time = 0.59939E+00
contours of eff. plastic strain
min= 0.125E+00 in element   16
max= 0.923E+00 in element   9

contour values
 A= 2.27E-01
 B= 3.46E-01
 C= 4.65E-01
 D= 5.83E-01
 E= 7.01E-01
 F= 8.20E-01
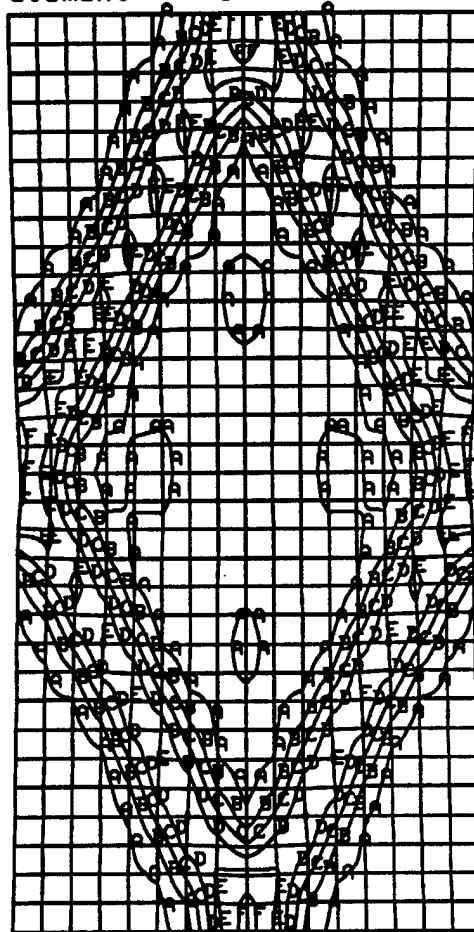
disp. scale factor =   0.100E+01 (default)

Figure 6.13. Contours of damage for a plane strain specimen pinched at midheight (2-FPL).

55

```
2-FUF MODEL FOR GROUP 2 BENCHM
  time =  0.60000E+00                                   contour value
                                                          A= 2.00E-01
contours of eff. plastic strain                           B= 2.90E-01
                                                          C= 3.80E-01
min= 1.278E-01 in element      4                          D= 4.69E-01
max= 9.900E-01 in element    505                          E= 5.59E-01
                                                          F= 6.49E-01
                                                          G= 7.38E-01
                                                          H= 8.28E-01
                                                          I= 9.18E-01
```

z
↑
└──→ x
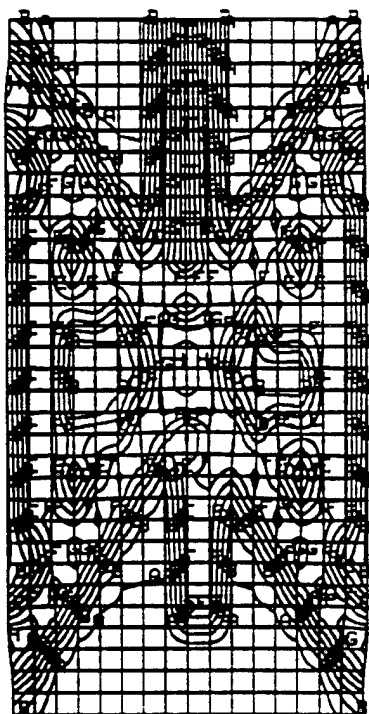
disp. scale factor = 0.100E+01 (default)

Figure 6.14. Contours of damage for an unconfined specimen with fixed lateral edge constraints (2-FUF).

```
2-FPF MODEL FOR GROUP 2 BENCHM
  time =  0.60000E+00
contours of eff. plastic strain
min= 1.363E-01 in element      6
max= 9.900E-01 in element    383
```

```
contour value
  A= 2.08E-01
  B= 2.97E-01
  C= 3.86E-01
  D= 4.74E-01
  E= 5.63E-01
  F= 6.52E-01
  G= 7.41E-01
  H= 8.30E-01
  I= 9.18E-01
```
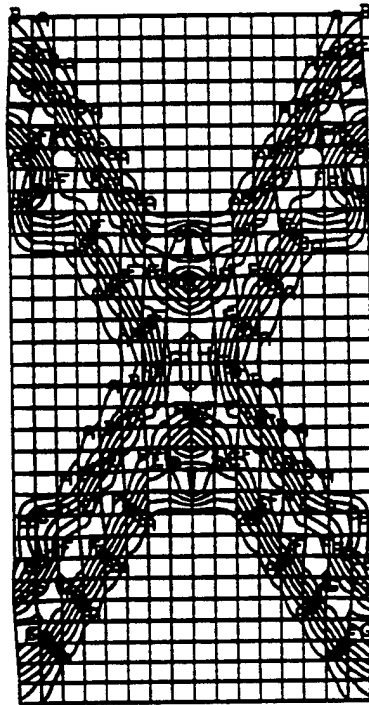
```
disp. scale factor =  0.100E+01 (default)
```

Figure 6.15. Contours of damage for a plane strain specimen with fixed lateral edge constraints (2-FPF).
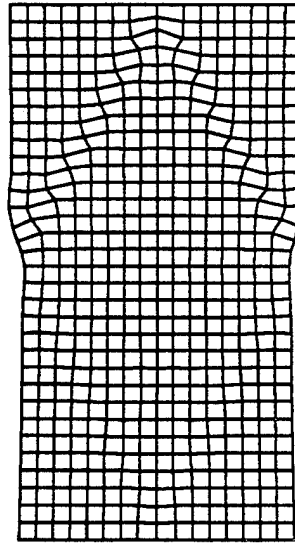
Figure 6.16. The deformed configuration of a plane strain specimen pinched at mid-height (2-FPL).

The damage pattern for the pinched specimen is a diamond pattern. Damage initiates at the mid-height pinch on each side, and at center on the loaded and unloaded ends. The damage pattern for the unpinched specimens with lateral end constraints is an 'X' pattern. Damage initiates at the four laterally constrained corners of the specimen.

The damage pattern can also be detected from the deformed configuration of each mesh, although less readily than from the contour plots. The deformed configuration for the pinched specimen without confinement is shown in Figure 6.16. Half of the diamond pattern is clearly visible on the loaded end of the specimen. Here some elements have distorted, probably because their moduli have been reduced to 1% of their original values. A *viscous* method for hourglass stabilization method was used in these analyses. We switched to a *stiffness* method in Round B, which reduces some of the observed distortion.

Local Stress-Strain Responses. Here we examine stress and strain histories at specific locations inside and outside the damage zones. Four sets of stress and strain histories are plotted in Figure 6.17 for the plane strain specimen pinched at mid-height (2-FPL). Three of these locations are at the corner points of the diamond pattern region of severe damage, labeled top center, side pinch, and
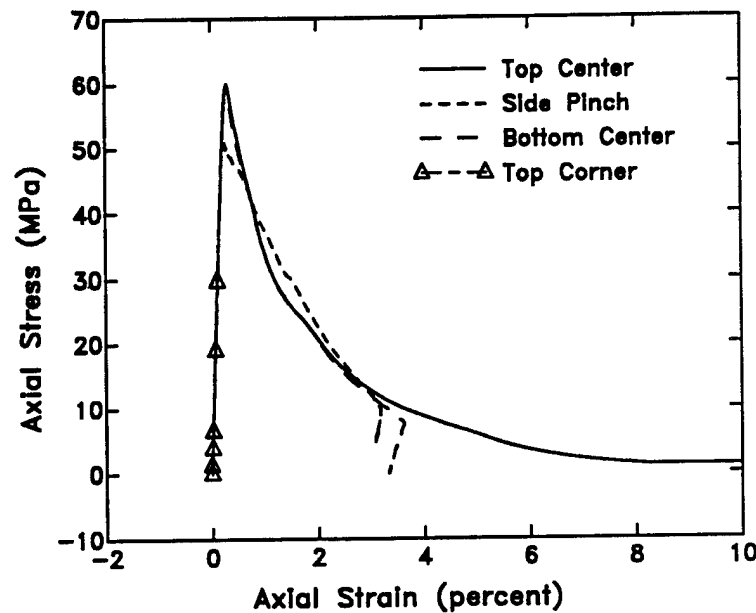
Figure 6.18. Stress-strain responses at four different locations (2-FPL).

bottom center. The top is the loaded edge of the mesh, and the bottom is the unloaded edge. The fourth location is the top corner, or loaded edge corner.

The stress histories at all four locations are similar, indicating that the distribution of axial stress is fairly uniform throughout the specimen, even while damage accumulates. The strain histories are similar up to a time of about 0.35 msec, just prior to the time of peak stress, but then they diverge. Axial strains as large as 13% (center) and less than 0.1% (corner) occur on the loaded edge of the specimen. Thus the post-peak distribution of strain is highly non-uniform, and this affects the local stress-strain responses.

Stress-strain curves are plotted in Figure 6.18 at the same four locations. The stress-strain curve at top center reaches a peak and then continuously softens as the strain increases. The stress-strain curves at the side pinch and bottom center also soften following the peak stress, but then they unload elastically at about 3% strain. The stress-strain curve outside the severe damage region (top corner) loads to a peak stress of about 50 MPa and then unloads elastically. This comparison demonstrates how different stress-strain behaviors are predicted at various locations within the specimen.

59
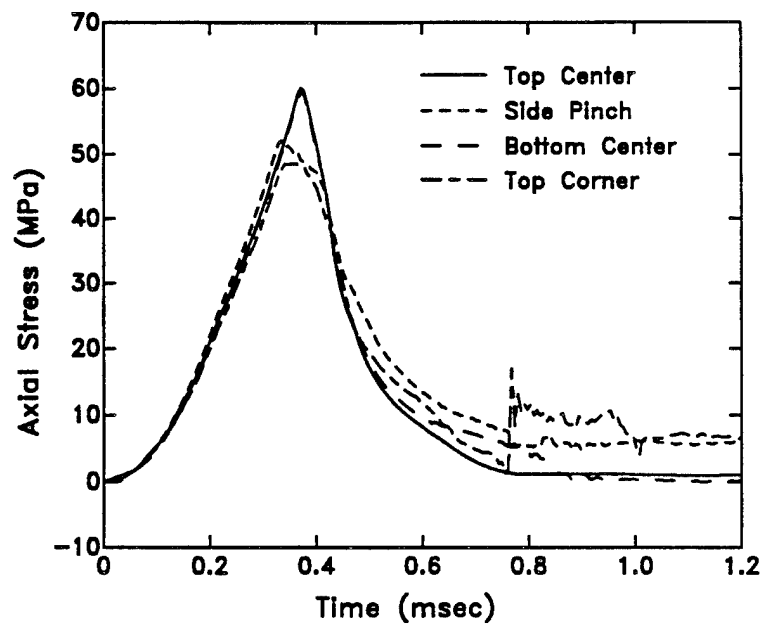
a) Stress histories.
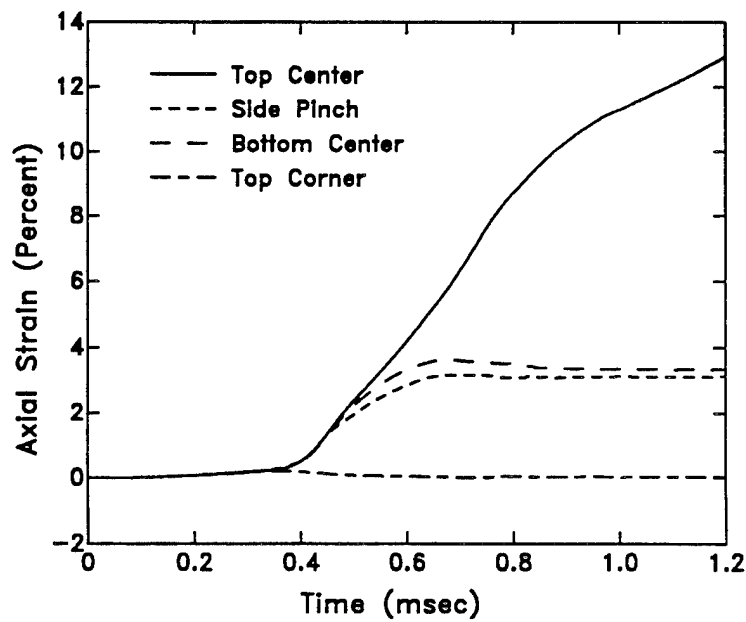
b) Strain histories.

Figure 6.17. Stress and strain histories calculated at four different locations (2-FPL).
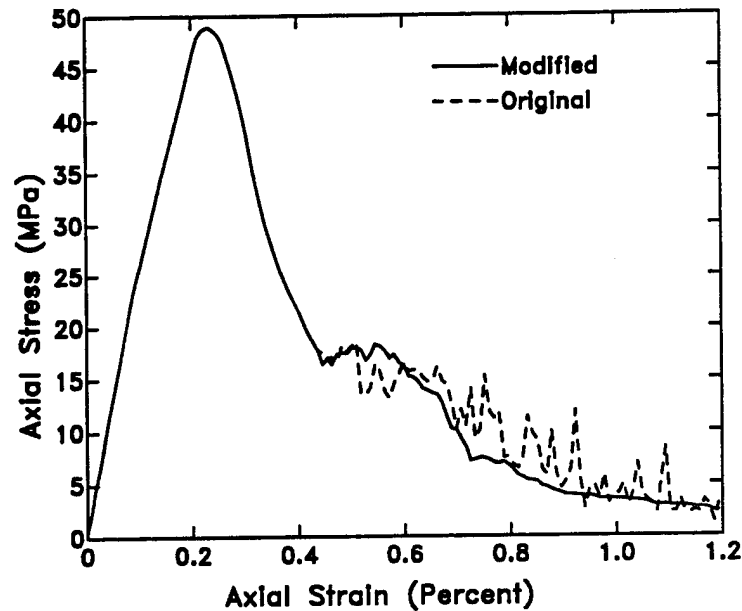
Figure 6.19. Average axial response calculated with two different tensile cutoff behaviors (2-FUL).

Effect of Tensile Cutoff Model on Calculated Response. The average axial stress-strain curves for the fine mesh calculations in Figure 6.10 exhibit high frequency oscillations after substantial softening has occurred. This high frequency behavior occurs when the tensile cutoff is reached. We implemented the cutoff behavior to instantaneously calculate maximum damage ($d = 0.99$) when the stress state reaches the tensile cutoff. However, we allowed the damage parameter to revert to its previous value if the stress state subsequently moves off of the cutoff surface. This resulted in abrupt fluxuation of the damage parameter which caused the high frequency behavior.

We ran an additional calculation in which maximum damage ($d = 0.99$) was sustained for the remainder of the calculation once the stress state reached the tensile cutoff. We will refer to this implementation as the modified tensile cutoff behavior. Average axial stress-strain histories calculated with the original and modified cutoff behaviors are compared in Figure 6.19 for the unconfined, pinched cylinder. Note that most of the high frequency behavior is eliminated in the calculation with the modified tensile cutoff, otherwise the stress-strain curves are nearly identical.

Contours of damage from the modified tensile cutoff calculation are given in Figure 6.20 for comparison with those from the original calculation previously shown in Figure 6.12. Although a diamond

61

DAM 2
time = 0.59949E+00
contours of eff. plastic strain
min= 0.118E+00 in element   512
max= 0.990E+00 in element   511

contour values
A= 2.30E-01
B= 3.60E-01
C= 4.89E-01
D= 6.19E-01
E= 7.48E-01
F= 8.78E-01
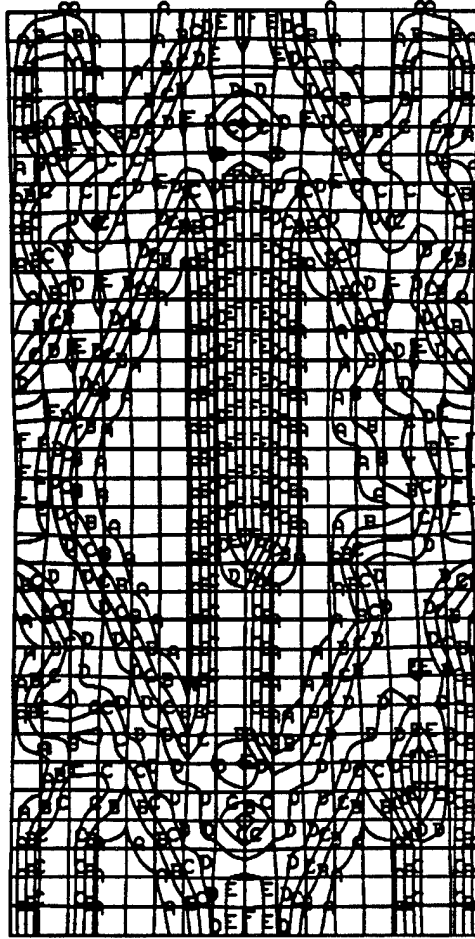
disp. scale factor = 0.100E+01 (default)
Figure 6.20. Contours of damage calculated with the modified tensile cutoff model (2-FUL).

pattern of damage is calculated with both the original and modified tensile cutoff behaviors, an axial fracture down the center of the specimen is also predicted with the modified behavior.

6.3 EFFECT OF MESH REFINEMENT ON THE CALCULATED RESPONSE.

Adding Through-the-Thickness Elements. We performed a three-dimensional lab test simulation to determine how well our single element fit predicts the average axial stress-strain response
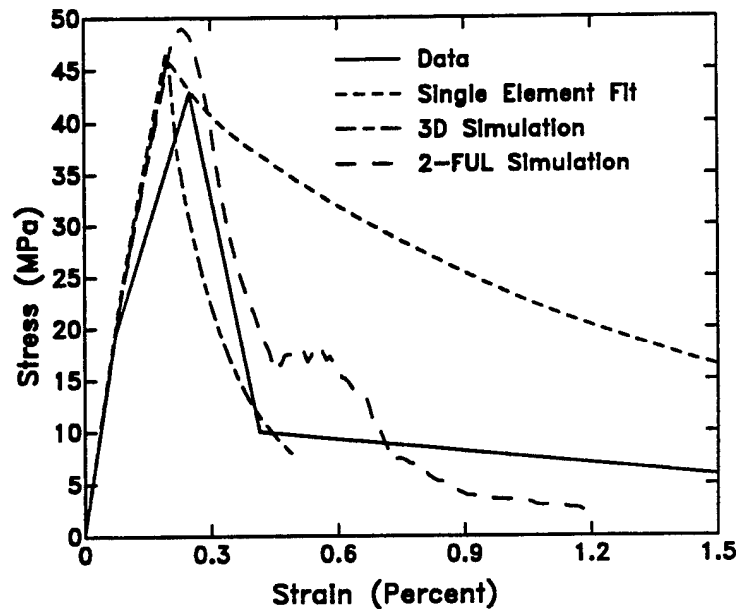
Figure 6.21. Effect of through-the-thickness refinement on the average axial stress-strain response of an unconfined specimen pinched at midheight.

of a lab test specimen in unconfined compression. This calculation is different than the Group 2 simulations in two respects. First, the calculation was run at a slow strain rate of 0.01/s to eliminate dynamic effects. This allows us to more readily compare the lab test simulation with the single element fit because both calculations are run at very low strain rates. Second, elements are modeled through-the-thickness of the specimen, so the resulting mesh is three-dimensional and should be a better simulation of an actual test than the Group 2 models with one element through-the-thickness. The drawback of adding elements through-the-thickness is that the computer run-time is increased.

The average axial stress-strain response is shown in Figure 6.21 for a pinched specimen 18 elements high and 9x9 elements over the square cross section. This calculation is referred to as the '3D simulation'. The average stress is obtained by averaging the axial stress of the 81 elements across the loaded edge of the specimen. Note that the peak stress and pre-peak response calculated with the 3D mesh are nearly equal to that of the single element fit. However, the post-peak softening response of the two calculations differs dramatically. The softening response of the 3D calculation is in good agreement with the data, whereas the softening response of the single element fit is much

63

less steep than that of the data. These comparison suggest that a rate-independent fit based on a single element model will not adequately capture the softening response of a lab test specimen.

Also shown in Figure 6.21 is the Group 2 simulation with one element modeled through-the-thickness. The width of the stress-strain pulse for the 3D simulation is less than that for the Group 2 simulation, and in better agreement with the data. This may be because through-the-thickness elements were modeled, or because the strain rate was reduced in the 3D simulation.

Contours of damage on each face of the 3D mesh are shown in Figure 6.22 at a time when substantial softening has occurred and the average axial strain is 0.32%. Note that although the contours indicate a diagonal damage pattern, the pattern is not a diamond pattern, nor is it symmetric about the axial midplane of each face. The reason for the lack of symmetry is not known, although it may be do to sensitivity of the damage and tensile cutoff portions of the model to numerical roundoff.

Refining the Group 2 Fine Mesh. To assess the effect of mesh refinement on the fine mesh predictions, an additional calculation for simulation FUL-2 was performed by doubling the number of elements in each coordinate direction. The resulting mesh is 64 elements high and 32x2 elements over the cross section. Stress-strain results for the original 16x1x32 mesh, and the refined 32x2x64 mesh are compared in Figure 6.23 and demonstrate that the pre-peak and post-peak responses are nearly identical until the concrete softens to about 60% of its peak stress.

Contours of damage from the refined mesh calculation are shown in Figure 6.24 for comparison with those from simulation FUL-2 and previously shown in Figure 6.12. Again, a diamond pattern of damage is predicted, although two possible fracture lines are calculated with the refined mesh while one possible fracture line is calculated with the original mesh. However, the width of the damage bands calculated with the refined mesh is approximately equal to that of the original mesh.

contour values
A: 2.33E-01
B: 3.62E-01
C: 4.91E-01
D: 6.20E-01
E: 7.49E-01
F: 8.78E-01
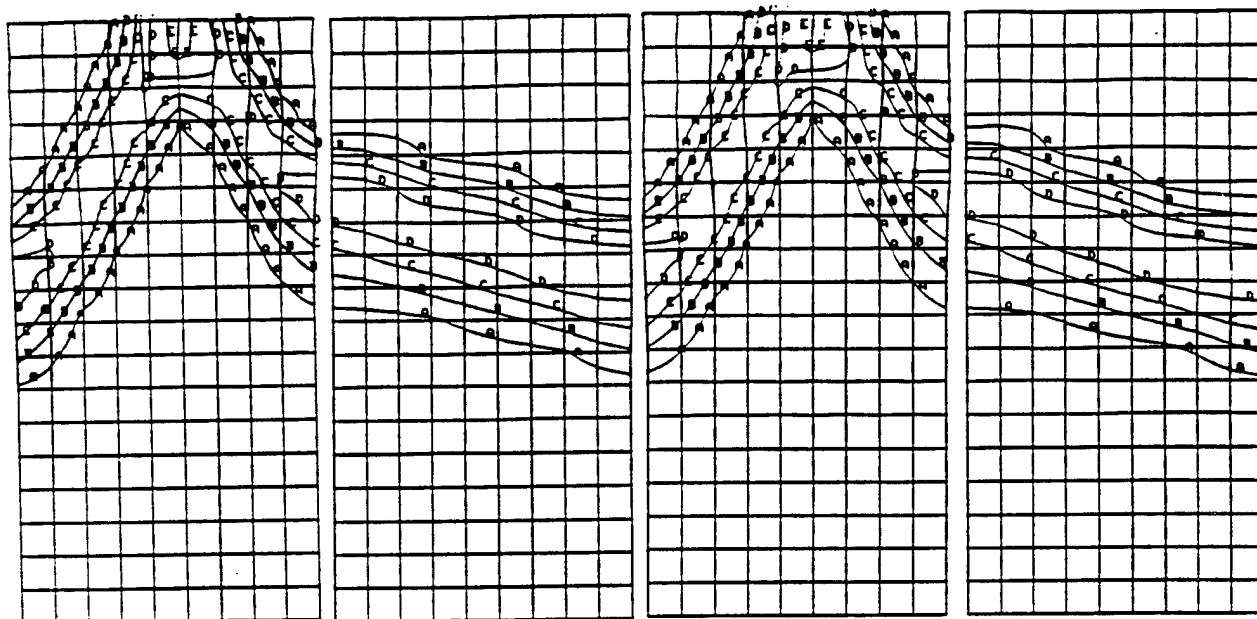
Figure 6.22. Contours of damage on each face of the 3D simulation.
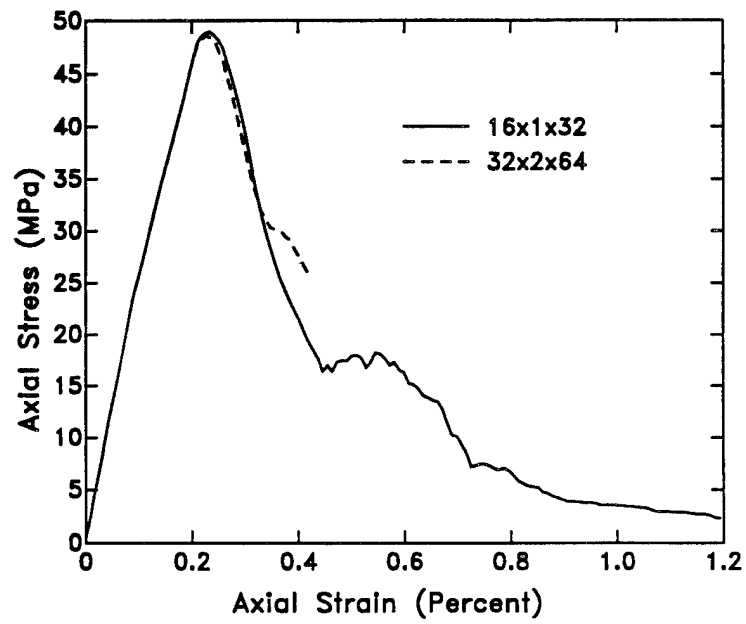
Figure 6.23. Effect of mesh refinement on the average axial stress-strain response of an unconfined specimen pinched at midheight (2-FUL).

FUL 2 32X64X2
  time = 0.47965E+00
contours of eff. plastic strain
min= 0.173E+00 in element 4002
max= 0.990E+00 in element 4064
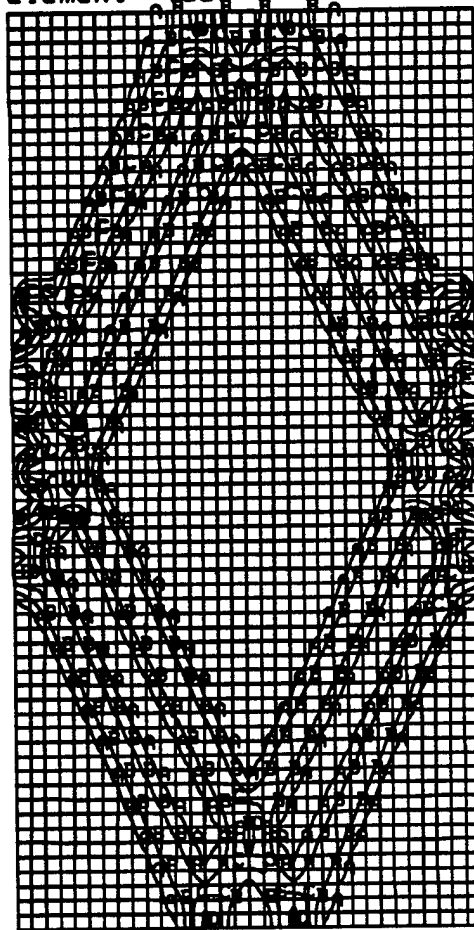
disp. scale factor = 0.100E+01 (default)

Figure 6.24. Contours of damage for a refined mesh simulation of specimen 2-FUL.

SECTION 7

ROUND B BENCHMARKS: FITS TO WSMR-5 DATA

The Round B calculations are similar to the Round A calculations except that RDA provided the calculators with WSMR-5 data curves measured by WES. The Round B calculations consists of Group 1 single element fits and Group 2 multi-element simulations. However, the Round B calculations are run at a slower strain rate than the Round A calculations to eliminate the undesirable oscillatory behavior observed in the Round A simulations. The Round B calculations also model rate dependence of the strength using the Duvaut-Lions viscoplastic update algorithm previously discussed in Section 2.4.4.

7.1   SINGLE ELEMENT FITS TO WSMR-5 DATA.

Single element fits of the model to WSMR-5 data are given in Figures 7.1 through 7.5. The calculations were run at a strain rate of 0.001/s to eliminate inertial effects, and rate dependence of the strength was neglected. We used the isotropic damage model previously described in Section 2.1. We fit the data without considering damage first, then *iteratively* adjusted the fits to include damage, as discussed in Appendix D. Table 7.1 provides the material model parameters used in these fits.

We obtained excellent fits of the model to the isotropic compression and uniaxial strain data. We also modeled less softening than measured from the TXC tests. This is because we expected more softening to be predicted in the Group 2 TXC simulations than modeled with the single element fits. The direct pull test data was fit to the tensile pressure cutoff model previously described for the Round A benchmarks.

A three-dimensional calculation was performed to asses the effect of mesh refinement on the calculated response. This calculation was not part of the required benchmark series. The three-dimensional simulation was performed with a 16x16x32 mesh for comparison with the single element fit, as shown in Figure 7.6. Rate dependence of the strength was ignored. The softening response

Table 7.1. Model parameters for the fit with damage.

Constitutive Model

K (MPa)	24100
G (MPa)	16000
ρ (gm/cm^3)	2.30

Failure Envelope

$$F_e(J_1) = \alpha - \gamma e^{-\beta J_1} + \theta J_1$$

α (MPa)	328
θ	0.03
λ (MPa)	317
β (MPa^{-1})	0.00148

Moveable Cap

$$F_c(J_1, \kappa) = 1 - \frac{(J_1 - L)(|J_1 - L| + J_1 - L)}{2(X - L)^2}$$

$$X(\kappa) = L + RF_e(L)$$

$$L(\kappa) = max(\kappa_0, \kappa)$$

R	5
X_0 (MPa)	0

Cap Hardening Rule

$$\epsilon_v^p = W\{1 - e^{-D[X - X_0] - D_2[X - X_0]^2}\}$$

W	0.05
D (MPa^{-1})	1.8×10^{-4}
D_2 (MPa^{-2})	2.4×10^{-7}

Third Invariant

$Q_1 =$ TOR/TXC $Q_2 =$ TXE/TXC

α_1	0.705
α_2	0.686

Pressure Cutoff

T (MPa)	-3.9

Damage Model

$$d = 1 - \frac{r_o(1 - A)}{\tau} - Ae^{B(r_o - \tau)}$$

r_0	0.4
A	0.7
B	0.01
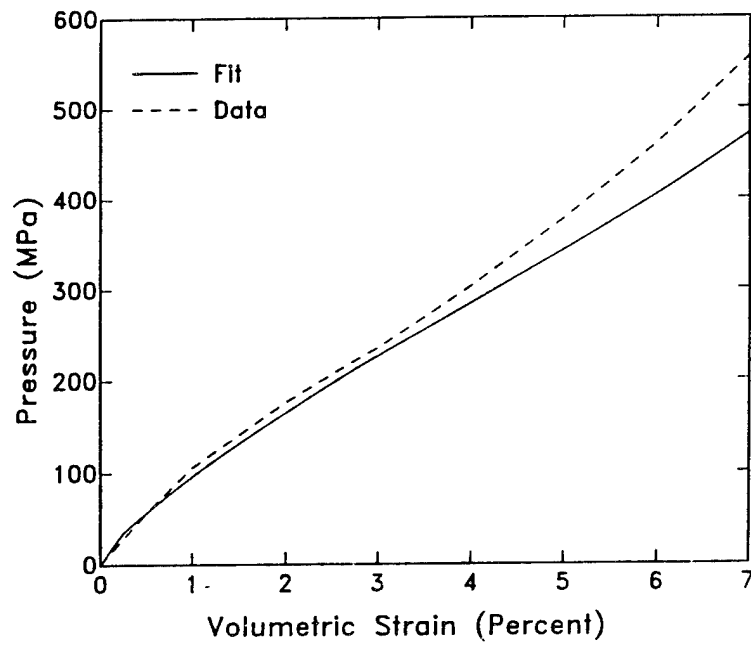
Figure 7.1. Fit of the model to isotropic compression data.
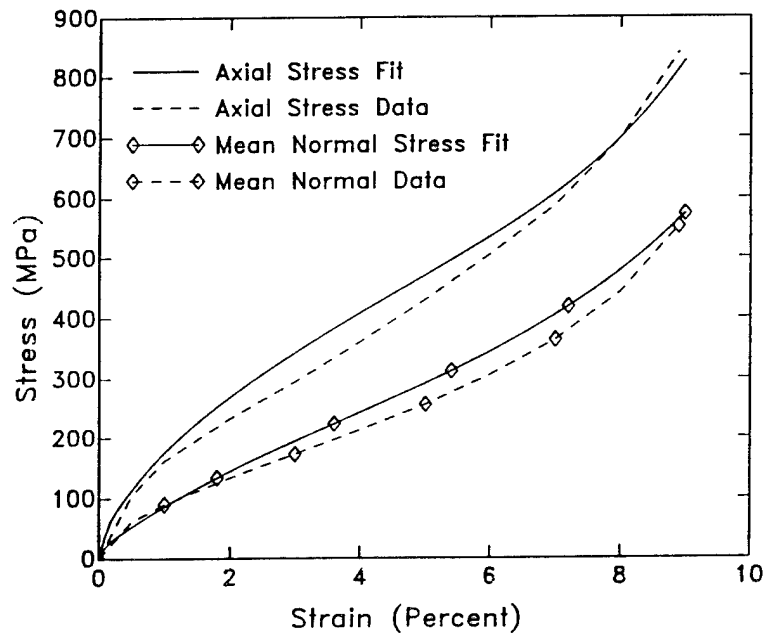
Figure 7.2. Fit of the model to uniaxial strain data.

70
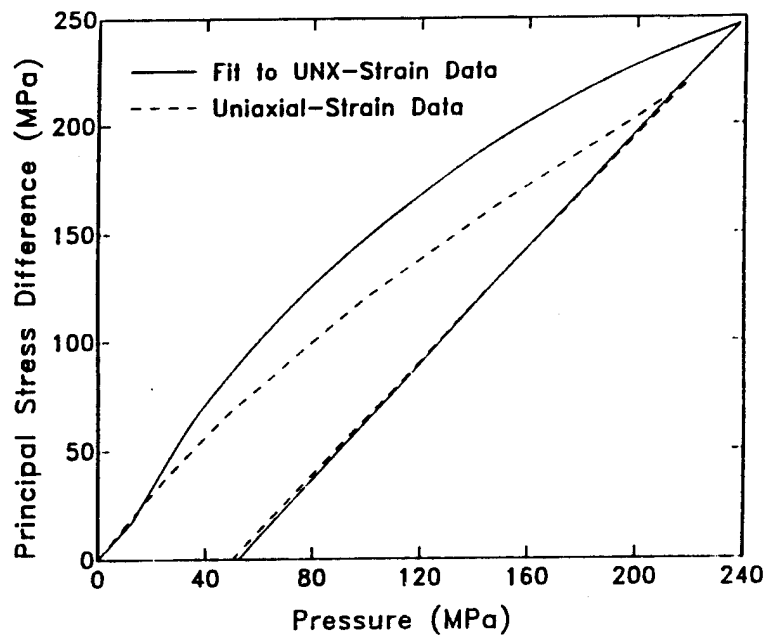
Figure 7.3. Fit of the model to principal stress versus pressure data for a uniaxial strain test.

of the three-dimensional simulation degrades more rapidly than the single element fit, although the degradation is not as rapid as we would have liked to have modeled[1]. Although no data is available on the softening response of WSMR-5 concrete from the unconfined compression tests, WES's *recommended* curve softens to zero strength at about 0.5% strain. These comparisons suggest that more damage should be modeled in our fit to the WSMR-5 data. They also suggest that the softening response is more sensitive to the mesh refinement when more damage is modeled.

7.2 MULTI-ELEMENT SIMULATIONS OF TXC TESTS.

The calculation matrix in Table 7.2 provides the mesh refinement and y-face constraints for the Round B Group 2 calculations. Only the lubricated end (free) cases from Round A were re-calculated in Round B. The Round B multi-element simulations were run at an average strain rate of $\dot{\epsilon} = 1.3$, which is a factor of ten slower than the Round A multi-element simulations. The slower strain rate eliminates undesirable oscillations. The Round B simulations were also performed with strength enhancement as a function of strain rate. The strength enhancement factor previously given in Equation 2.44 was provided by RDA to all benchmark participants.

---

[1]Time constraints prevented us from re-adjusting our fits and performing additional simulations.

COMPARISON OF TXC SHEAR RESPONSE AT CONFINING PRESSURES WITHIN
THE BRITTLE REGION FOR WSMR-5 3/4 INCH CONCRETE
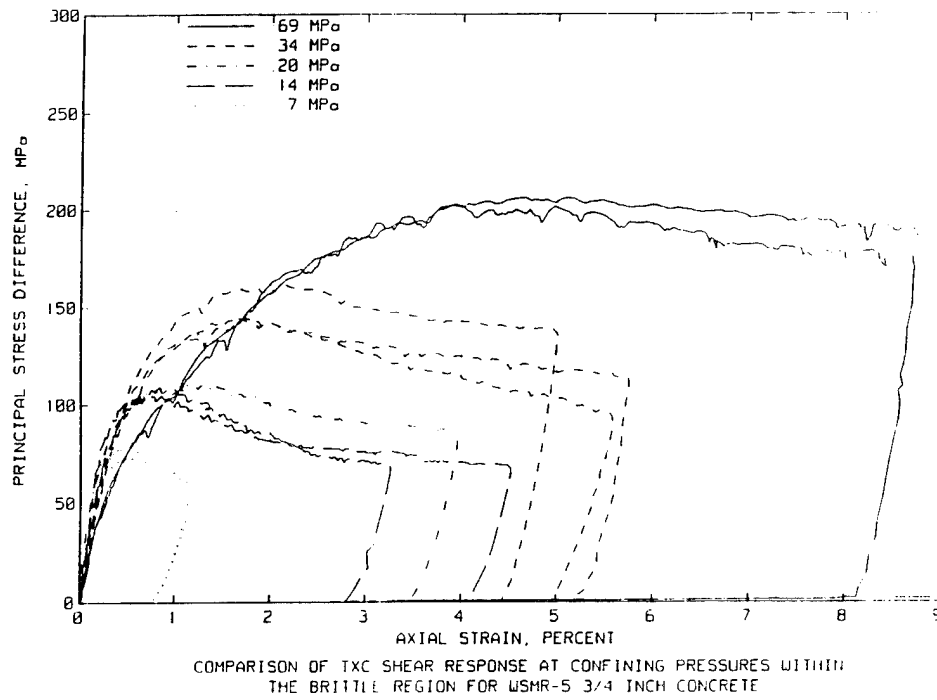
(a) WSMR-5 concrete data.
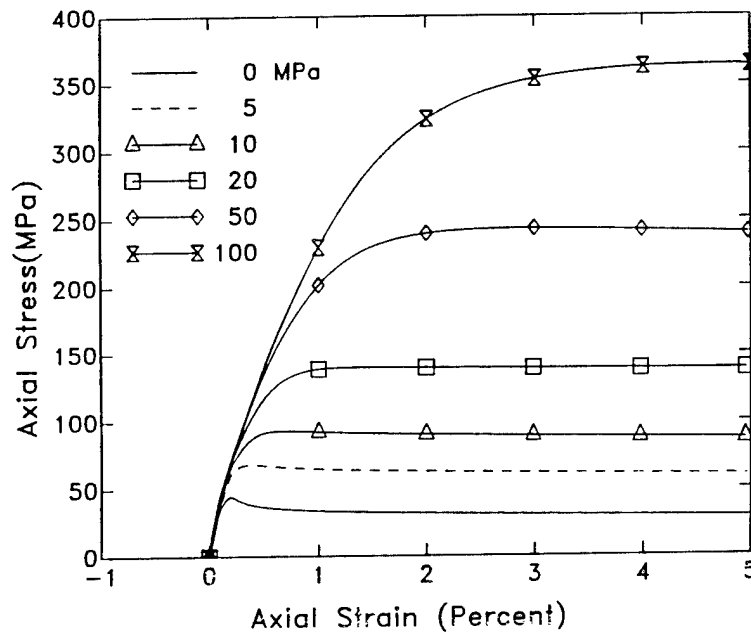
(b) Single element fits.

Figure 7.4. Fit of the model to TXC test data for confining pressures between 0 and 100 MPa.
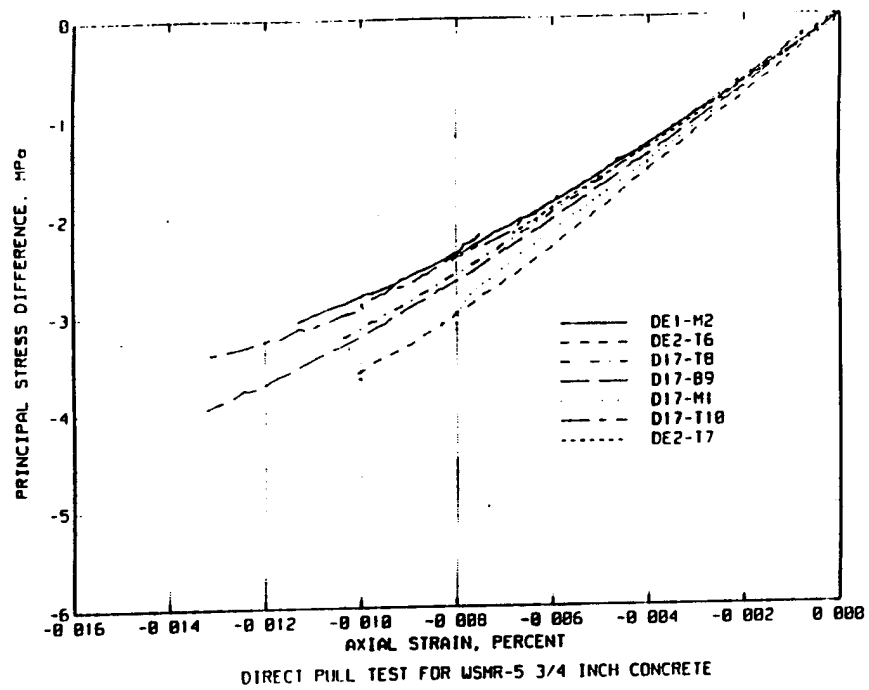
(a) WSMR-5 concrete data.
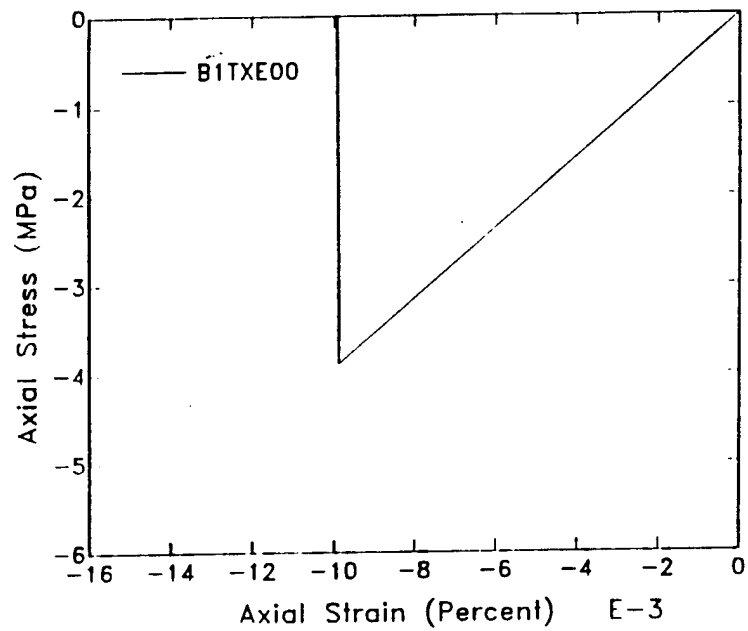
(b) Single element fit.

Figure 7.5. Fit of the model to direct pull test data.

73
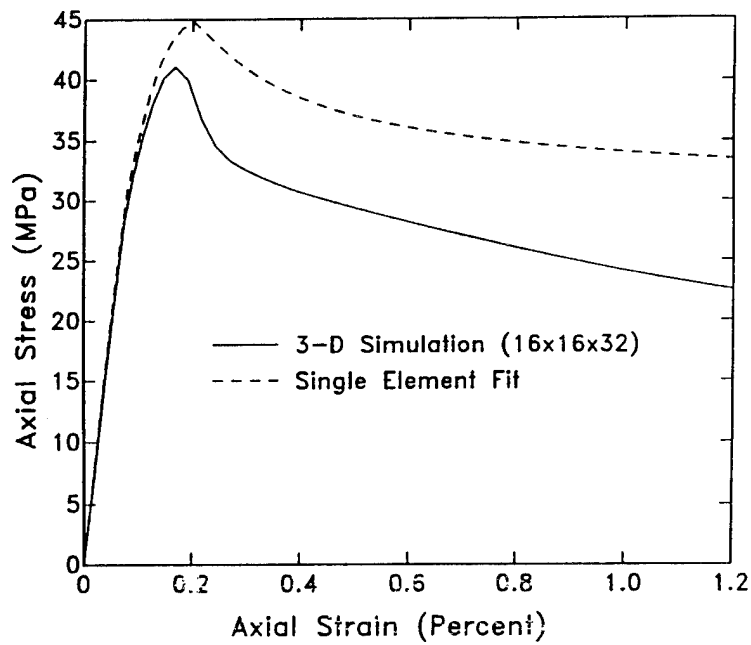
Figure 7.6. Comparison of three-dimensional simulation with the single element fit (Round B).

Table 7.2. Matrix of Group 2 laboratory test simulations for Round B.

Case	Zoning xxyxz	Constraint on y-Faces	Lateral Constraint on Ends	Pinching
B2-CUL	1x1x2	free	lubricated	yes
B2-CPL	1x1x2	plane strain	lubricated	yes
B2-MUL	1x1x32	free	lubricated	yes
B2-MPL	1x1x32	plane strain	lubricated	yes
B2-FUL	16x1x32	free	lubricated	yes
B2-FPL	16x1x32	plane strain	lubricated	yes

The average axial stress-strain responses from the coarse, medium, and fine mesh simulations are compared in Figure 7.7a for plane strain and in Figure 7.7a for unconfined compression. The peak stresses attained with the coarse, medium, and fine mesh simulations are in close, but not identical agreement. As expected from Round A, the peak stress attained in the plane strain simulations is greater than the peak stress attained from the unconfined compression simulations. The value of the peak stress attained in all simulations is greater than the static value of 45 MPa because rate dependence of the strength was modeled.

Unlike the Round A simulations, the steepness of the softening response for the Round B simulations does not increase dramatically with mesh refinement. Only small increases in softening response are calculated with increased mesh refinement, at least for plane strain response. This is because we modeled less damage in the Round B simulations than in the Round A simulations. This demonstrates that the effect of mesh refinement on the softening response is less severe when less damage is modeled.

RDA compiled all participants Round B benchmark calculations in Reference 9. APTEK's original B2-FUL simulation reported to RDA exhibits a sudden drop in stress. This instability (sudden stress drop) is associated with the type of hourglass control we used. The sudden stress drop is due to instability of the rectangular mesh caused by hourglassing[2] in elements with aspect ratios of 16. Such a high aspect ratio is outside the usual range of 2 or less.

Two types of hourglass stability methods are available in DYNA3D, called viscous and stiffness methods. The default form in DYNA3D is a viscous form. The effect of the hourglass stability method on simulation B2-FUL is shown in Figure 7.8. Note that a sudden drop in stress occurs when using the viscous form for hourglass stability, but not when using the stiffness form. Our original (unstable) B2-FUL simulation reported to RDA in Reference 9 was preformed with the viscous method whereas the stable response was preformed with the stiffness method. All other Round A and B calculations were performed with the viscous method.

---

[2]Hourglass deformation modes are spurious zero energy modes that arise from elements formulated with one-point Gauss quadrature. The spurious deformation modes must be stabilized while retaining legitimate deformation modes.
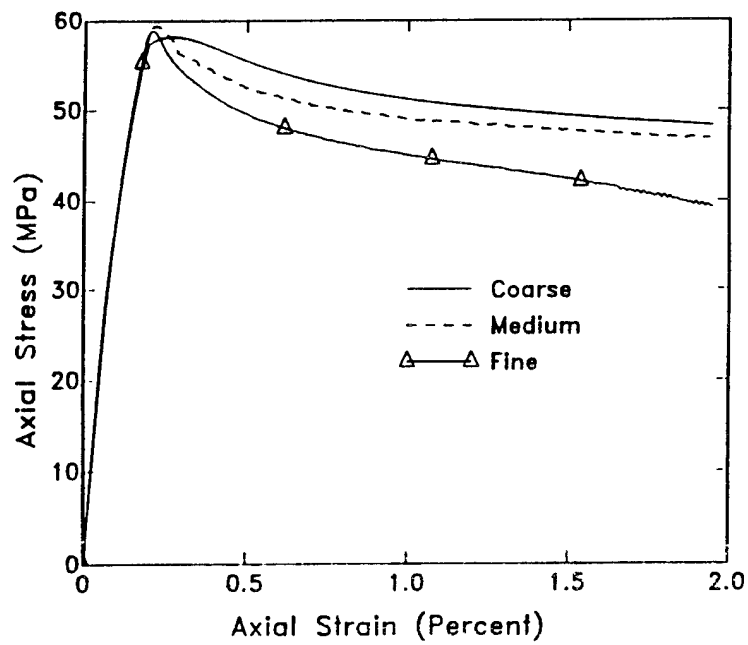
(a) Plane strain.
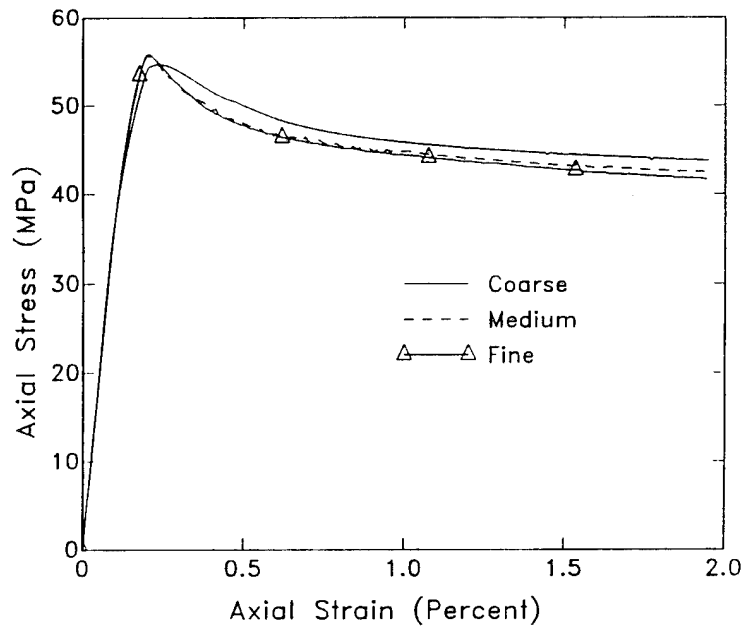
(b) Unconfined compression.

Figure 7.7. Comparison of coarse, medium, and fine mesh simulations for Round B lubricated specimens.
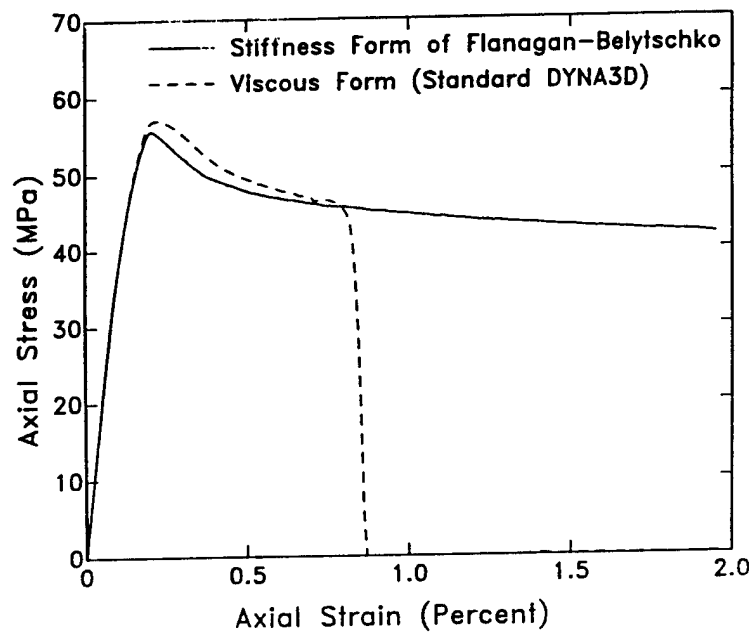
Figure 7.8. Effect of hourglass stability method on the unconfined, fine mesh calculation (B2-FUL).

SECTION 8

ROUND D BENCHMARKS: DYNAMICS OF

REINFORCED SLABS

The Round D benchmarks study the dynamics of reinforced concrete slabs in plane strain under various load levels. The geometry of the undeformed slab mesh in shown in Figure 8.1. The bottom surface of the slab coincides with the $x - y$ plane with plane strain in the y-direction. The vertical z-direction corresponds to the through-the-thickness direction of a concrete wall. The mesh is 10x1x6 solid concrete elements in the x-y-z directions, respectively. Thus 6 elements are modeled through-the-slab thickness. The dimensions of the slab are 380x25x114 mm. The bottom and top rows of elements are 13 mm high. All other elements are 22 mm high.
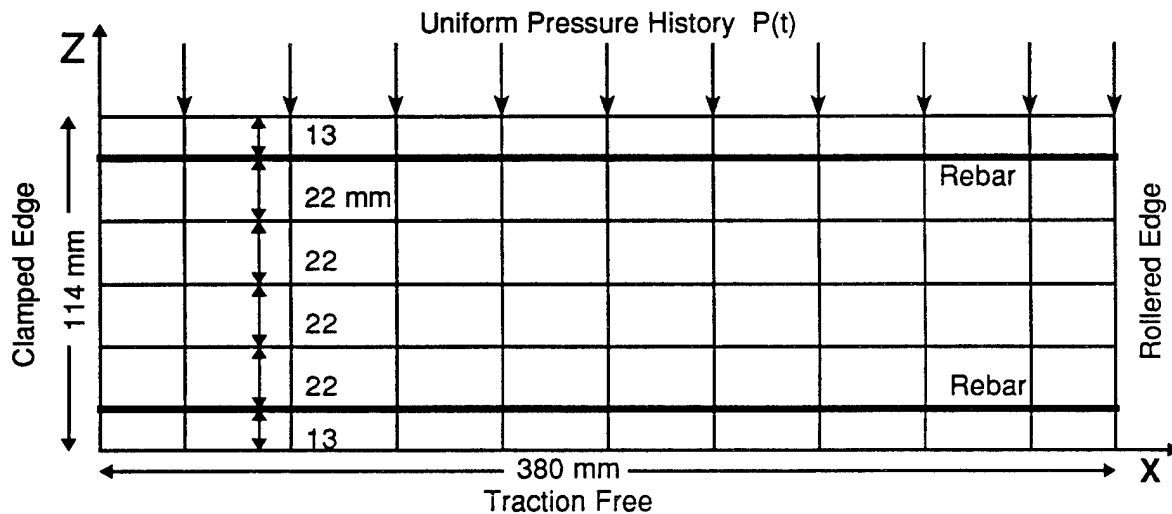
Figure 8.1. Geometry of slab in Round D benchmark calculations.

Two rebar are are bonded to the concrete, one between the first and second rows of elements, and one between the fifth and sixth rows of elements. The cross-sectional area of each rebar is 17.2 mm^2. The rebar are located on the front face at $y = 0$.

The left edge at $x = 0$ mm is clamped. The right edge at $x = 380$ mm is a roller boundary. It
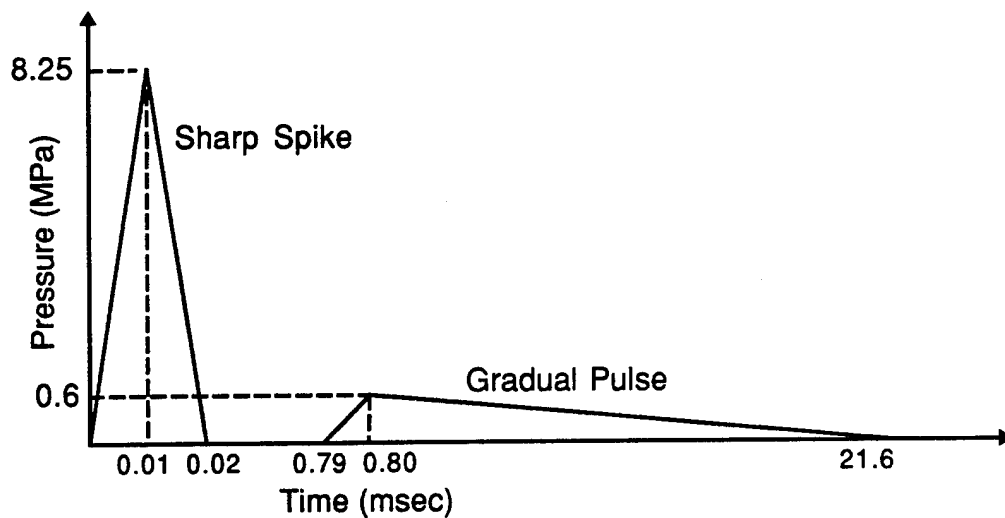
Figure 8.2. Unscaled pressure history applied to slab sections in Round D.

Table 8.1. Case designation and load factor for Round D pressure pulse.

Case	Load Factor LF
D1	0.6
D2	1.4
D3	2.2
D4	3.0

represents the midspan symmetry plane of a concrete wall. The front and back surfaces at $y = 0$ mm and $y = 25$ mm are roller boundaries to enforce the plane strain condition. The bottom surface at $z = 0$ mm is traction free. The top surface at $z = 114$ mm has a spatially uniform pressure history, $p(t)$, applied. The pressure history consists of a sharp spike followed by a more gradual pulse, as shown in Figure 8.2. The magnitude of this pressure history is scaled by the load factors given in Table 8.1 for four different cases. Before being scaled, the sharp spike initiates at 0 ms, peaks to 8.25 MPa at 0.01 ms, then decays to 0 Mpa at 0.02 ms. The more gradual pulse initiates at 0.79 ms, peaks to 0.6 Mpa at 0.80 ms, then decays to 0 MPa in 21.6 ms.

RDA compiled all benchmark participants results and reported them in Reference 11. The thrust, bending moment, shear force, and deflection histories compiled by RDA for APTEK are shown in Figure 8.3. The four calculations were run for 20 msec. Of particular interest are the displacement

histories calculated along the midspan symmetry plane at x=380 mm and $z = 57$ mm. The maximum downward displacement ranges from 0.026 cm for LF=0.6 to 13.9 cm for LF=3.0, which is almost three orders of magnitude in maximum displacement for a factor of 5 difference in scale factor. The time to reach the maximum displacement also increases with load factor.

The maximum displacement versus load factor and time to maximum displacement are compared in Figure 8.4 for all participants models. These comparisons demonstrate the extreme sensitivity of the maximum deflection to small changes in the applied load. Most calculations predict a large jump in deflection for load factors between 2.2 and 3.0, just as APTEK does.

Contours of damage are shown in Figure 8.5 through Figure 8.8 for cases D1 through D4, respectively. In all cases, tensile damage initiates on the clamped edge near the top (loaded) surface and along the bottom surface near the midspan. Very limited damage is predicted in calculation D1 by 20 ms. The location of this damage corresponds to the front face (loaded face) of a concrete wall near the edge. Much more severe damage is predicted in calculation D2 by 20 ms, particularly over the bottom surface of the slab. This surface corresponds to the backface of a concrete wall.

Contours of damage are predicted at 6 ms and 20 ms for calculations D3. The damage contours predicted at 20 ms are not significantly different than those predicted at 6 ms. These contours suggest that backface spall is likely to occur near the midspan.

Contours of damage at 6, 8.5, 11, and 20 msecs are shown for calculation D4. The entire slab is severely damaged by 8.5 ms. Note, however, that damage accumulation is reduced near the clamped edge by 11 ms. This is due to modeling modulus recovery or 'healing' of the bulk modulus, as previously discussed in Section 4. Initially, elements along the clamped edge go into tension ($P < 0$) and both the bulk and shear moduli are severely degraded. As the slab deforms further, some of the elements along the clamped edge go into compression ($P > 0$). In this case, the bulk modulus is recovered, or set back to its initial undamaged value. Although this example illustrates our modulus recover model, the model still must be verified against experimental data.
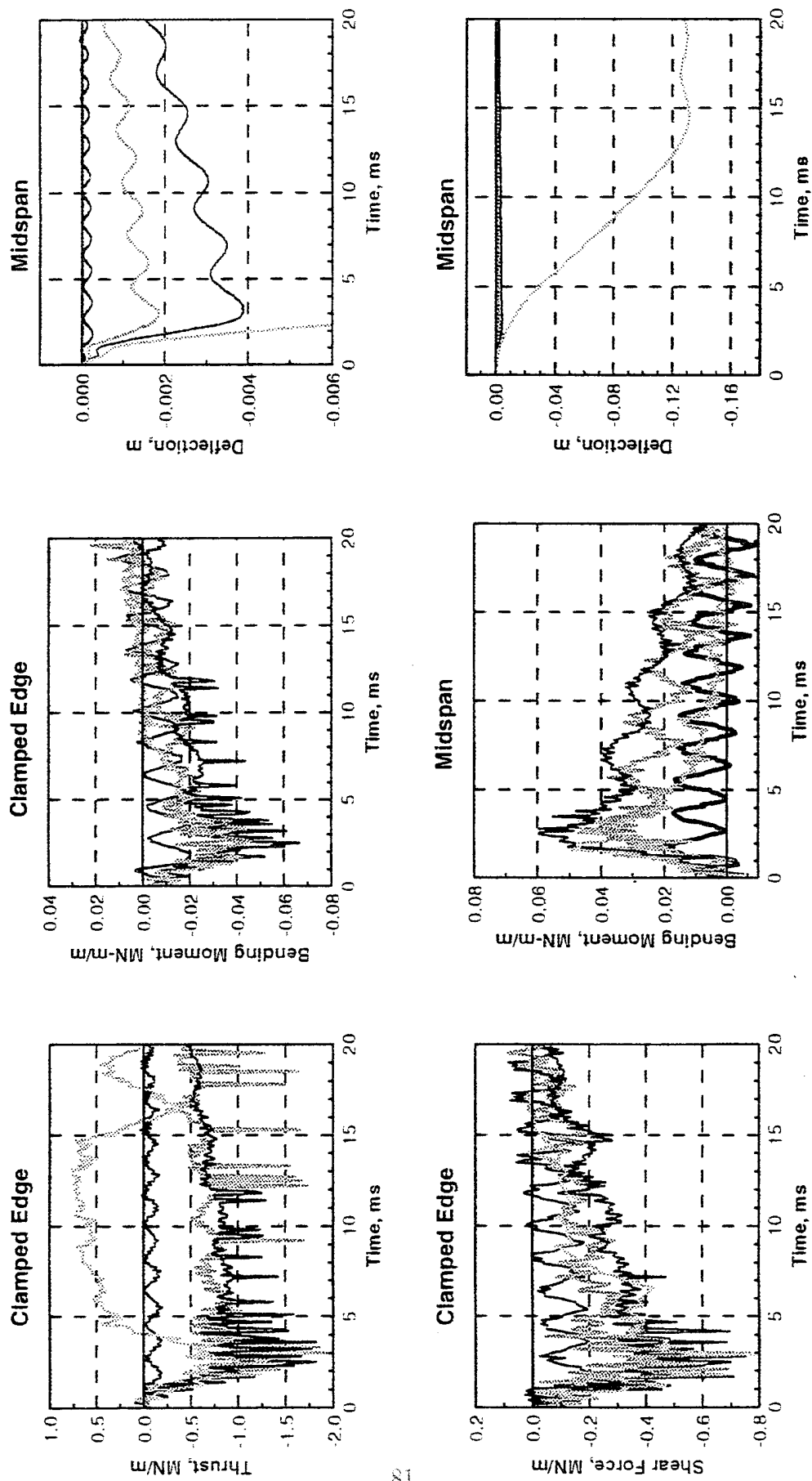
Figure 8.3. Deflections and resultants compiled by RDA for Round D slab sections.

Load Factor

0.6   1.4   2.2   3.0

81
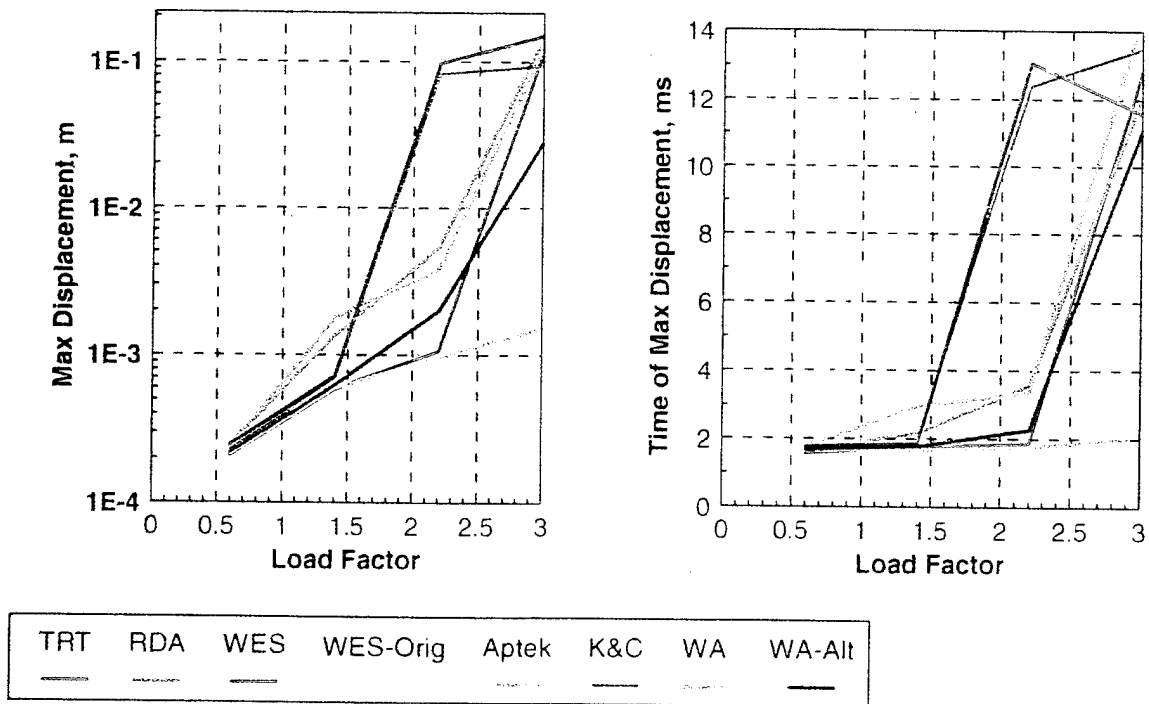
Figure 8.4. Maximum deflection versus load factor, compiled by RDA for Round D slab sections.
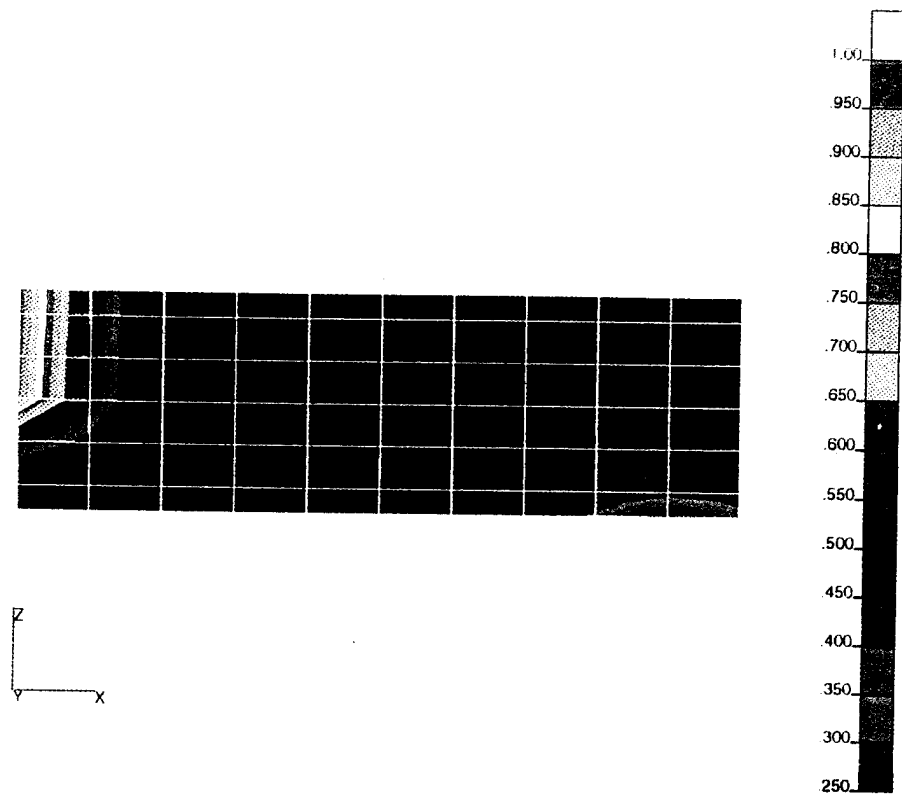
Figure 8.5. Contours of damage at 20 ms for Round D case D1 calculation.
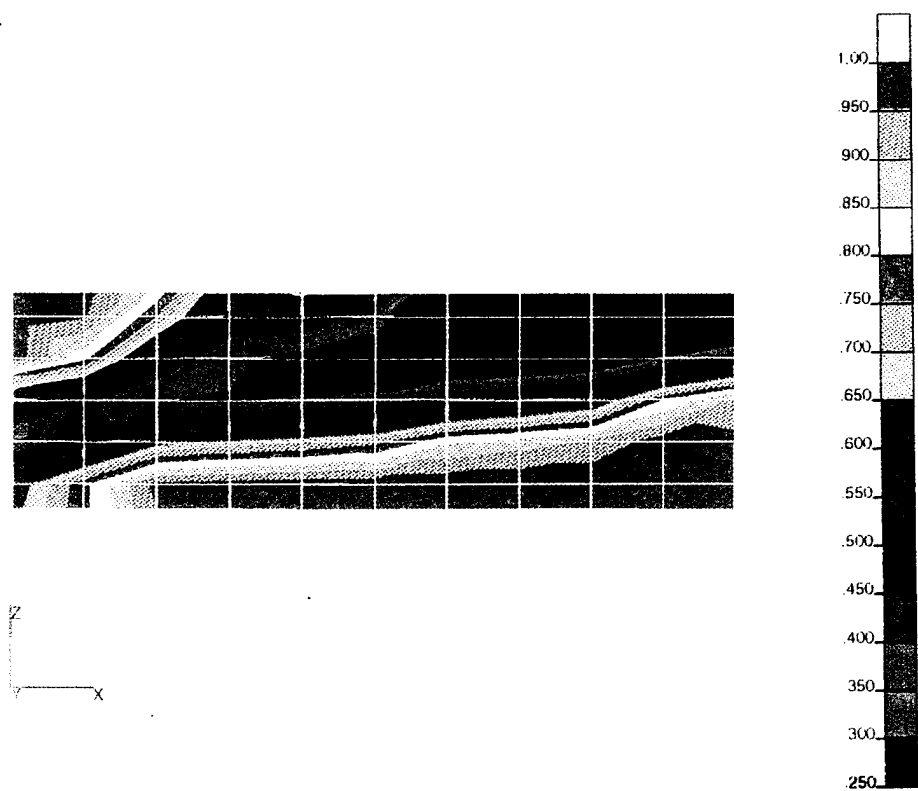
Figure 8.6. Contours of damage at 20 ms for Round D case D2 calculation.
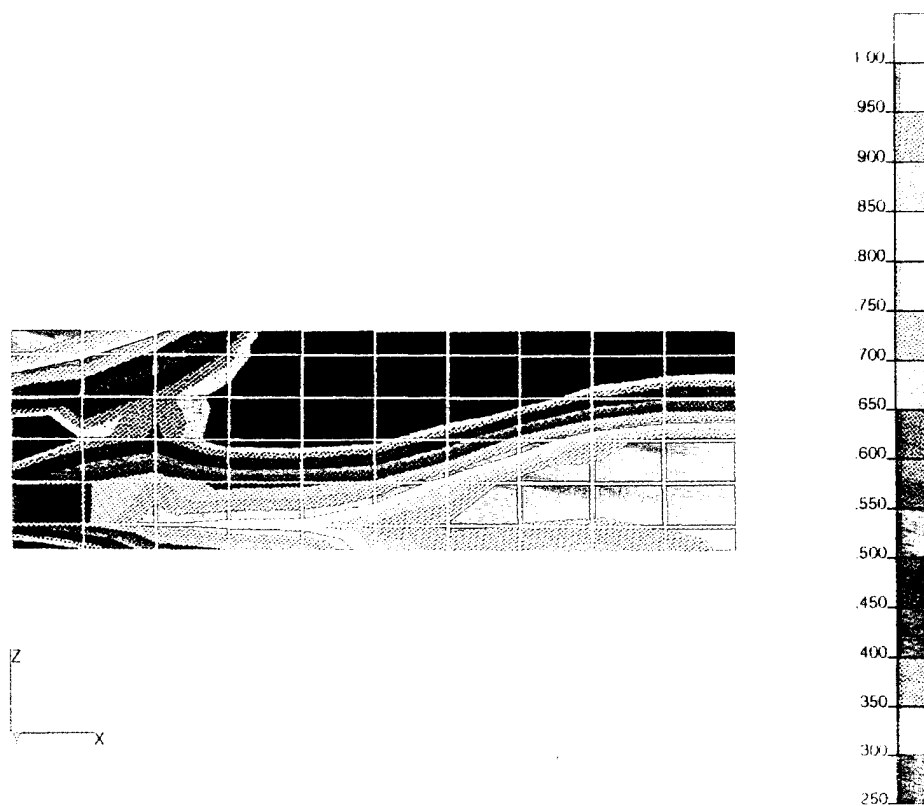
(a) 6 ms.
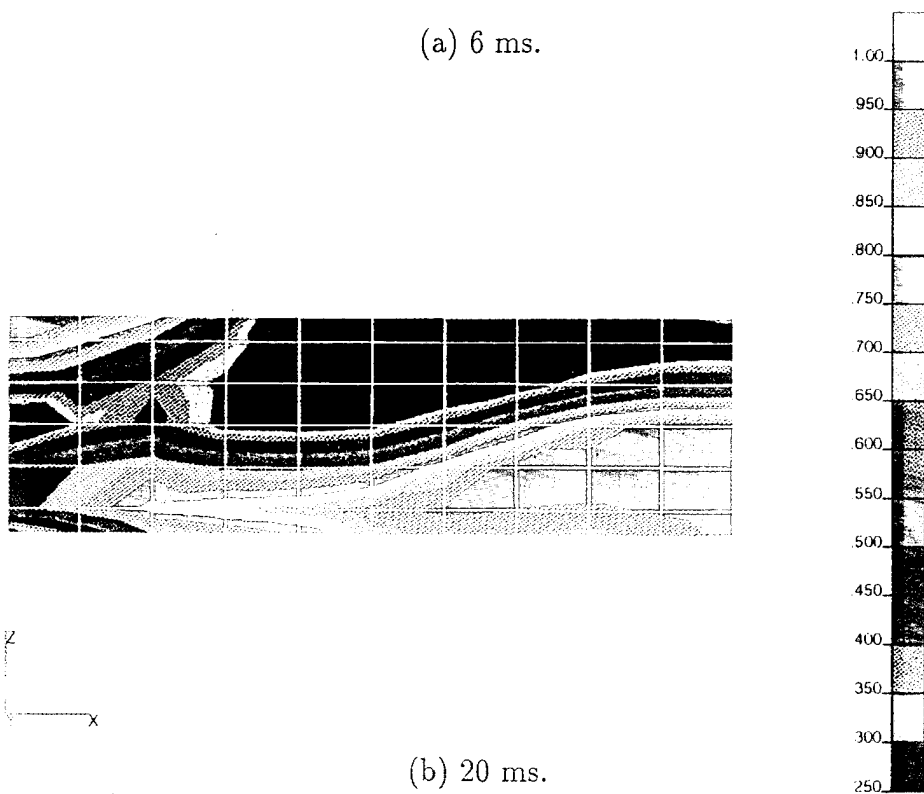
(b) 20 ms.

Figure 8.7. Contours of damage at two times for Round D case D3 calculation.
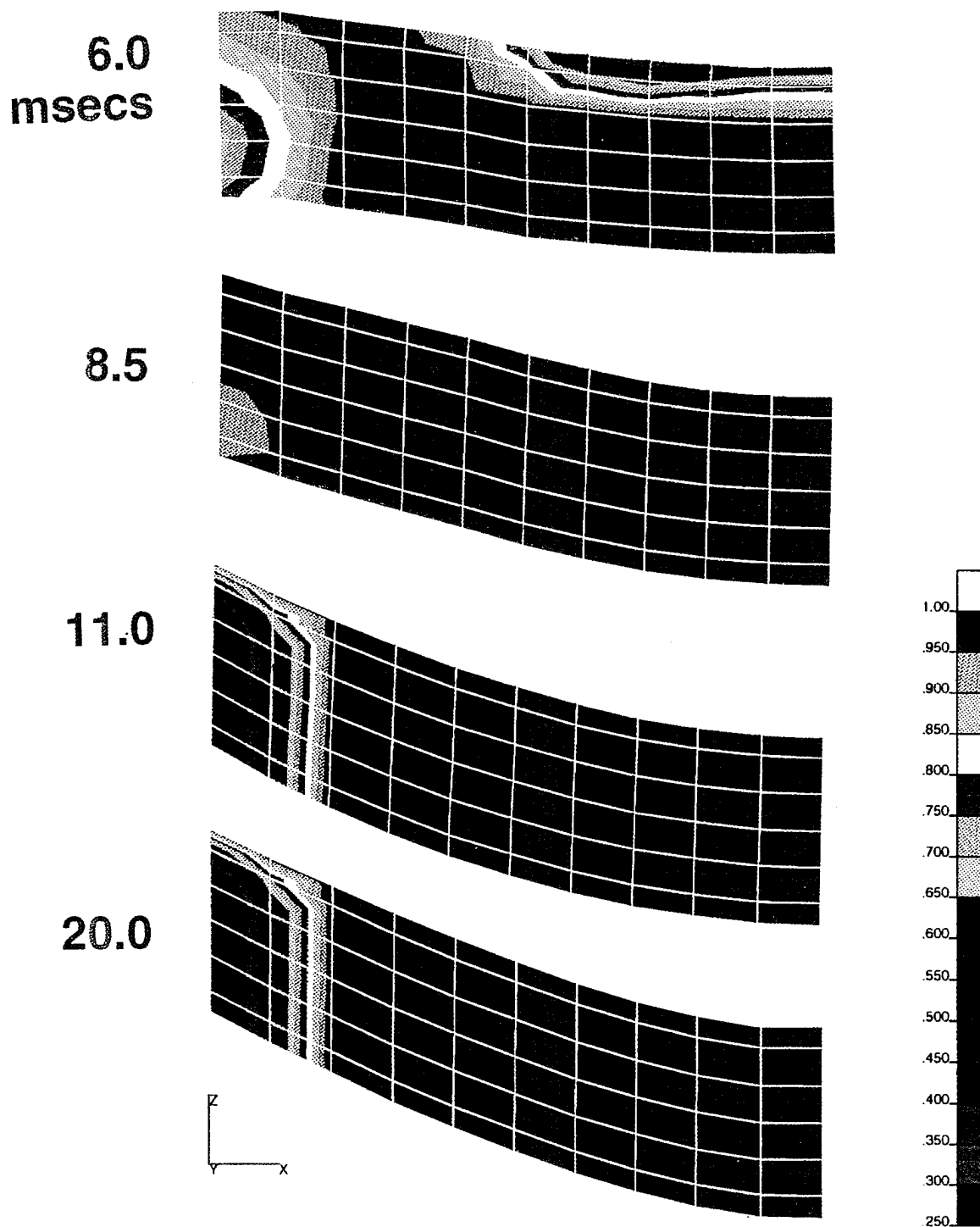
Figure 8.8. Contours of damage at four times for Round D case D4 calculation.

SECTION 9

SUMMARY AND FUTURE EFFORTS

The three-invariant smooth-cap model with isotropic damage models the essential features of concrete behavior. These features include different strengths in TXC and TXE, shear enhanced compaction, dilatancy, post-peak softening, degradation of the elastic moduli, and localized damage accumulation. The damage modeling efforts discussed in this report are a first attempt at modeling softening and modulus degradation, and all results should be considered preliminary. Numerous enhancements and studies are recommended for a follow-on effort, as follows:

- **Stress-Based vs. Strain-Based Models.** Simo and Ju developed alternative, but not equivalent, damage formulations for stress-based and strain-based models. Although we implemented their strain-based formulation for ductile response, future efforts will examine the appropriateness of stress vs. strain-based formulations, particularly for modeling cyclic response between the brittle and ductile regimes. Whichever type of formulation is selected, it will be used consistently for both brittle and ductile damage.

- **Continuity Between Brittle and Ductile Models.** Currently two separate models are implemented for the brittle (tensile pressure) and ductile (compressive pressure) regimes. Although the damage initiation threshold is modeled continuously between these two models, the *evolution* of the damage parameter and the accumulation of plasticity are discontinuous between these two models at $P = 0$. Future efforts will ensure that there is a continuous and smooth connection between modeling damage in the brittle and ductile regimes by merging the brittle and ductile models into a single, more sophisticated model. This model will contain a pressure-dependent damage initiation threshold throughout the compressive and tensile regimes, allow for slight plasticity in the tensile regime (as warranted by available data), and smoothly adjust the severity of the softening response (damage accumulation) between the tensile and compressive regimes.

- **Isotropic vs. Anisotropic Damage Models.** In addition to the isotropic damage formulation discussed in this report, Simo and Ju also developed an anisotropic damage formulation for modeling the tensile failure of concrete. Unlike the scaler damage variable used in the isotropic model, a fourth-order *tensor* characterizes damage in the anisotropic model. Future efforts will examine the feasibility of implementing their anisotropic model into our concrete damage model. We also plan to review the brittle anisotropic model recently implemented into DYNA3D by Govindjee in Reference 20.

- **Modeling the Effects of Preloading.** The measured reduction in modulus and strength due to preloading a specimen in uniaxial strain prior to direct pull or unconfined compression tests was was previously shown in Figure 1.4 for WSMR-5 concrete. Future efforts will predict the measured stress-strain responses and damage mechanisms. The main difficulty here is determining the evolution of a pressure-dependent damage threshold (through the softening parameters A and B) when cycling between tension and compression. In addition, the use of stress-based or strain-based damage models will have a significant affect on the calculated results.

SECTION 10

LIST OF REFERENCES

1. Whirley, R.G. and B.E. Engelmann, *DYNA3D: A nonlinear, Explicit, Three-Dimensional Finite Element Code for Solid and Structural Mechanics - User Manual*, Methods Development Group, Mechanical Engineering, Lawrence Livermore National Laboratory, UCRL-MA-107254, Rev. 1, Nov. 1993.

2. Pelessone, D., "A Modified Formulation of the Cap Model," Prepared for DNA under Contract DNA-0010086-C-0277, General Atomics, GA-C19579, January 1989.

3. Sandler, L.S. and D. Rubin, "An Algorithm and a Modular Subroutine for the Cap Model," *International Journal for Numerical and Analytical Methods in Geomechanics 3,*, pps. 173-186, 1979.

4. Simo, J.C. and J.W. Ju, "Strain- and Stress-Based Continuum Damage Models –I. Formulation", *International Journal of Solids and Structures*, Vol. 23, No. 7, pps 821-840, 1987.

5. Simo, J.C. and J.W. Ju, "Strain- and Stress-Based Continuum Damage Models –I. Formulation", *International Journal of Solids and Structures*, Vol. 23, No. 7, pps 841-869, 1987.

6. Hurlbut, B.J., "Experimental and Computational Investigation of Strain-Softening in Concrete," Department of Civil, Environmental, and Architectural Engineering, College of Engineering and Applied Science, University of Colorado, Boulder, Report to US AFOSR 82-0273, Oct. 1984.

7. Rubin, M.B., "Simple, Convenient Isotropic Failure Surface," *Journal of Engineering Mechanics*, Vol. 117, No. 2, Feb. 1991, pps. 348-369.

8. Simons, D., "DNA CWE Structures and Airblast Benchmark Meeting, Remarks on Softening, Concrete Material Model Descriptions", Logicon R&D Associates, Los Angeles, CA, April 28-19, 1993.

9. Simons, D., "DNA CWE Structural Response Calculations Meeting, Volume II - Round B Benchmark Problems 1 & 2," Logicon R&D Associates, Los Angeles, CA, Sept. 29-30, 1993.

10. Simons, D., "DNA CWE Structural Benchmark Meeting," Logicon R&D Associates, Los Angeles, CA, Jan. 17, 1994.

11. Simons, D., "DNA CWE Structural Analysis Meeting, Volume I - Lab Test Plans, Code Development, DE-21 Results, Benchmark Round D," Logicon R&D Associates, Los Angeles, CA, May 18-19, 1994.

12. Simo, J.C., J.G. Kennedy, S. Govindjee, "Non-Smooth Multisurface Plasticity and Viscoplasticity. Loading/Unloading Conditions and Numerical Algorithms," *International Journal for Numerical Methods in Engineering*, Vol. 26, 1988, pps. 2161-2185.

13. Mazars, J., "Mechanical Damage and Fracture of Concrete Structures", *Advances in Fracture Research (Fracture 81)*, Proceedings of the 5th International Conference on Fracture (ICF5), Vol. 4, Pergamon Press, pps 1499-1506, 1981.

14. Duvaut, G. and J.L. Lions, "Les Inequations en Mechanique et en Physique," Dunod, Paris, 1972.

15. Chen, W.F. and D.J. Han, *Plasticity for Structural Engineers*, Springer-Verlag New York Inc., 1988, pg 352.

16. Sandler, I.S. and T.C. Pucik, "Non-Uniqueness in Dynamic Rate-Independent Non-Associated Plasticity," LOGICON/R & D Associates, Los Angeles, CA, 1992.

17. Fung, Y.C. *A First Course in Continuum Mechanics*, Prentice Hall, Englewood Cliffs, N.J. 1969, pg. 143.

18. Schwer, L.E. and Y.D. Murray, "A Single Surface Three Invariant Cap Model with Mixed Hardening," *International Journal for Numerical and Analytical Methods in Geomechanics*, vol 18, pgs 657-688, 1994.

19. Ross, C.A. and J.W. Tedesco, "Effects of Strain-Rate on Concrete Strength," Presented at the American Concrete Institute 1991 Spring Convention, Washington D.C., March 1992.

20. Govindjee, S., G.J. Kay, and J.C. Simo, "Anisotropic Modeling and Numerical Simulation of Brittle Damage in Concrete," Submitted to *International Journal for Numerical Methods in Engineering*, Department of Civil Engineering, University of Cal. at Berkeley, 1994

21. Windham, J.E., *Mechanical Property Recommendations for Clay Backfill, Structure Grout, and In Situ Soils at the CONWEB Test Site, Fort Knox, KY*, Geomechanics Division, Structures Laboratory, US Army Engineer Waterways Experiment Station, Vicksburg, Mississippi, Prepared for DNA, February 1990.

22. Seaman, Lynn, *SRI PUFF 8 Computer Program for One-Dimensional Stress Wave Propagation*, SRI International Final Report on Project PYU-6802, Volume II, Prepared for U.S. Army Ballistics Research Laboratory, August 1978.

23. Kennedy, T.C. and H.E. Lindberg, "Model Tests for Plastic Response of Lined Tunnels," *Journal of the Engineering Mechanics Division*, ASCE, Vol. 104, No. EM2, Proc. Paper 13692, April 1978, pp. 399-410.

24. Florence, A.L. and L.E. Schwer, "Axisymmetric Compression of a Mohr-Coulomb Medium Around a Circular Hole," *International Journal for Numerical and Analytical Methods in Geomechanics*, Vol. 2, Issue No. 4, October-December, 1978, pp. 367-379.

25. Sokolnikoff, I.S. *Mathematical Theory of Elasticity*, McGraw-Hill Book Company, New York, 1956, pp. 32.

APPENDIX A

THREE INVARIANT SCALING FUNCTION $\mathcal{R}$

Rubin considers a three-invariant yield function of the general form:

$$f(J_1, \sigma_e, \beta) = \sigma_e - \mathcal{R}(J_1, \beta) Y_d(J_1) \qquad \text{(A.1)}$$

where $f = 0$ at failure and Y_d is the failure surface for TXC. The functional form of $\mathcal{R}$ proposed by Rubin is

$$\mathcal{R} = \frac{-b_1 + \sqrt{b_1^2 - 4b_2 b_0}}{2b_2} \qquad \text{(A.2)}$$

where

$$
\begin{aligned}
b_2 &= (\cos\beta - a\sin\beta)^2 + b\sin^2\beta \\
b_1 &= a(\cos\beta - a\sin\beta) \\
b_0 &= -(3 + b - a^2)/4 \\
b &= (2Q_1 + a)^2 - 3
\end{aligned}
$$

$$\text{(A.3)}$$

$$
\begin{aligned}
a &= \frac{-a_1 + \sqrt{a_1^2 - 4a_2 a_0}}{2a_2} \\
a_2 &= Q_2 \\
a_1 &= \sqrt{3}Q_2 + 2Q_1(Q_2 - 1) \\
a_0 &= 2Q_1^2(Q_2 - 1)
\end{aligned}
$$

The value of $\mathcal{R}$ in Equation A.2 depends on the state of stress through the angle β, and on experimentally determined values for Q_1 and Q_2 as functions of pressure. The function $\mathcal{R}$ provides the shape of the failure envelope in the octahedral plane. This shape may be that of a circle (MOSS), semi-regular hexagon (Mohr-Coulomb), or irregular hexagon-like shape in which each of the six sides is quadratic (rather than linear) between the TXC and TXE stress states.

The yield function previously given in Equation 2.18 for the APTEK concrete model is of the general form suggested by Rubin in Equation A.1, where $Y_d = \sqrt{3}F_f$ for $F_c = 1$. The general form of $\mathcal{R}$ given in Equation A.2 has been implemented into DYNA3D for pressure dependent values of Q_1 and Q_2.

A.1 REDUCTION OF $\mathcal{R}$ TO THE MOHR-COULOMB CRITERION.

Mohr's condition for pressure-dependent materials states that yielding occurs when the maximum shear stress reaches a critical value as a function of pressure, see Reference 15. Rubin derives an analytical expression for $\mathcal{R}$ for a nonlinear failure envelope as follows:

$$\mathcal{R}(\beta) = \frac{\sqrt{3}Q_2}{\left[(1 + Q_2)\cos\beta - \sqrt{3}(1 - Q_2)\sin\beta\right]} \tag{A.4}$$

where

$$Q_1 = \frac{\sqrt{3}Q_2}{1 + Q_2} \tag{A.5}$$

$$Q_2 = \frac{3 - \sin\varphi}{3 + \sin\varphi} \tag{A.6}$$

$$\tag{A.7}$$

and the friction angle φ may be pressure dependent.

The simplest form of Mohr's condition is known as the Mohr-Coulomb criterion and is graphically represented in Figure A.1 as a straight-line envelope of failure states in normal stress, σ, versus shear stress, τ, space. The principal stresses are $\sigma_1 \geq \sigma_2 \geq \sigma_3$. Two experimentally determined constants define the straight-line envelope: the cohesion, c, and the friction angle, φ, as follows:

$$|\tau| = c - \sigma\tan\varphi \tag{A.8}$$

The principal stresses, and hence $|\tau|$, can be defined in terms of the three stress invariants, J_1, $\sqrt{J_2'}$, and β. The failure envelope also forms a straight line in $\sqrt{J_2'}$ vs J_1 stress invariant space.
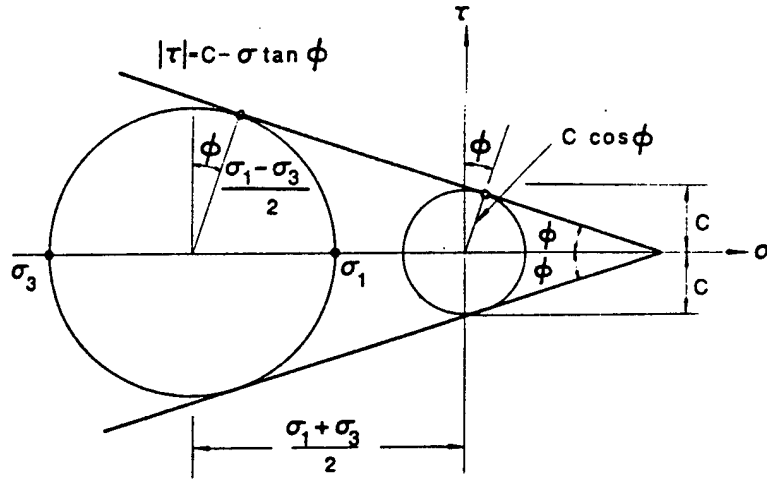
Figure A.1. Mohr-Coulomb criterion with a straight-line failure envelope.

APTEK's three-invariant yield function, Equation 2.18, is equal to a straight-line Mohr-Coulomb criterion if $\mathcal{R}$ is given by Equation A.4, and the failure surface parameters α and θ are related to the friction angle, φ, and unconfined compressive strength, σ_u, as follows:

$$\alpha = \frac{6c\cos\varphi}{\sqrt{3}(3-\sin\varphi)} \tag{A.9}$$

$$\theta = \frac{2\sin\varphi}{\sqrt{3}(3-\sin\varphi)} \tag{A.10}$$

where

$$c = \frac{\sigma_u}{2\sqrt{N}} \tag{A.11}$$

$$N = \frac{1+\sin\varphi}{1-\sin\varphi} \tag{A.12}$$

The failure surface parameters and $\mathcal{R}$ depend on the same pressure-independent friction angle. For most soils, the friction angle is $\varphi \approx 30$ degrees.

One point to note is that the three-invariant model is more general than a strict Mohr-Coulomb criterion. As previously noted for the Mohr-Coulomb criterion, the shape of the failure envelope in the $\sqrt{J_2'}$, J_1 plane, and the shape of the semi-regular hexagon in the octahedral plane, depend

A-3

on the same friction angle φ. φ is constant for a straight-line envelope and a function of pressure for a non-linear envelope. In the three-invariant model, φ may be used to determine the shape of the irregular hexagon in the octahedral plane. The failure surface function, F_f, may be specified independently of φ, and does not have to be linear even though a constant value for φ is specified.

A.2 REDUCTION OF $\mathcal{R}$ TO THE MAXIMUM-OCTAHEDRAL-SHEAR STRESS CRITERION.

This criterion states that yielding begins when the octahedral-shear stress reaches a critical value. Rubin assumes a slight generalization of the MOSS condition by allowing the critical value to be a function of pressure. Rubin demonstrates that, for this case, the function $\mathcal{R}$ reduces to $\mathcal{R} = Q_1 = Q_2 = 1$. Thus the failure curve Y_d is not scaled for different states of stress. The yield function in Equation A.1 reduces to a two-invariant yield function. For this generalized criterion, the failure envelope is nonlinear with pressure, but remains a circle in the octahedral plane.

The Drucker-Prager and Von Mises criteria are special cases of the generalized MOSS criterion. The straight-line envelope of the Drucker-Prager criterion forms a cone in principal stress space, while the pressure-independent Von Mises envelope forms a cylinder.

A.3 REDUCTION OF $\mathcal{R}$ TO A WILLAM-WARNKE MODEL.

The Willam-Warnke model is a subset of the more flexible Rubin model previously discussed in Section 2.4.2. In these models, the shape of the failure surface in the deviatoric plane transitions with pressure. This means that the ratio of the TXE to TXC failure surface increases with pressure, as does the ratio of the TOR to TXE failure surfaces. In a Willam-Warnke model, the TOR/TXE ratio depends specifically on the TXE/TXC ratio at each pressure value. In the more general Rubin model, the TOR/TXE ratio can be specified independently of the TXE/TXC ratio.

The Willam-Warnke model was the specification for the Round D and E benchmarks. However, no TXE or TOR data was measured for WSMR-5 concrete. Instead of fitting our model to data, RDA

specified the location and shape of the TXE surface along the hydrostat, denoted Ψ_2, as follows:

$$\Psi_2(P) = \begin{cases} 0.686 & P \leq 75 \text{ MPa} \\ 0.610 + 0.00102P & 75 \text{ MPa} < P < 382 \text{ MPa} \\ 1.0 & P \geq 382 \text{ MPa} \end{cases} \qquad (A.13)$$

In addition, RDA specified that the shape of the failure surface in the deviatoric plane must transition with pressure according to a Willam-Warnke model.

To model the Willam-Warnke failure surface, we fit the functional form of our TXE surface, $Q_2(P)$, to RDA's specification in Equation A.13. Then we derived the location of the Willam-Warnke TOR surface, denoted Ψ_1, from the following formula:

$$\Psi_1(P) = \frac{\sqrt{3}(1 - Q_2^2) + (2Q_2 - 1) * \sqrt{3(1 - Q_2)^2 + 5Q_2^2 - 4Q_2}}{3(1 - Q_2^2) + (1 - 2Q_2)^2} \qquad (A.14)$$

where Q_2 is a function of pressure. This formula can readily be reduced from textbook formulas for radius of the Willam-Warnke model in the deviatoric plane (see, for example, Reference 15). Finally we fit the functional form of our TOR surface, $Q_1(P)$, to the derived specification in Equation A.14.

The Rubin model can accommodate a wide range of three-invariant model behaviors. Although our model meets the Willam-Warnke benchmark specifications, we have the flexibility to adjust our model if those specifications turn out to be inappropriate for high-strength concrete. For example, if TXE and TOR concrete data is measured, our model can be directly fit to that data, even if the data does not transition according to a Willam-Warnke model.

APPENDIX B

EXPLICIT PORE COMPACTION MODEL FOR SOILS

In the CONWEB test series in Reference 21, high stress levels are generated in soil in the vicinity of an explosive charge. Mechanical property data for backfill materials used in these tests, i.e., dynamic uniaxial stress-strain data indicate that the backfill materials stiffen at high stress levels. Hence they are not adequately modeled with a constant bulk modulus model. In consultations with Professor Miles Rubin of the Israel Technion Institute, it was decided that a Mie-Grüneisen equation of state, coupled with explicit treatment of pore collapse at low pressure, would be an appropriate representation for both low and high pressure states. The Mie-Grüneisen equation and fitting procedures to Hugoniot shock data are well established. We have integrated it into the smooth-cap model to treat in a continuous manner both high and low pressure behavior. The theory of the Mie-Grüneisen model and evaluation of the implementation are discussed in the next two subsections.

B.1 THEORY.

Consider a geologic material, such as soil, which consists of solid particles with voids between particles, called 'pores'. Let V be the initial volume of the soil in the unstressed state, and v the current volume in the stressed state. The total volume of the soil is the sum of the volumes of the solid particles, denoted by the subscript 's', and the pores, denoted by the subscript 'p', as follows:

$$
\begin{aligned}
V &= V_s + V_p \\
v &= v_s + v_p
\end{aligned}
\tag{B.1}
$$

The relative volume of the soil, J, is the ratio of the current to initial volume, $J = v/V$.

The pressure in the soil is taken to depend on the pressure in the solid particles, P_s, and the soil

porosity, ϕ, in the following form:

$$P = [1 - \phi(\kappa)]P_s(E_s, J, \kappa) \tag{B.2}$$

in which κ is the cap hardening parameter and E_s is the specific internal energy per unit mass in the solid particles, calculated from the strain energy and mass of the material. Heat transfer is neglected. The soil porosity is the ratio of the current pore volume to the current soil volume, $\phi = v_p/v$. The initial porosity of the soil is $\Phi = V_p/V$. Note that the pressure in the soil is equal to the pressure in the solid particles when the porosity is zero, i.e., $P = P_s$ when $\phi = 0$. Until the pores are fully collapsed, the soil pressure is less than the solid particle pressure, i.e., $P < P_s$ when $\phi > 0$.

To determine the pressure in the soil, expressions for the solid particle pressure and the porosity must be defined. The pressure in the solid particles is given by the Mie-Grüneisen equation of state. The porosity is defined in terms of the cap hardening relation. This relation describes the plastic volume strain as a function of κ. Expressions for these quantities are given the following two sections.

B.1.1   Mie-Grüneisen Equation of State.

The Mie-Grüneisen equation gives the pressure in a material as a function of internal energy and density, related to pressures and energies along a reference curve at the same density. The form of the Mie-Grüneisen equation given in Reference 22 is:

$$P - P_{\text{ref}} = \rho\Gamma(E - E_{\text{ref}}) \tag{B.3}$$

where P is pressure, E is internal energy, ρ is density, and the subscript 'ref' indicates the reference state. Γ is a material parameter called the Grüneisen ratio, and is obtained from laboratory test data. It is is assumed to be a function of the density only; in particular, $\rho\Gamma$ = constant in the present theory.

The Mie-Grüneisen equation extends information from known pressure-volume and energy-volume

states, typically the Hugoniot states for shocked material, to other values of pressure and energy. With the Hugoniot for the solid particles as the reference state, denoted by the subscript 'hs', the pressure in the solid particles is given by:

$$P_s = P_{hs} + \rho_s \Gamma_s (E_s - E_{hs}) \qquad (B.4)$$

The pressure and energy in the solid particles along the Hugoniot are given by:

$$P_{hs} = \frac{\rho_{0s} c_0^2 \phi_{cs}}{(1 - S_l \phi_{cs})^2} \qquad (B.5)$$

$$E_{hs} = \frac{c_0^2 \phi_{cs}^2}{2(1 - S_l \phi_{cs})^2} \qquad (B.6)$$

where ρ_{0s} is the initial density of the solid particles, c_0 is the bulk sound speed in the solid at low pressures, and S_l is the slope of a linear fit to shock velocity versus particle velocity data from shock tests. The constant product $\rho_s \Gamma_s$ is equal to the product of the initial values, $\rho_{0s} \Gamma_{0s}$. The parameter ϕ_{cs} is the relative change in the volume of the solid particles, given by:

$$\phi_{cs} = 1 - \frac{v_s}{V_s} = 1 - \frac{1 - \phi}{1 - \Phi} J \qquad (B.7)$$

Note from Equations B.5 and B.6 that the Hugoniot pressure and energy in the solid particles are zero when the change in volume of the solid particles is zero.

B.1.2 Soil Porosity.

An expression is derived in this section for $\phi(\kappa)$, which is the soil porosity as a function of the cap hardening parameter. This is accomplished in two steps. First, an expression is given for the soil porosity as a function of the the plastic volume strain. Second, a cap hardening relation is defined which provides the plastic volume strain as a function of κ.

It is assumed that the plastic volume strain of the soil is a function of the porosity only in the following form:

$$\epsilon_v^p = 1 - \frac{1 - \Phi}{1 - \phi} \qquad (B.8)$$

The initial porosity of the soil in the unstressed state is Φ, and the initial plastic volume strain is zero. As the soil is compressed, the pores collapse until the porosity is zero. At this state, the plastic volume strain is maximum and is equal to the initial porosity. No further plastic volume strain is allowed. Thus, from Equation B.8,

$$\epsilon_v^p = 0 \quad \text{when} \quad \phi = \Phi$$

$$\epsilon_v^p = \Phi \quad \text{when} \quad \phi = 0 \tag{B.9}$$

Rearrangement of Equation B.8 gives the current porosity as a function of the plastic volume strain:

$$\phi = 1 - \frac{1 - \Phi}{1 - \epsilon_v^p} \tag{B.10}$$

The cap hardening equation provides a relation between the plastic volume strain, ϵ_v^p, and the hardening parameter, κ. For the smooth-cap model this relation is:

$$\epsilon_v^p = W\left\{1 - e^{-D[X(\kappa)-X_0]-D_2[X(\kappa)-X_0]^2}\right\} \tag{B.11}$$

The parameter $W = \Phi$ is the maximum plastic volume strain. The function $X(\kappa)$ is the value of the first stress invariant, J_1, at the intersection of the cap with the J_1 axis. The parameter X_0 is the value of X evaluated at κ_0, the initial value of the hardening parameter. The parameters D and D_2 are obtained by fitting Equation B.11 to experimental data.

B.2 EVALUATION OF THE IMPLEMENTATION.

Stress-strain histories calculated with the Mie-Grüneisen model are shown in Figure B.1. These comparisons are for McCormick Ranch Sand during loading and unloading in uniaxial strain. Properties of McCormick Ranch Sand reported in Reference 3, and values assumed for Γ_{0s} and S_l, are given in Table B.1.

The response of the Mie-Grüneisen model during loading and unloading in the low pressure region is compared in Figure B.1a with the response calculated with a constant bulk modulus model. The
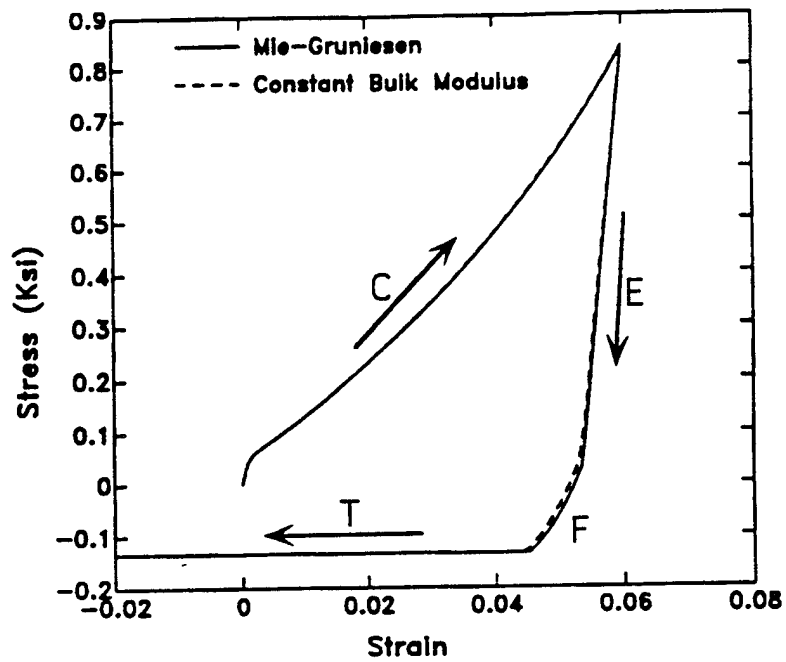
(a) Low pressure behavior.
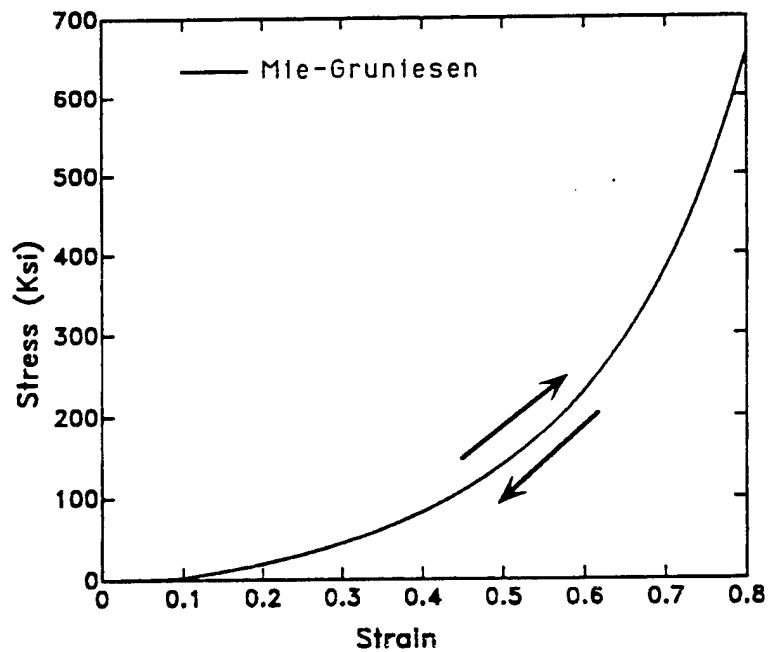
(b) High pressure behavior.

Figure B.1. Stress-strain histories calculated with Mie-Grüneisen model implemented in DYNA3D.

B-5

Table B.1. Parameter values for Mie-Grüneisen demonstration problem.

Constant Bulk Modulus Model

K (ksi)	66.7
G (ksi)	40.0
ρ (lbf/in^3)	0.07

Mie-Grüneisen Model

c_0 (in/s)	19250
Γ_{0s}	2.0
S_l	1.5
G (ksi)	40.0
ρ (lbf/in^3)	0.07

Failure Envelope

$$F_f(J_1) = \alpha - \gamma e^{-\beta J_1} + \theta J_1$$

α (psi)	250
θ	0
λ (psi)	180
β (psi^{-1})	0.67×10^{-3}

Moveable Cap

$$F_c(J_1, \kappa) = 1 - \frac{(J_1 - L)(|J_1 - L| + J_1 - L)}{2(X - L)^2}$$

$$X(\kappa) = L + RF_e(L)$$

$$L(\kappa) = \max(\kappa_0, \kappa)$$

R	2.5
X_0 (ksi)	0.0

Cap Hardening Rule

$$\epsilon_v^p = W\{1 - e^{-D[X - X_0] - D_2[X - X_0]^2}\}$$

W	0.066
D (psi^{-1})	0.67×10^{-3}
D_2 (psi^{-1})	0.0

responses are in good agreement, which validates the low pressure behavior of the Mie-Grüneisen-smooth-cap implementation.

During compressive loading to about 10% strain, collapse of the pores and compression of solid particles occurs when the active portion of the model is the cap mode, designated by 'C' in Figure B.1a. Collapse of the pores reduces the porosity of the soil. All plastic volume strain is due to the change in porosity. In this example problem, all pores are completely collapsed, the porosity is zero, and the plastic volume strain is maximum ($\epsilon_v^p = W$) at about 10% strain. The partitioning of total strain into elastic and plastic components depends on user selection of the parameters of the cap and failure surfaces.

During loading or unloading in the elastic regime, designated by 'E' during unloading in Figure B.1a, changes in pore and solid particle volume also occur, but in such a manner that the porosity remains constant. Hence no changes in plastic volume strain occur.

The response of the Mie-Grüneisen model in the high-pressure region is shown in Figure B.1b. Loading and unloading occur along the same stress-strain curve for strains greater than about 10%, i.e., all incremental strains are elastic and due to deformation of the solid particles. Below 10% strain, loading and unloading are along different stress-strain paths, similar to the low pressure behavior previously shown in Figure B.1a.
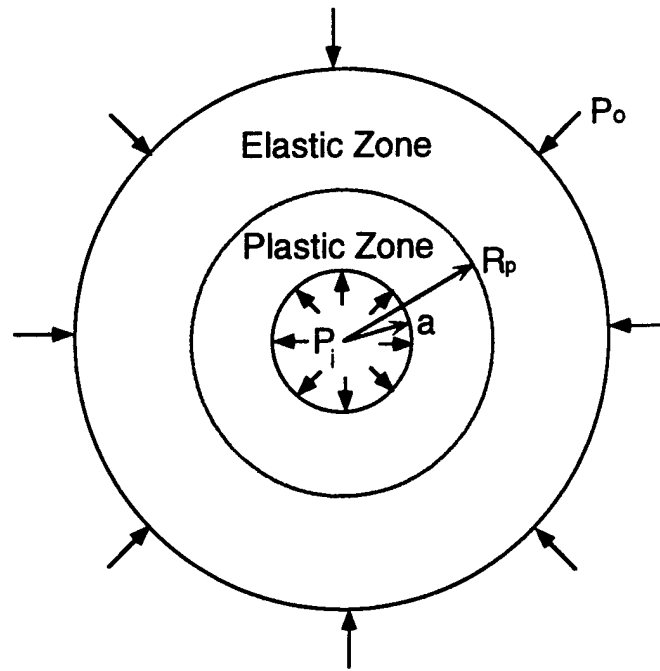
Figure C.1. Axisymmetric compression of a Mohr-Coulomb medium around a circular hole.

APPENDIX C

VERIFICATION OF THE THREE-INVARIANT MODEL

Kennedy and Lindberg [23] and Florence and Schwer [24] provide the stress-strain response of a Mohr-Coulomb medium for axisymmetric compression around a circular hole. The medium is subjected to an increasing free-field pressure, P_o, and a constant internal pressure, P_i, as shown schematically in Figure C.1. A plane strain condition is imposed. Yielding initiates on the inner boundary of the hole. The radius R_p of the yielded region increases with increasing free-field pressure.

Analytical results are calculated for a straight-line (constant friction angle) yield criterion. Material properties used in the analysis are given in Table C.1. Analytical stress-load and strain-load histories are shown in Figure C.2. The response is elastic-perfectly plastic, with the plastic response initiating at about $P_o = 11$ ksi. These histories are calculated at a radius of $r = 2$ inches from the center of the hole. The value of the normalized invariant, $\hat{J}_3$, and hence $\mathcal{R}$, varies throughout the elastic and plastic regimes.

A constant bulk modulus, K_0, is used to calculated the pressure-volumetric strain response of the medium. In addition, the elastic volumetric strain, ϵ_{kk}^e, is the difference between the total
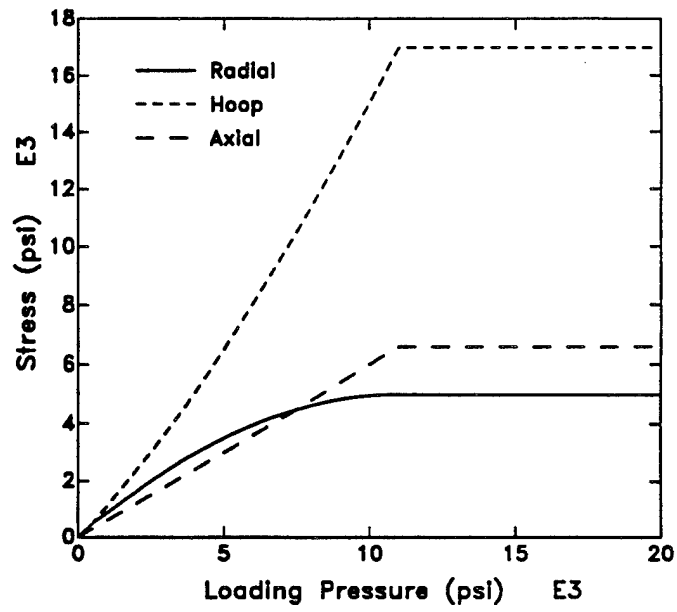
(a) Stress-load histories.
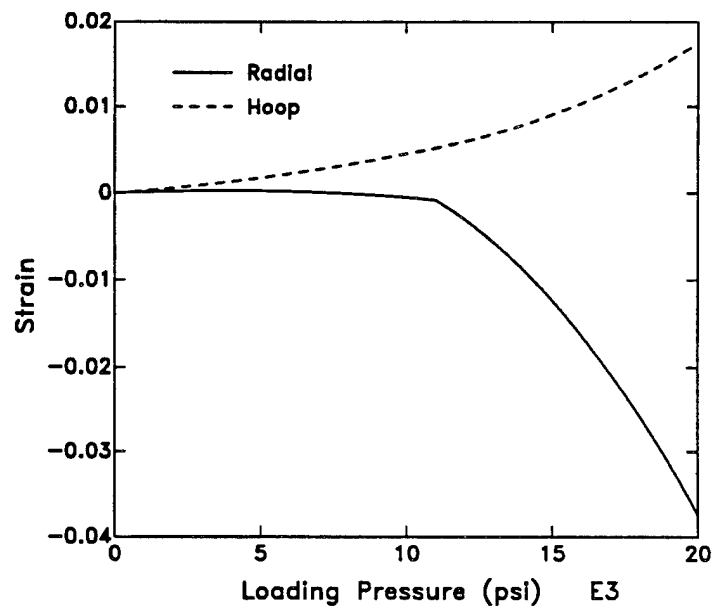
(a) Strain-load histories.

Figure C.2. Analytical results for the axisymmetric compression of a Mohr-Coulomb medium around a circular hole.

Table C.1. Material properties used in analysis of a Mohr-Coulomb medium.

ν	0.3
G (ksi)	1000
σ_u (psi)	2000
ϕ (degrees)	30
P_i (psi)	500
a (inch)	1.0
r (inch)	2.0

volumetric strain, ϵ_{kk}, and the plastic volumetric strain, ϵ_{kk}^p (the double subscript indicates the use of the summation convention). The analytical pressure-volumetric strain response is as follows:

$$P = K_0(\epsilon_{kk} - \epsilon_{kk}^p) \qquad (C.1)$$

This is a different pressure relation than used in APTEK's explicit pore collapse model, so the analytical results cannot be used to directly verify the implementation of the third invariant in the explicit pore collapse model. However, the analytical results can be used to verify the implementation of the third invariant in the constant bulk modulus model.

Comparisons Between the Analytical and Constant Bulk Modulus Models. In the DYNA3D calculations, the analytical strain histories shown in Figure C.2(b) are applied to a single element[1]. DYNA3D output stress histories are compared with the analytical stress histories shown previously in Figure C.2(a). Material parameters used in the calculations are given in Table C.2 and correspond to those in Table C.1. The DYNA3D failure surface parameters α and θ are related to the friction angle, φ, and unconfined compressive strength, σ_u, used in the analyses (see Equations A.9 and A.10).

As shown in Figure C.3, the numerical results are in excellent agreement with the analytical results throughout the elastic and plastic regimes. This validates the extension of the constant bulk modulus model to three invariants. In particular, it validates all modifications to yield function, return mapping algorithm, and the stress update. These same modifications are implemented in

---

[1] They are interpreted by the DYNA3D material model driver as strain-time histories.

Table C.2. Material properties used in three-invariant extensions of APTEKs models.

Bulk Modulus Model		Mie-Grüneisen Equation of State	
K_0 (ksi)	2167	c_0 (in/s)	109700
K_1 (psi)	0	Γ	0
K_2 (psi)	0	S_l	0
G (ksi)	1000	G (ksi)	1000
ρ (lbf/in^3)	0.070	ρ (lbf/in^3)	0.07

Failure Envelope

α (psi)	692.8
θ	0.231
λ (psi)	0
β (psi^{-1})	0

Cap and Hardening Rule

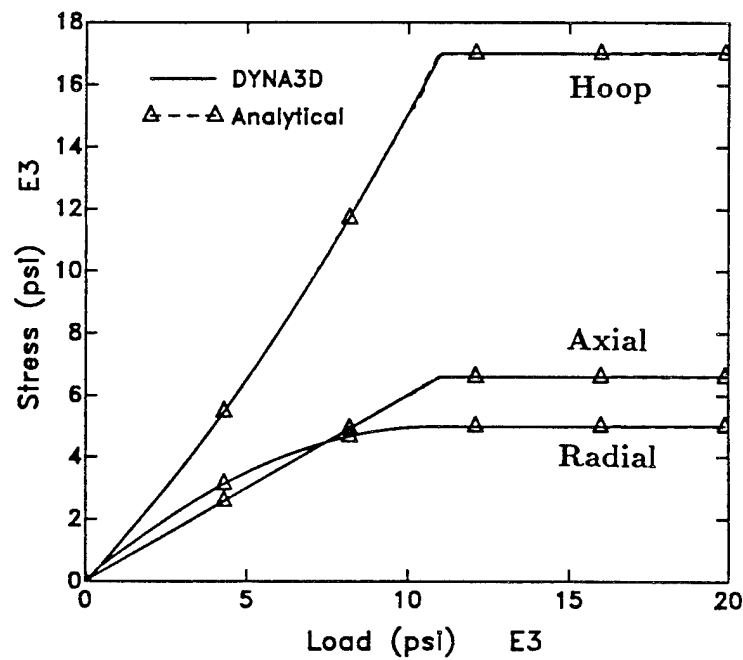|	
R	0.1
X_0 (psi)	1×10^5
Φ	0.05
D (psi^{-1})	0.67×10^{-4}
D_2 (psi^{-1})	0.0

Figure C.3. Comparison of analytical results using a Mohr-Coulomb criterion with numerical results using a three-invariant model with constant bulk modulus.
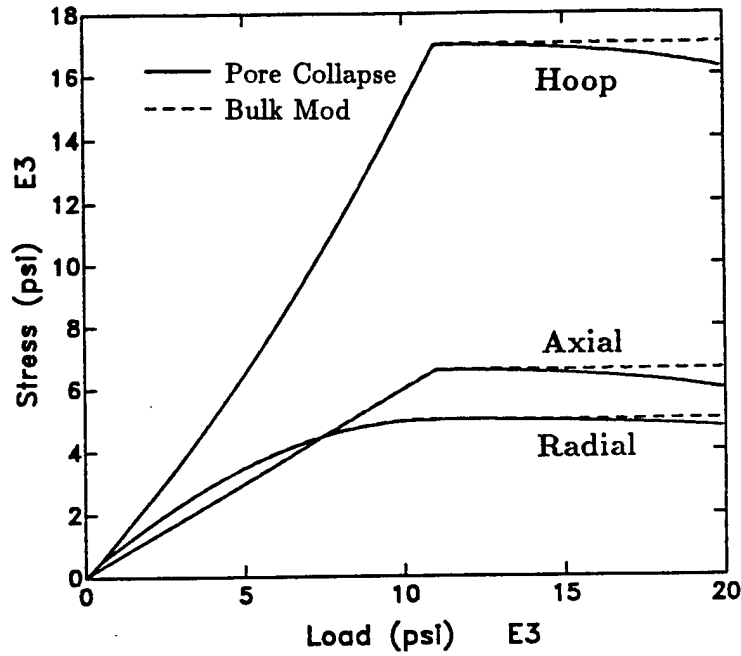
Figure C.4. Comparison of stress-load histories calculated with the explicit pore collapse and constant bulk modulus models extended to three invariants.

the explicit pore collapse model.

Comparisons Between the Explicit Pore Collapse and Constant Bulk Modulus Models.

Comparisons between the three-invariant extensions these cap models are given in Figure C.4. All properties were previously given in Table C.2. Stress-load histories are in agreement throughout the elastic response and during the early portion of the plastic response. However, the histories diverge with increasing load because the models use different pressure relations.

The pressure relation used in the explicit pore collapse model is:

$$P = (1 - \phi)P_s \qquad (C.2)$$

where ϕ is the porosity and P_s is the pressure (refer to Appendix B). The solid particle pressure is represented by the Mie-Grüneisen equation of state. Through appropriate selection of model parameters ($\Gamma = 0$, $S_l = 0$), Equation C.2 is reduced to a model with a constant solid-particle bulk modulus, K_{0s}:

$$P = (1 - \phi)K_{0s}(1 - J_s) \qquad (C.3)$$

where J_s is the relative volume of the solid particles. The term $1 - J_s$ is the change in volume of

the solid particles relative to the initial solid particle volume.

There are three differences between the pore collapse and constant bulk modulus (analytical) pressure relations given by Equations C.3 and C.1, respectively:

1. The models have different bulk moduli. In the pore collapse model, the modulus of the solid particles, K_{0s}, is constant. The effective modulus, K, depends on the porosity as well as the solid particle modulus, namely: $K = (1 - \phi)K_s$. Thus the effective modulus varies between an initial value of $(1 - \Phi)K_s$ before any pores are compressed, and a final value of K_s once all pores are fully crushed. Φ is the initial porosity. In the analytical model, the effective modulus, K_0, is constant. It is related to the solid-particle modulus and initial porosity of the pore collapse model, as follows: $K_0 = (1 - \Phi)K_{0s}$.

2. The models calculate dilatation differently. In the pore collapse model, the total relative volume, J, is accurately calculated from the determinant of the deformation gradient matrix. In turn, the solid particle volume, J_s, depends on J and ϕ as follows: $J_s = J(1 - \phi)/(1 - \Phi)$. If the relative volume is defined as $J = 1 - \Delta$, then Δ is the change in volume per unit volume, and is called the dilatation (see Reference 25). In the analytical model, the total volumetric strain is a first order, small strain approximation of the dilatation: $\epsilon_{kk} \approx \Delta$.

3. The models have different definitions of plastic volume strain. In the pore collapse model, the plastic volume strain is the difference between the relative volumes of the solid particles and medium: $\epsilon_v^p = (J_s - J)/J_s$. In the analytical model, the plastic volume strain is the difference between the total and elastic volume strains: $\epsilon_v^p = \epsilon_{kk} - \epsilon_{kk}^e$.

To compare the pore collapse model in Equation C.3 with the analytical model in Equation C.1, each equation is rewritten in terms of ϵ_v^p, K, and J. The constant modulus relation from Equation C.1 becomes:

$$P = K_0(1 - J - \epsilon_v^p) \tag{C.4}$$

where the approximation $\epsilon_{kk} \approx 1 - J$ was used. The pore collapse pressure relation from Equa-

tion C.3 becomes:

$$P = K_0 \frac{1 - J - \epsilon_v^p}{(1 - \epsilon_v^p)^2} \qquad (C.5)$$

where

$$1 - \epsilon_v^p = \frac{1 - \Phi}{1 - \phi} \qquad (C.6)$$

These relations are identical when the plastic volume strain is zero, such as during the initial elastic response (see Figure C.4), but diverge as the plastic volume strain increases with increasing load.

APPENDIX D

FITTING PROCEDURE

This section describes our procedure for fitting the concrete damage model to data. We fit the isotropic damage model previously discussed in Section 2.1 to piecewise-linear representations of data provided by RDA for the Round A benchmarks. The actual data curves were not provided. RDA's representations of the data will be referred to as 'data' through-out the remainder of this section.

First we describe our fit of the model to data without including damage. Such a fit predicts elastic-perfectly plastic response for TXC tests, which is not representative of the data. Next we describe our fit of the model to data with damage included in the fit.

D.1   FIT WITHOUT DAMAGE.

We began our fitting procedure by fitting the the smooth-cap model to data without considering damage. The parameters we obtained from this fit are given in Table D.1. Note that a pressure cutoff if listed. This is because these fits were made prior to implementation of the brittle damage model. Also note that only two parameters are listed for the three invariant surface. This is because a reduced form of the Rubin three invariant model was implemented in the concrete damage model at the time this fits were made. The reduced form did not allow the shape of the failure surface in the deviatoric plane to transition with pressure. The fitting procedure without damage is standard so only a brief outline is given here, as follows:

- The initial bulk and shear moduli, K and G respectively, were provided by RDA. In general, however, they can be attained from unloading curves for from isotropic compression and uniaxial strain data at very low pressure;

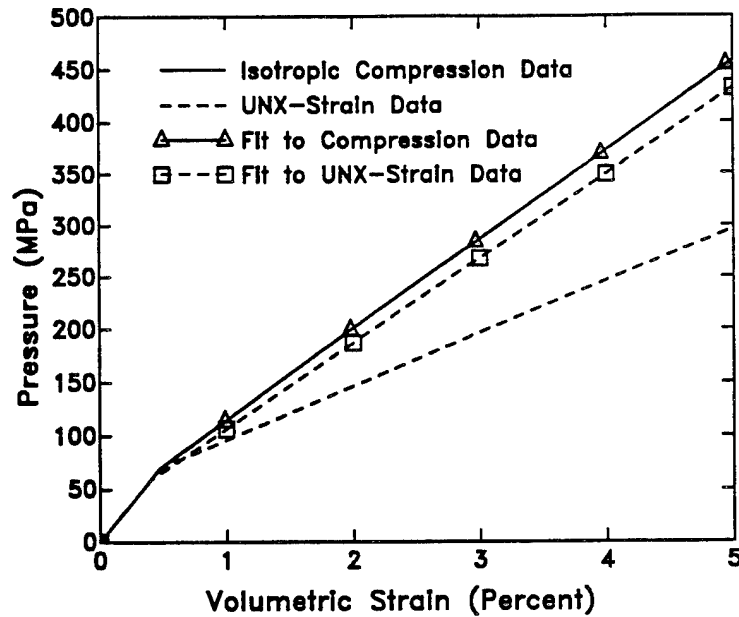- The tensile cutoff was obtained from the unconfined TXE data. This fit is given in Figure 6.7;

Figure D.2. Preliminary fits without damage to pressure-volumetric strain data.

- The four parameters of the TXC failure surface were obtained from an analytical expression provided by RDA for the peak stress difference versus pressure. This preliminary fit is given in Figure D.1a;

- The two parameters for the three-invariant model were obtained from an analytical expression for the TXE surface, and a straight-line fit between the TXE and TXC values, i.e. straight-line Mohr-Coulomb behavior in the deviatoric plane. The fit to TXE data is given in Figure D.1b;

- The three parameters of the hardening rule were obtained from the elastic bulk modulus and a bilinear pressure-volumetric strain curve obtained from hydrostatic compression data. This preliminary fit is shown in Figure D.2;

- The initial location of the cap was obtained from the isotropic compression pressure-volumetric strain curve while the cap shape function was obtained from a fit to the stress path from uniaxial strain data. This preliminary fit is given in Figure D.3.

Results of the fit without damage are compared with piecewise-linear representations of TXC test data in Figure D.4. The confining pressure is indicated next to each curve. Although we fit the peak stress fairly well, the calculated response is elastic-perfectly plastic, which is not representative of

Table D.1. Model parameters for the fit without damage.

Constitutive Model

K (MPa)	14700
G (MPa)	11025
ρ (gm/cm^3)	2.28

Failure Envelope

$$F_e(J_1) = \alpha - \gamma e^{-\beta J_1} + \theta J_1$$

α (MPa)	230
θ	0
λ (MPa)	221
β (MPa^{-1})	1.6×10^{-3}

Moveable Cap

$$F_c(J_1, \kappa) = 1 - \frac{(J_1 - L)(|J_1 - L| + J_1 - L)}{2(X - L)^2}$$

$$X(\kappa) = L + RF_e(L)$$

$$L(\kappa) = max(\kappa_0, \kappa)$$

R	1.2
X_0 (MPa)	210

Cap Hardening Rule

$$\epsilon_v^p = W\{1 - e^{-D[X-X_0] - D_2[X-X_0]^2}\}$$

W	0.12
D (MPa^{-1})	1.35×10^{-4}
D_2 (MPa^{-2})	1.00×10^{-8}

Third Invariant

$Q_1 =$TOR/TXC $Q_2 =$TXE/TXC
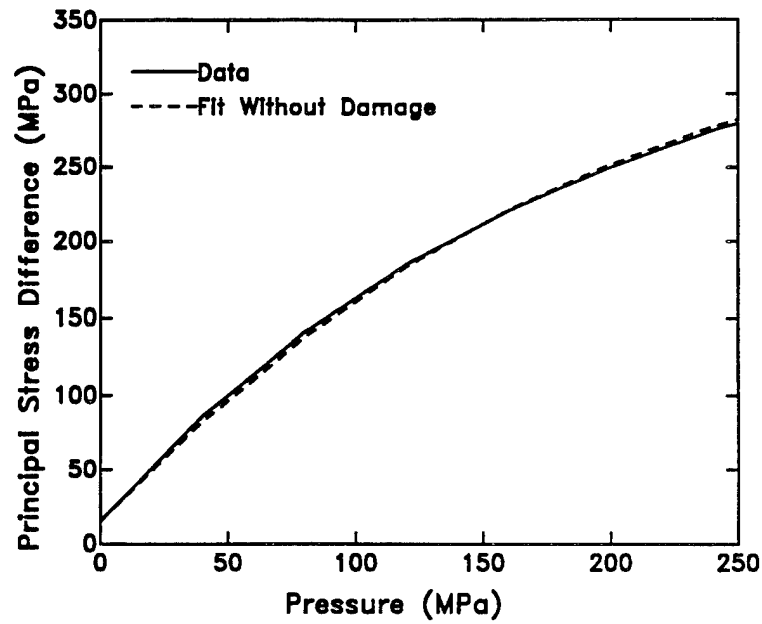
α_1	0.705
α_2	0.686

Pressure Cutoff

T (MPa)	-2.5

Damage Model

$$d = 1 - \frac{r_o(1 - A)}{\tau} - Ae^{B(r_o - \tau)}$$

r_0	1×10^5
A	0
B	0

(a) TXC data and fit.
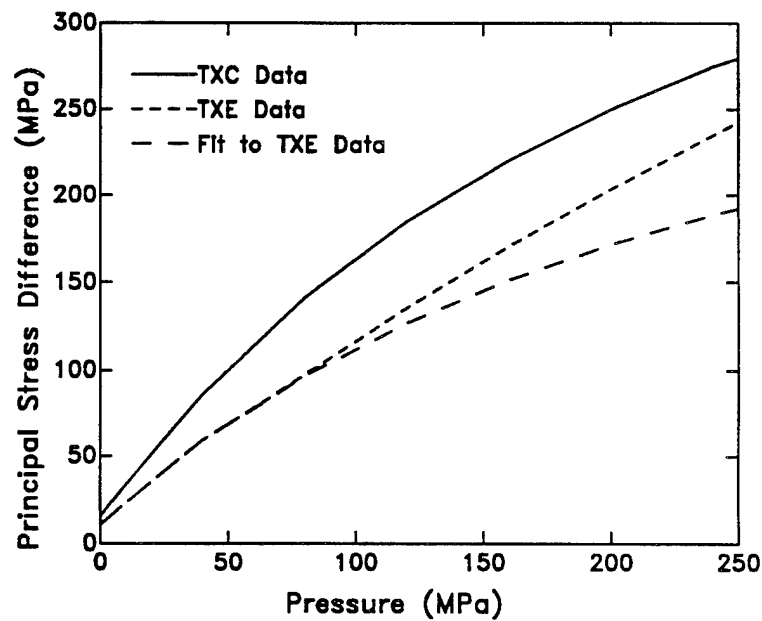
(b) TXE data and fit.

Figure D.1. Preliminary fit without damage to TXC and TXE failure surfaces.
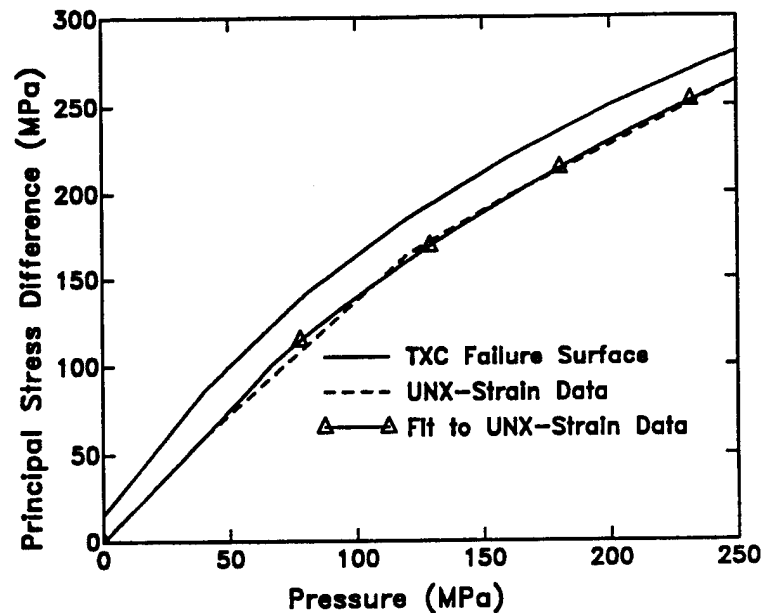
Figure D.3. Preliminary fit without damage to the stress path from uniaxial strain data.

the post-peak softening response of the lab test data. In addition, we calculate less strain hardening than measured.
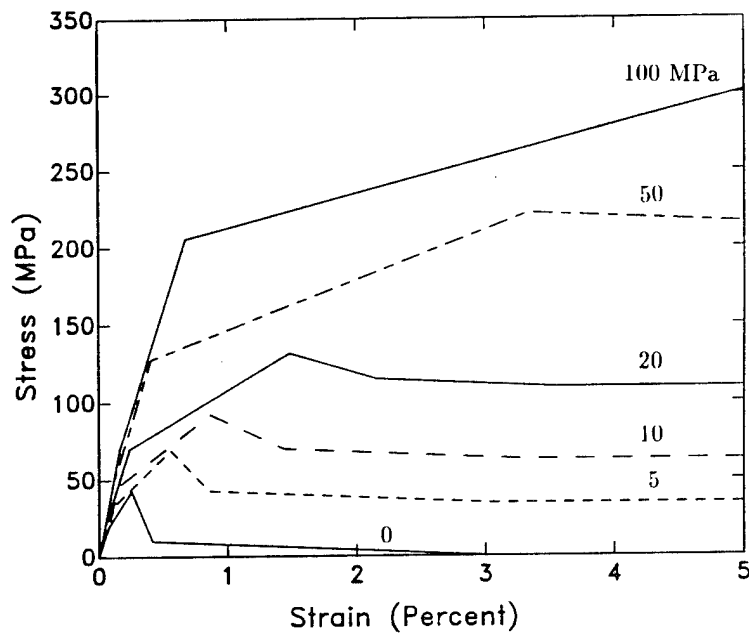
D.2 FIT WITH DAMAGE.

Our fits of the damage model to TXC data are given in Figure D.5 for confining pressure between 0 and 100 MPa. These fits should be compared with the TXC data previously given in Figure D.4b. Note that the model predicts the softening behavior of the data reasonably well, but not the hardening response.

The fit of the model, with and without damage, to the unconfined compression data is shown in Figure D.6. The ratio of the stress from the fit with damage, to the stress from the fit without damage, is the reduction factor $1 - d$. The point at which the fitted curves separate, which is at about 25 MPa in this example, depends on the value of r_o. We attempted to model a small amount of hardening in this example by selecting r_o to initiate damage prior to the peak stress. We could have selected r_o to initiate damage at the peak stress. However, damage would still have initiated prior to the peak stress in the fits with confining pressure. Thus both pre-peak hardening and
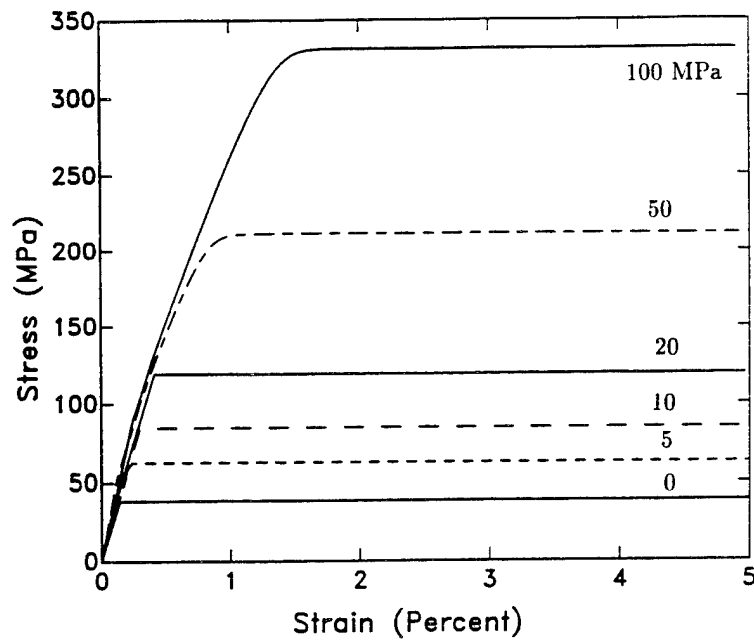
(a) Fit without damage.

(b) Data provided by RDA.

Figure D.4. Single element stress-strain curves, fit without damage to TXC data.
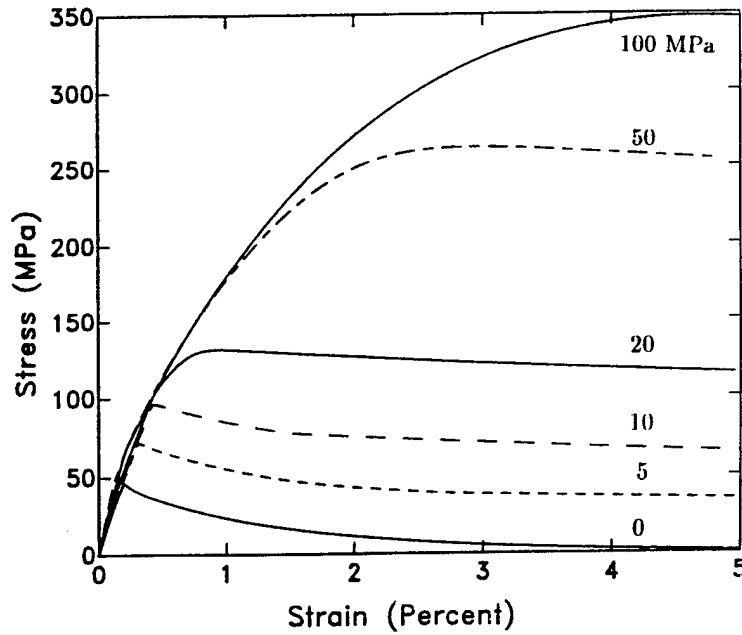
Figure D.5. Single element stress-strain curves, fit with damage to TXC data.

post-peak softening are modeled with the damage model, although the hardening response is not adequately predicted with the selected damage parameters.

The peak stress is attained by iterative adjustment of the shear failure surface location and damage model parameters. Two fits of the shear failure surface to the principal stress difference versus pressure data are given in Figure D.7. The fit labeled 'fit without damage' provides the peak stress of the elastic-perfectly plastic curves previously given in Figure D.4. The fit labeled 'fit with damage' provides the peak stresses calculated with and without damage and previously shown in Figure D.6. Note that we adjusted the shear failure surface upward to include damage in the model. Otherwise, the peak stresses attained from our fit with damage would be less than the desired values. Our adjusted parameters for the fit with damage are given in Table D.2. It is evident from our fitting procedure that the peak stress of our damage model depends on damage accumulation as well as plasticity.

The value of the damage parameter d depends on the elastic strain energy term, τ. Equivalent strain histories are shown in Figure D.8 and demonstrate that the equivalent strain in unconfined compression is four times larger than that for a 50 MPa confining pressure. The equivalent strain decreases with confinement in TXC calculations, apparently due to less lateral expansion with higher confinement, so the damage accumulation also decreases with confinement. This is why less softening
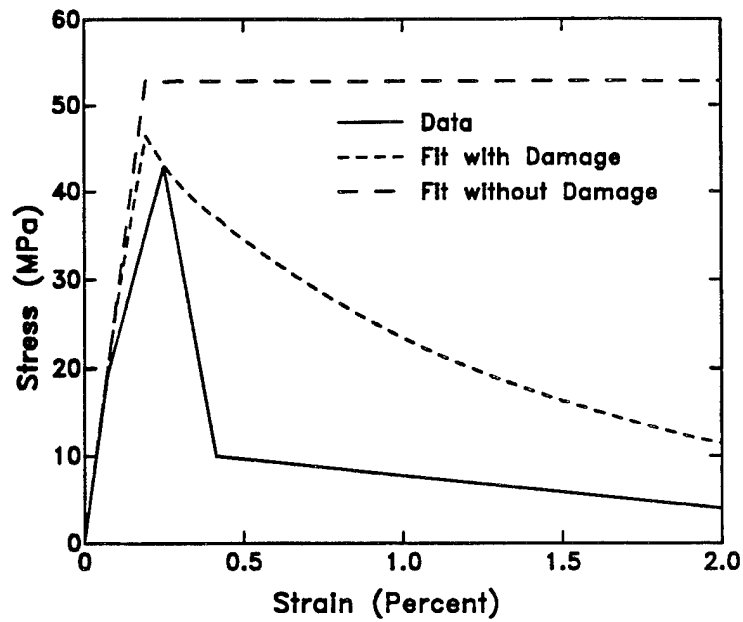
Figure D.6. Fits with and without damage, to unconfined compression data.
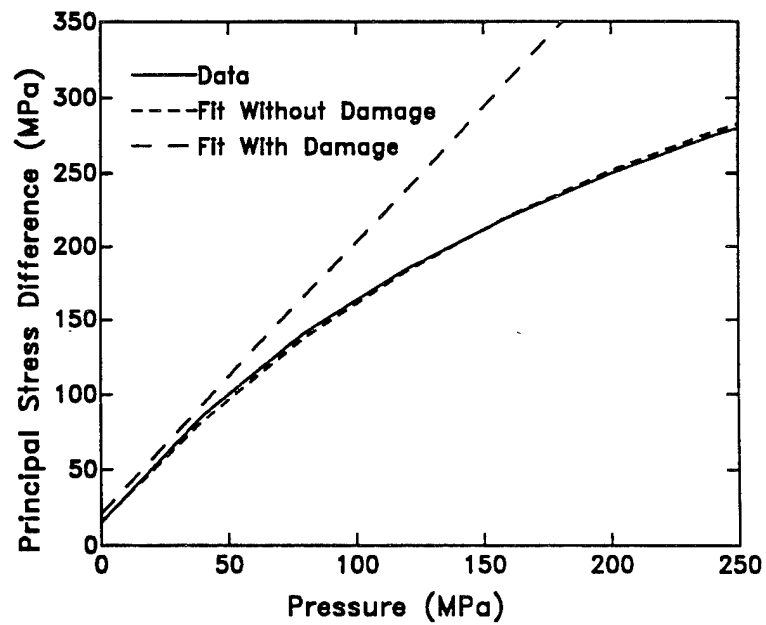

Figure D.7. Adjustment of the shear failure surface fit to account for pre-peak damage.

Table D.2. Model parameters for the fit with damage.

Constitutive Model

K (MPa)	14700
G (MPa)	11025
ρ (gm/cm^3)	2.28

Failure Envelope

$$F_e(J_1) = \alpha - \gamma e^{-\beta J_1} + \theta J_1$$

α (MPa)	12
θ	0.35
λ (MPa)	0
β (MPa^{-1})	0

Moveable Cap

$$F_c(J_1, \kappa) = 1 - \frac{(J_1 - L)(|J_1 - L| + J_1 - L)}{2(X - L)^2}$$

$$X(\kappa) = L + RF_e(L)$$

$$L(\kappa) = max(\kappa_0, \kappa)$$

R	1.2
X_0 (MPa)	210

Cap Hardening Rule

$$\epsilon_v^p = W\{1 - e^{-D[X-X_0]-D_2[X-X_0]^2}\}$$

W	0.12
D (MPa^{-1})	1.35×10^{-4}
D_2 (MPa^{-2})	1.00×10^{-8}

Third Invariant

$Q_1 =$ TOR/TXC $Q_2 =$ TXE/TXC

α_1	0.705
α_2	0.686

Pressure Cutoff

T (MPa)	-2.5

Damage Model

$$d = 1 - \frac{r_o(1 - A)}{\tau} - Ae^{B(r_o - \tau)}$$

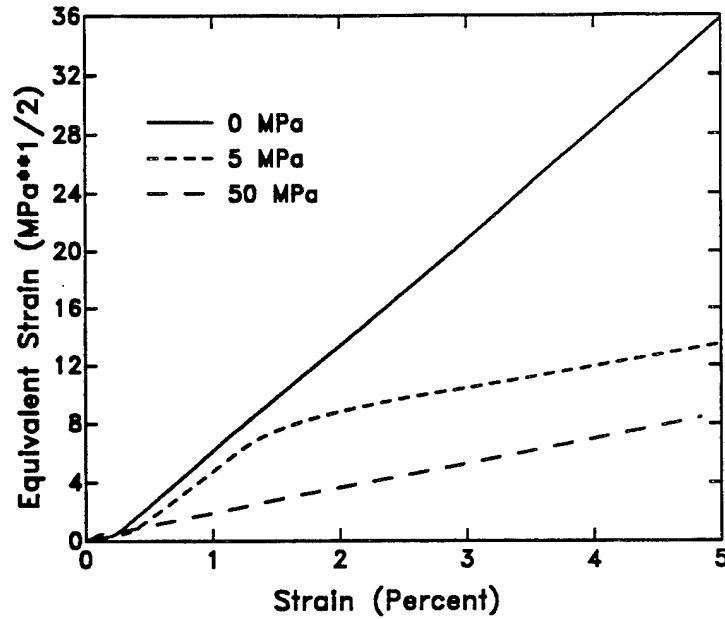| r_0	0.15
A	0.8
B	0.1

Figure D.8. Variation of equivalent strain energy with confining pressure.

is observed in the TXC stress-strain curves as the confinement level increases.

Two fits of the damage model to the unconfined compression data are shown in Figure D.9. The parameter A was selected to fit the peak stress and the parameter B provides the steepness of the softening response. We selected r_o to initiate damage just prior to the peak stress. This figure demonstrates how the softening response is affected by the parameter B, holding A and r_o constant.

As previously mentioned, we first fit our model to the data without including damage, i.e. an elastic-perfectly plastic fit to TXC stress-strain curves. Then we included damage in the fit by iteratively adjusting the damage parameters and shear failure surface location to account for pre-peak plasticity and damage accumulation. However, no iterative adjustments were made to other aspects of the fit, such as the hardening rule or cap shape function. This is because we wanted perform the Group 2 lab test simulations first, to assess our selection of the damage model parameters. The effect of damage on our original fits is discussed in the following paragraphs.

Our fit of the model, including damage, to isotropic compression and uniaxial strain data is shown in Figures D.10 and D.11. The pressure-volumetric strain curves calculated with damage lie below
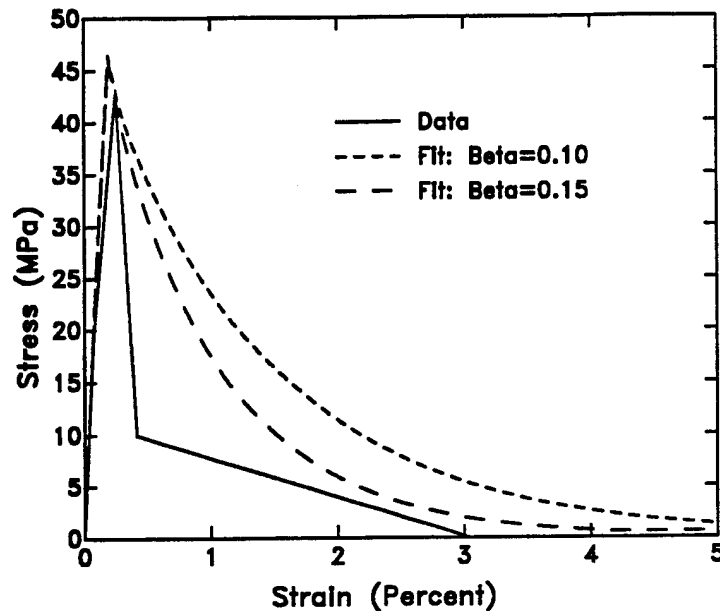
Figure D.9. Two example fits with damage to unconfined compression data.

those of the measured data, whereas the stress path with damage lies above the measured data. A better fit to the data could be obtained by iteratively adjusting the hardening rule, cap shape, and damage model parameters. Of course, any adjustment to these parameters would also affect our fit to the TXC stress-strain data previously shown in Figure D.5. Thus an analyst must iterate among numerous parameters to obtain a good fit of the smooth-cap model with damage to data. One recommendation is development of an automated optimization fitting procedure, such as a least-squares procedure.

One final point to note is that our model predicts plastic volume expansion, or dilation, which is commonly observed in concrete test specimens. Figure D.12 demonstrates that substantial volume expansion is predicted at low confining pressures. The volumetric strain in this figure is negative in expansion and positive in compression. Slight volume expansion occurs at 10 MPa, but not at higher confining pressures. The volume expands due to large lateral tensile strains (plastic flow) in the TXC calculations. Measured post-peak volume strains are not available for comparison with the calculations because they were not provided by RDA due to unreliable strain gage measurements.
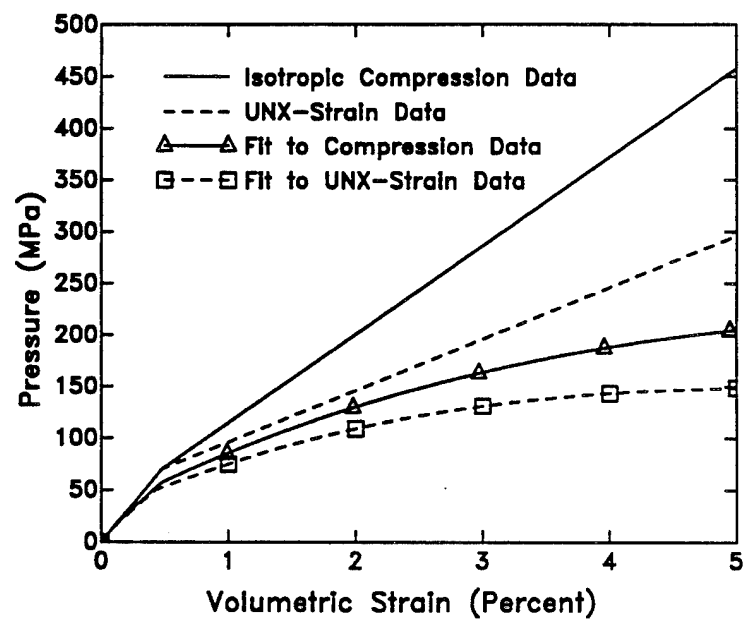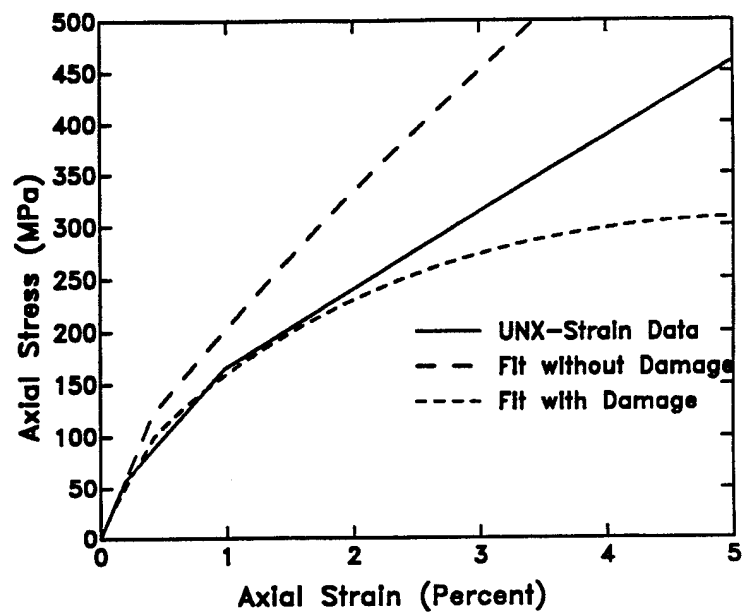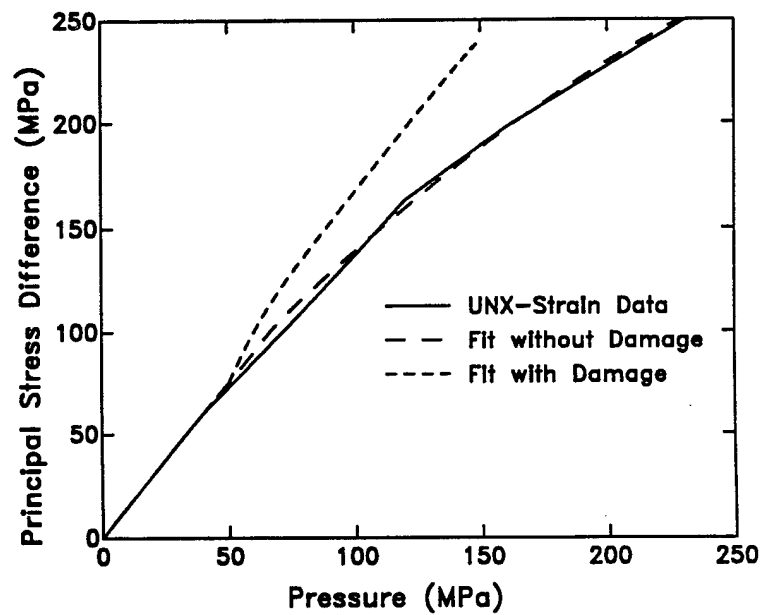
Figure D.10. Fits of the model, with damage, to pressure-volumetric strain data.

(a) Axial stress-strain response.

(b) Stress path.

Figure D.11. Fits of the model, with and without damage, to uniaxial strain data.
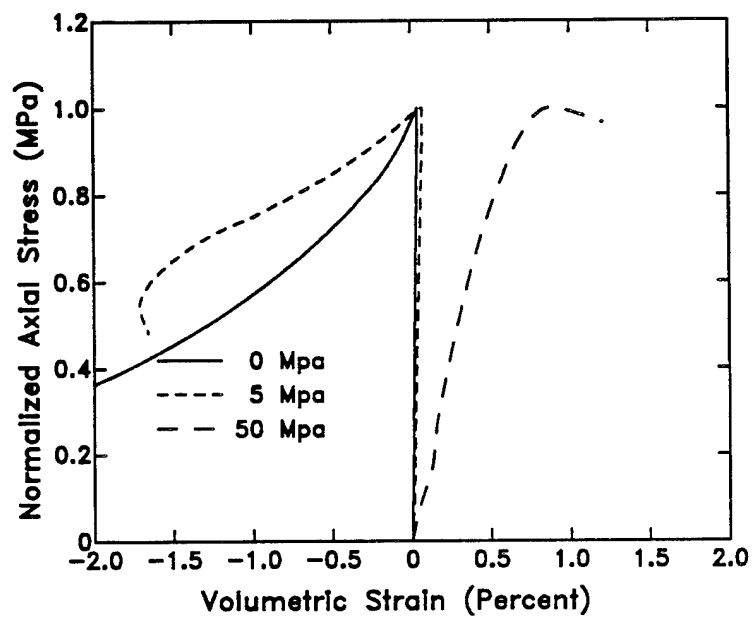
Figure D.12. Predicted volume expansion under TXC loading.

DISTRIBUTION LIST

DNA-TR-94-190

DEPARTMENT OF DEFENSE

DEFENSE INTELLIGENCE AGENCY
    ATTN: DIW-4
    ATTN: PAX-5B G WEBER

DEFENSE NUCLEAR AGENCY
    ATTN: SPSD
    ATTN: SPWE LTC JIM HODGE
2 CY ATTN: SSTL
    ATTN: TASS DR C GALLOWAY
    ATTN: TDTR

DEFENSE TECHNICAL INFORMATION CENTER
2 CY ATTN: DTIC/OCP

FIELD COMMAND DEFENSE NUCLEAR AGENCY
    ATTN: FCTO
    ATTN: FCTT DR BALADI

JOINT STAFF/J-8
    ATTN: J8 WAR FIGHTING DIV

DEPARTMENT OF THE ARMY

ARMY RESEARCH LABORATORIES
    ATTN: AMSRL-SL-CE

DEP CH OF STAFF FOR OPS & PLANS
    ATTN: DAMO-NCZ

U S ARMY ATMOSPHERIC SCIENCES LAB
    ATTN: SLCAS-AR-M R SUTHERLAND

U S ARMY ENGR WATERWAYS EXPER STATION
    ATTN: C WELCH CEWES-SD-R
    ATTN: CEWES-SS-R DR BALSARA
    ATTN: D RICKMAN CEWES-SE-R
    ATTN: E JACKSON CEWES-SD-R
    ATTN: F DALLRIVA CEWES-SS-R

U S ARMY NUCLEAR & CHEMICAL AGENCY
    ATTN: MONA-NU DR D BASH

U S ARMY RESEARCH LAB
    ATTN: AMSRL-WT-TA G BULMASH
    ATTN: SLCBR-SS-T

DEPARTMENT OF THE NAVY

NAVAL RESEARCH LABORATORY
    ATTN: CODE 5227 RESEARCH REPORT

NAVAL SURFACE WARFARE CENTER
    ATTN: CODE K42 L VALGE

NAWCWPNSDIV DETACHMENT
    ATTN: CLASSIFIED LIBRARY

OFFICE OF CHIEF NAVAL OPERATIONS
    ATTN: NUC AFFAIRS & INT'L NEGOT BR

DEPARTMENT OF THE AIR FORCE

AIR UNIVERSITY LIBRARY
    ATTN: AUL-LSE

HQ USAF/XOFS
    ATTN: XOFN

PHILLIPS LABORATORY
    ATTN: PL/WS MR SHARP

USAF SPACE COMMAND
    ATTN: LT COL CROSS

DEPARTMENT OF ENERGY

LAWRENCE LIVERMORE NATIONAL LAB
    ATTN: PAUL GUDIKSEN
    ATTN: R PERRETT

LOS ALAMOS NATIONAL LABORATORY
    ATTN: A S MASON
    ATTN: J NORMAN
    ATTN: R W WHITAKER
    ATTN: B SHAFER

OTHER GOVERNMENT

CENTRAL INTELLIGENCE AGENCY
    ATTN: OSWR/NED 5S09 NHB
    ATTN: OSWR S WALLENHORST

DEPARTMENT OF DEFENSE CONTRACTORS

AEROSPACE CORP
    ATTN: P RAUSCH

APTEK, INC
2 CY ATTN: B B LEWIS
    ATTN: T MEAGHER
2 CY ATTN: Y D MURRAY

BOEING TECHNICAL & MANAGEMENT SVCS, INC
    ATTN: D ECKBLAD

CALSPAN CORP
    ATTN: M DUNN
    ATTN: M HOLDEN

CARPENTER RESEARCH CORP
    ATTN: H J CARPENTER

GENERAL ATOMICS, INC
    ATTN: CHARLES CHARMAN

GENERAL RESEARCH CORP
    ATTN: W ADLER

H & H CONSULTANTS, INC
    ATTN: W HALL

HORIZONS TECHNOLOGY, INC
    ATTN: B KREISS
    ATTN: B LEE

INSTITUTE FOR DEFENSE ANALYSES
    ATTN: CLASSIFIED LIBRARY
    ATTN: E BAUER

JAYCOR
    ATTN: CYRUS P KNOWLES

KAMAN SCIENCES CORP
    ATTN: T STAGLIANO

KAMAN SCIENCES CORP
    ATTN: VERNON SMITH

KAMAN SCIENCES CORP
    ATTN: D MOFFETT
    ATTN: DASIAC

KAMAN SCIENCES CORPORATION
    ATTN: DASIAC

LACHEL AND ASSOCIATES, INC
    ATTN: J BECK

LOGICON R & D ASSOCIATES
    ATTN: DON SIMONS
    ATTN: LIBRARY

LOGICON R & D ASSOCIATES
    ATTN: G GANONG

LOGICON R & D ASSOCIATES
    ATTN: E HUMPHRIES
    ATTN: J WEBSTER
    ATTN: T MAZOLLA

MAXWELL LABORATORIES INC
    ATTN: S HIKIDA

SCIENCE APPLICATIONS INTL CORP
    ATTN: J STODDARD

SCIENCE APPLICATIONS INTL CORP
    ATTN: D BACON
    ATTN: J COCKAYNE
    ATTN: P VERSTEEGEN
    ATTN: W LAYSON

SCIENCE APPLICATIONS INTL CORP
    ATTN: J MANSHIP

SOUTHERN RESEARCH INSTITUTE
    ATTN: C PEARS

SRI INTERNATIONAL
    ATTN: J GRAN
    ATTN: M SANAI

TECH REPS, INC
    ATTN: F MCMULLAN

TITAN CORPORATION (THE)
    ATTN: M ITO

TOYON RESEARCH CORP
    ATTN: J CUNNINGHAM

TRW S.I.G.
    ATTN: NORMAN LIPNER

WEIDLINGER ASSOC, INC
    ATTN: DARREN TENNANT
    ATTN: H LEVINE

WEIDLINGER ASSOCIATES, INC
    ATTN: M BARON